Empirical Analysis of Pneumatic Tire Friction on Ice

Troy Nigel Holley

Thesis submitted to the Faculty of

the Virginia Polytechnic Institute and State University

in partial fulfillment of the requirements for the degree of

Master of Science

in

Mechanical Engineering

Corina Sandu

Mehdi Ahmadian

Saied Taheri

September 14, 2010

Blacksburg, VA

Keywords: Friction, Ice, Terramechanics, Tires

Empirical Analysis of Pneumatic Tire Friction on Ice

Troy Nigel Holley

Abstract

Pneumatic tire friction on ice is an under-researched area of tire mechanics. This study covers the design and analysis of a series of pneumatic tire tests on a flat-level ice road surface. The terramechanics rig of the Advanced Vehicle Dynamics Lab (AVDL) is a single-wheel test rig that allows for the experimental analysis of the forces and moments on a tire, providing directly the data for the drawbar pull of said tire, thus supporting the calculation of friction based on this data. This indoor testing apparatus allows for some degree of replication by helping to maintain test conditions and by imposing a desired tire slip; the normal load, camber angle, toe angle, and other testing configurations can also be pre-set, as required. Methods of and issues related to controlling the production of ice and maintaining the conditions of numerous factors for each trial run were also documented.

The AVDL terramechanics rig allowed for the collection of data from tests that varied the tire tread, tire inflation pressure, normal load on the wheel, and the slip ratio of the moving tire. This empirical data was then analyzed through the statistical analysis program JMP 8 in order to determine which factors (or combination of factors) significantly influence pneumatic tire friction on ice. The analysis verified that the slip ratio had a significant effect on the observed coefficient of friction, which decreased as the slip ratio increased. The combinations of the slip ratio and inflation pressure and the slip ratio and tire setup also had a significant effect on the observed coefficient of friction. The tests appear to have validated the theory that the drawbar pull and the traction was higher for the tire with tread.

Acknowledgements

I'd like to thank several people that helped me over the course of this research and in completing my degree: Dr. Sandu for the chance to work at CVeSS and for the incredible opportunity to obtain a Master's Degree in Mechanical Engineering from Virginia Tech. Adam Woodward for his work on obtaining the enclosure and alleviating the friction problems plaguing the rig, along with Colin, Heather, and Vivake from NASA. Ben Taylor for his continued support with the Terramechanics Rig and the software and responding to minor questions I had. Michael Craft for his help on modifying the crossbar and moving around literally tons of equipment and sand and assisting with some of the cleanup. Clemente Negode for his steel angle idea for the camber. Thanks to my good friend [and future doctor] Ozma for giving me moral support over the summer. Special thanks to the National Science Foundation for their support through the NSF Grant Opportunities for Academic Liaison with Industry (GOALI) grant and the Graduate School Recruiting Office for their support through the Powell Fellowship. And of course thanks, Ma, for constant checking to see how I was doing and making sure I was alright…

Table of Contents

List of Figures

List of Tables

1 Introduction

1.1 Motivation of the Study

Tires are key components of a vehicle, with a huge impact on the vehicle dynamics. In order to control a vehicle on an ice surface it is necessary for a driver to have proper training and/or experience to understand how to keep the vehicle stable on such a low-friction surface, and how to properly utilize the equipment on said vehicle. One of the most important elements, if not the most important one, is the pneumatic tire. The tire has to have consistent and predictable responses to driver input and has to allow the vehicle to steer and accelerate or decelerate as necessary in icy conditions. The friction between a tire and ice is critical in the overall traction of the vehicle on an icy surface. Since safety and stability are directly derived from the tire and road interface, a tire with consistent and reliable characteristics is crucial to assisting the driver.

This interaction between tires and ice is a complex phenomenon on which this research seeks to gain insight. There are numerous factors that affect the coefficient of friction between a tire and ice surface. The experiments carried out in this paper included the tire tread, the normal load, the tire inflation pressure, and the slip ratio. These and other factors have been tested on full-sized vehicles but keeping variables consistent is a challenge for these tests as they are mainly performed outdoors. In order to keep these factors consistent, the indoor Terramechanics Rig located in the Advanced Vehicle Dynamics Lab (AVDL) was utilized.

1.2 Research Objective

The main objective of this study is to understand the impact of different vehicle and tire parameters on the tractive capacity of pneumatic tires. Moreover, we aimed at extracting the coefficient of friction from the experimental data collected on the Terramechanics Rig as a function of tire slip. To achieve these goals, the following tasks had to be performed: a) Ensure repeatability and consistency of experiments in the Terramechanics Rig. b) Select the main parameters to be investigated and perform a complete design of an experiment for the Terramechanics Rig where these parameters will be varied. c) Conduct the experiments and collect all the data. d) Analyze and interpret the data collected.

1.3 Research Approach

Tire friction on ice is not a well-documented area of pneumatic tire research. To find previous studies concerning wheeled vehicles operating in icy conditions required the use of numerous different sources for information, not limited to, but including Engineering Village, SAE, Virginia Tech's library, Interlibrary Loan (ILL), internet search engines, and so on. Engineering Village was one of the most useful references as it linked to numerous journal articles—many of which had to be requested through the Virginia Tech's ILL system.

The use of a Terramechanics Rig in the analysis of tire friction on ice is a novel idea that has not been attempted in previous studies. Some of the past studies extracted the information needed from small-scale experiments and full-size vehicle tests. Most of the small scale tests did not use actual tires. A few tests simply used a rubber block, while one test used an actual piece of tire tread. One study did however have a turntable apparatus that appeared to use a full-size tire. The larger scale tests were usually conducted using full-size trailers or actual instrumented

vehicles. Some of these tests were completed only a few years ago but much of the research papers conducted tests 10 to 20 years ago.

1.4 Thesis Outline

This thesis is divided into several sections in order to elaborate on the research and experiments conducted. Chapter two is the review of literature and covers previous tests that are similar to this study. There is an analysis of their procedures and an overview of the data they collected, including models that are relevant to this study. Chapter three covers the background of pneumatic tires. This goes into the various pieces that make up the structure of a pneumatic tire and how this affects the friction observed from the tire.

Chapter four describes some of the characteristics of tires being used on an ice surface. Chapter five gives an overview of what parameters will be relevant in order to compare the data gathered from the Terramechanics Rig to previous studies. Chapter six details the various pieces of equipment that have been used to collect and analyze data in this study. Chapter seven describes the creation of the test surface. Chapter eight describes the design of experiment and the software used to create the design. Chapter nine gives an overview of the data collected and an interpretation of the results. Chapter ten concludes the study.

2 Review of Literature

In order to gain some insight into how tests of tire friction on ice might be conducted at the scale of the Terramechanics Rig in the Advance Vehicle Dynamics Lab (AVDL), smaller scale tests and smaller-scale testing apparatus had to be reviewed. This would provide some background on how to structure the tests and maintain test conditions. The data collected from the tests conducted on the Terramechanics Rig would ideally be compared to published data from past studies, including full-scale tests, rubber friction on ice tests, and any other relevant test data. Previous models were also analyzed to see if the Terramechanics Rig could provide input data for them and also for benchmarking purposes.

The first section of this literature review covers previous testing methods and their usefulness in the current study. The second portion goes over some of the previous ice friction data and its relevance to this study. The third portion covers relevant models that can be used for comparison to data collected in this study and as a starting point for creating new tire-friction-on-ice models.

2.1 Review of Literature: Test Methodology

In A New Method for Determining Tire Traction on Ice [1], the researchers had a tire rig and a rotating tray that could hold snow or ice. They did not explain what kind of tire hub or motor they utilized, but gave the parameters they would use to create their friction data. They only mentioned that the tray allowed them to test for the coefficient of friction at various slip angles. They attempted to keep the test conditions identical, but ended up with two different temperatures, -5.0°C and -4.8°C, which had similar lateral coefficients of friction up until 3 degrees of slip angle, and deviated with a coefficient of friction of 0.004 at the max slip angle

tested of 10 degrees of slip [2]. The ice was created in a circular turntable, or rotating tray, as seen in Figure 2-1.

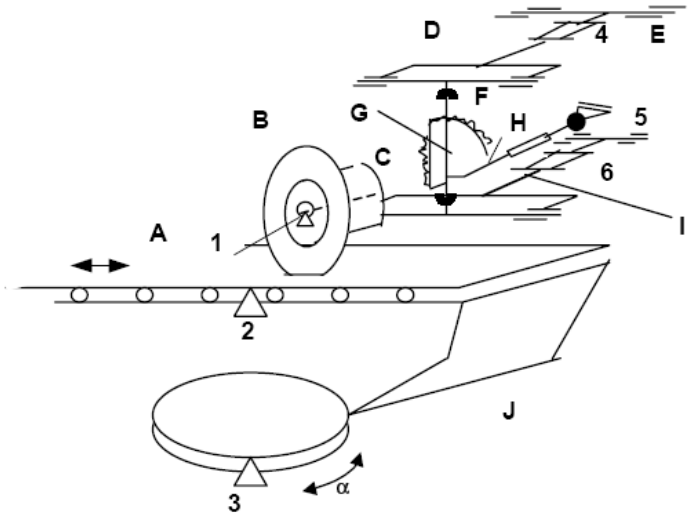

Fig. 2 The schematic diagram of the tire tester

A-platform; B-tire; C-special hub; D-upper guide arm; E-base; F-sector body; G-vertical shaft; H-horizontal pulled bar; I-lower guide arm; J-turntable; 1,3-angle measuring sensor; 2-travel sensor; 4,6-force measuring ring; 5-force measuring bar

Figure 2-1. The tire testing device utilized by the authors of [3]. Turntable not drawn to scale.

To eliminate bubbles they suggested using a reduced rate of ice growth, giving an example of 3 millimeters per hour. The exact rate they utilized was not specified. To finish off the ice surface, they used a blade made of Perspex, commonly known as acrylic or Plexiglas. This smoothed the top of the surface and left behind some ice fragments that were then wiped away with a "clear absorbent cotton cloth" [sic] (assumedly a clean cotton cloth). To lower the heat transfer between the ice and the surroundings, the test trough had two air channels (one on each side) that blew cool air over the surface [3].

After each test, the blade process was repeated to ensure identical test conditions. This was followed by cleaning off the surface again. The previous test or another past test would be repeated on a portion of the new surface to determine if the ice was indeed similar. The researchers did not specify how many tests they completed, as they did not utilize any test data from their machine, instead using numbers from previous studies. Their tests over adjacent days showed that their methodology could ensure good repeatability and illustrated the advantage of an indoor test [3].

In the Study of the Test Method to Determine Rubber-Icy Road Friction, the authors used a reciprocating tray of ice that moved against two pieces of tire tread seen in **Figure 2-2** This apparatus allowed them to carry out tests at varying vertical pressure, slip velocity, and temperature (to get information at high and low "sliding speed regions") [4].

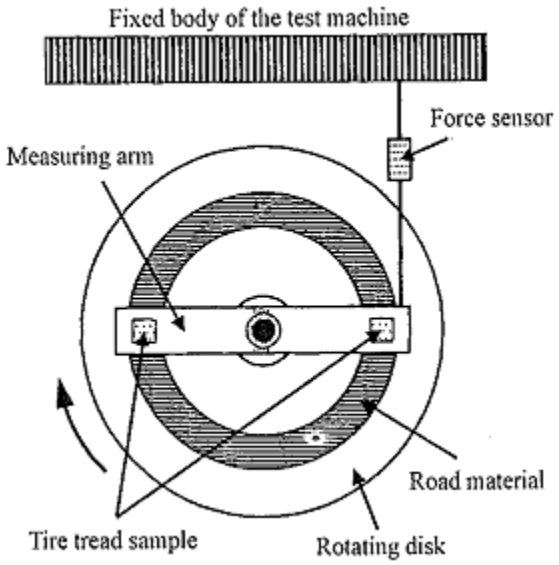

Figure 2-2. Diagram of the test machine used in the study which utilizes two samples of tire tread instead of a full tire [4]. The diagram also shows how the force is measured through the use of a force sensor attached to the tread sample.

Through their observations, the authors noted that the rubber compound used in tires did not obey Coulomb's law. They concluded that a tire's mechanical performance was closely related to its friction characteristics. Their data showed that temperatures lower than the freezing point of water produced higher coefficients of friction independent of vertical load. Also, at temperatures lower than freezing, lower vertical loads increase the coefficient of friction as evident in Figure 2-3.

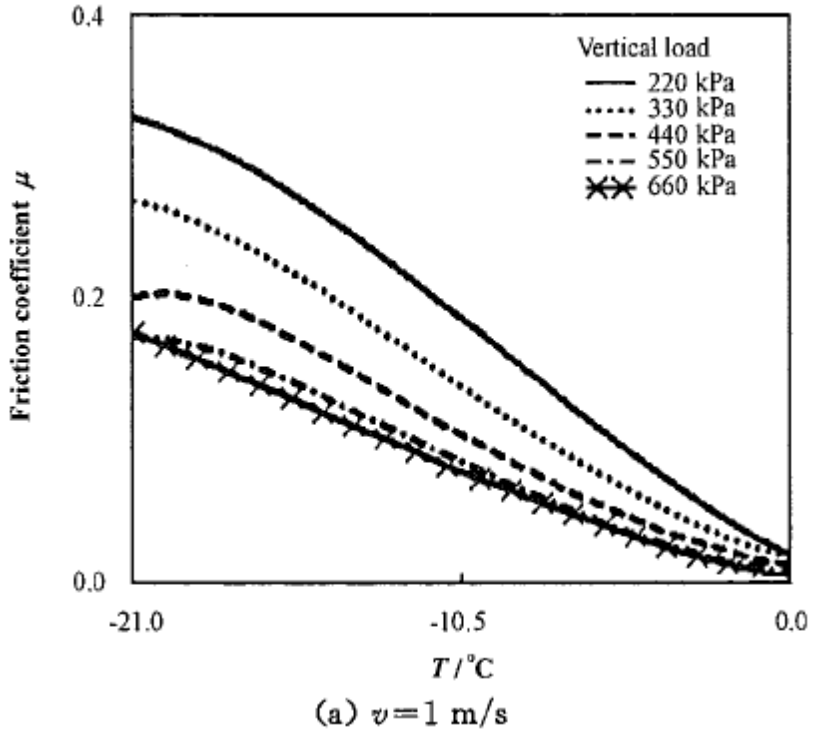

Figure 2-3. Comparison of the coefficient of friction versus the ice temperature [4].

The authors of Three Approaches to Winter Traction Testing Using Instrumented Vehicles compared three test vehicles that had three different methods of testing the coefficient of friction for winter surfaces. These three vehicles were the CRREL instrumented vehicle, the Uniroyal-Goodrich (U-G) traction tester and the SAAB Friction tester which was used for a

different purpose. The CRREL vehicle (CIV) was designed for vehicle mobility research. The Uniroyal-Goodrich tester was developed for commercial tire testing. The SAAB friction tester was developed for airport runway safety. Each vehicle had its own set of procedures and data analysis [5].

Going over previous methods for testing the traction on different surfaces, the researchers noted that before the 1970's the most common traction test was a drawbar pull test. This test utilized a load cell attached to the rear of the vehicle to measure the "amount of pull" the instrumented vehicle could produce. Conversely, these more recent test setups allow the traction to be measured at each individual wheel and to be controlled by a computer, for more accuracy and quicker results [5].

The authors of [4] compared the three test vehicles in order to establish a basis for future studies. They observed an average traction coefficient of 0.03 on smooth ice compared to an average of 0.72 on an asphalt runway. The U-G tester and the CIV reported similar results in all of the tests while the SAAB vehicle had different values since it was tuned specifically to airport runways. From the data they collected, the researchers observed a maximum coefficient of friction of ice around 0.2 and a an average coefficient of ice around 0.15. They also noted that the SAE conservatively reports the friction values that correspond to untrained drivers operating their cars at high slip (values) on icy roads [5].

The Cold Regions Research and Engineering Laboratory (CRREL) conducted experiments to determine the coefficient of friction of ice versus various materials. They utilized a temperature control room that measured 3 meters by 5 meters (9.84 feet by 16.4 feet). In this

environment they literally dragged ice samples of varying sizes against samples on a testing table using plywood boxes as sample holders, as seen in Figure 2-4.

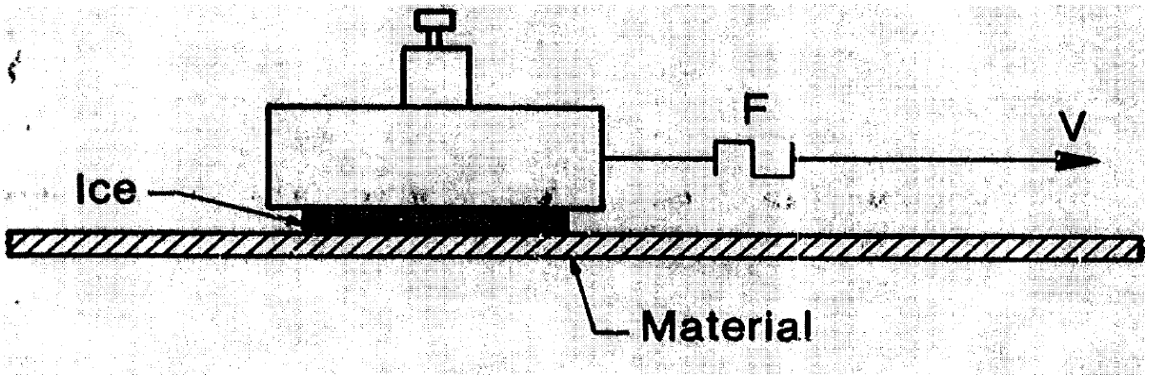

Figure 2-4. First test setup with ice being dragged across the stationary material on a table [6].

The tables measured 0.6 meters by 3 meters (1.96 feet by 9.84 feet). Starting and stopping the dragging process meant that they only had 2 meters of testing length. For a second set of tests, they reversed this setup using a large test basin for ice that measured "34.4 by 9 m [sic] (113 feet by 29.5 feet), as seen in **Figure 2-5**. This merely doubled their original testing length to 4 meters. In comparison the Terramechanics Rig is 25 feet long by 6 feet, with approximately half of this area available for testing [6].

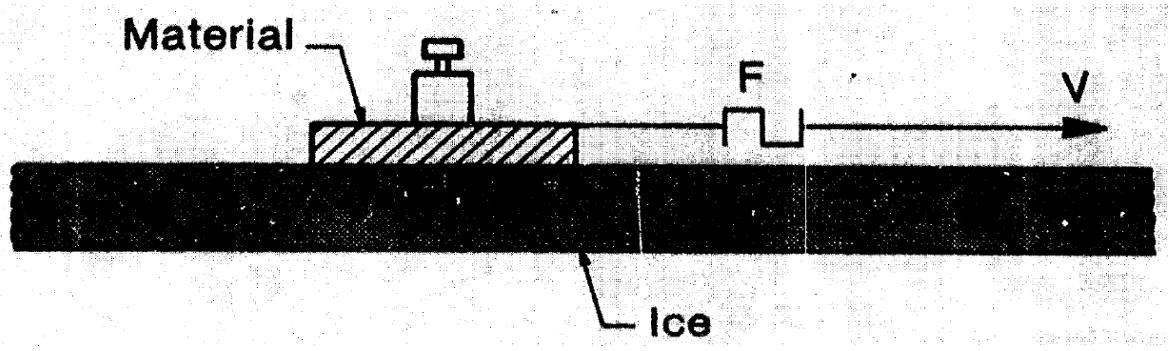

Figure 2-5. The opposite configuration with stationary ice and sample materials [6].

The device used to drag the items was a custom towing apparatus created from a Bodine variable speed motor, shown in Figure 2-6. The motor was stepped down by a ratio of 20:1 so that the maximum speed of the motor was 86 rpm. This was mated to a 7 cm diameter pulley, or a circumference of 22 cm. This means that the maximum speed the device could pull materials at was around 31.5 cm/s using a calculation of (22 cm divided by 1.4333 revolutions per second) [6]. This value is well within the range of the rig, as it has a maximum translational speed around 78 cm/s.

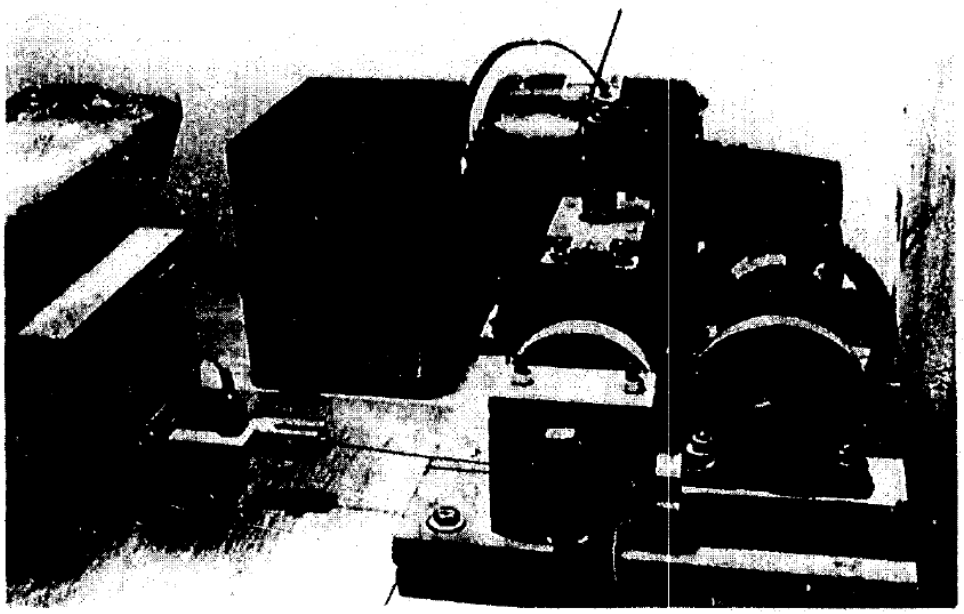

Figure 2-6. Towing apparatus used in CRREL tests [6].

The researchers noted that as the normal load increased between the ice and the materials they tested, the coefficient of friction would decrease. The roughness also affected the coefficient of friction of ice versus any material. Polishing their metal samples had the effect of greatly reducing the coefficients of friction versus ice [6]. Similarly to polished metal, it can be

observed that after several vehicles have run over a section of ice or even snow, that the ice becomes smoother as the result of melting.

2.2 Combined Testing Parameters

From these previous tests, a basic guideline begins to form. Essentially, any indoor tests done on ice should be consistent with the following:

1) Tests use a quarter-car or single wheel rig for convenience and repeatability
2) Tests are run indoors in a controlled environment
3) The type, hardness, and orientation of the ice (top or bottom orientation) is maintained in its creation
4) The ice is created at a very slow rate of growth to form a clear surface without air bubbles
5) The ice is smooth, level, and uniform
6) The tire surface is clean and as smooth as possible (ignoring the tread itself)
7) Temperature of the finished ice surface stays constant
8) The air temperature stays as constant as possible
9) The temperature of the tire, surface, and bulk of ice is the same, or as close as possible
10) Repeated tests are done on re-surfaced ice that has relaxed or a new portion of the same surface as the previous test
11) Normal load and inflation pressure remain constant during each trial

2.3 Review of Literature: Data From Previous Tire on Ice Tests

The researchers of the Study of the Test Method to Determine Rubber-Icy Road Friction collected data from their reciprocating ice tray at various temperatures, vertical loads, and speeds

[4]. The refrigeration system used in the current experiment allows for the control of the temperature of the ice. For the purposes of the experiment, the data obtained can be directly compared to the coefficient of friction observed at -3 °C (26.6 °F) seen in Figure 2-7. Using a rough estimate of a 26 cm wide and 18 cm long tire contact patch—the length based on the ratio of the width to the length seen in [7] results in 468 cm^2 (72.5 sq in) contact patch area. The higher testing range would be around 8825 N (1984 lbf) resulting in a vertical load of 18.9 N/cm^2 or 189 kPa.

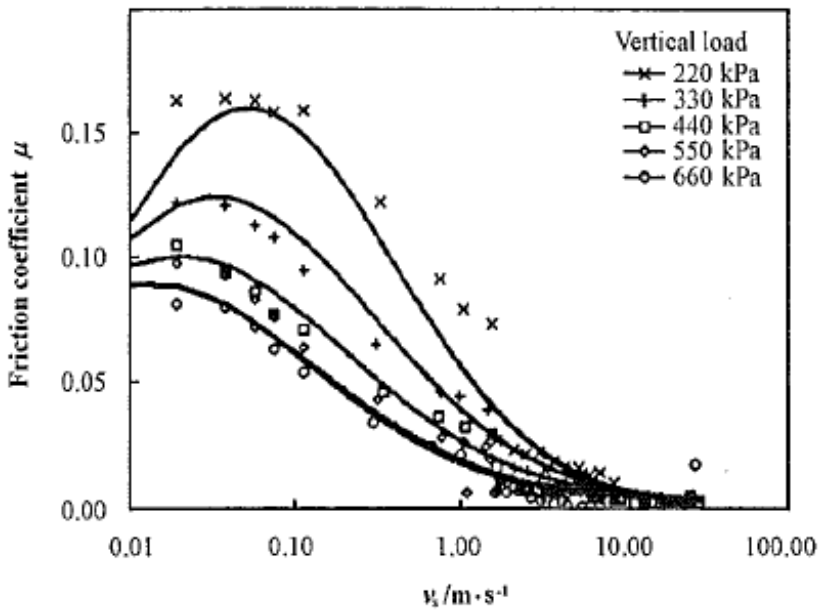

Figure 2-7. Comparison of the coefficient of friction versus varying vertical load in kPa (1 kPa = 0.1 N/cm^2) at a temperature of -3 °C (26.6 °F) [4].

In A New Method for Determining Tire Traction on Ice the authors had data from Tire Force Generation on Ice that looked at the change in the coefficient of friction as the sliding speed, or the speed of the tires minus the speed of the axle (vehicle speed). The test data from

this paper showed that the coefficient of friction steadily decreased with increasing sliding speed, v_s, seen in Figure 2-8 [1].

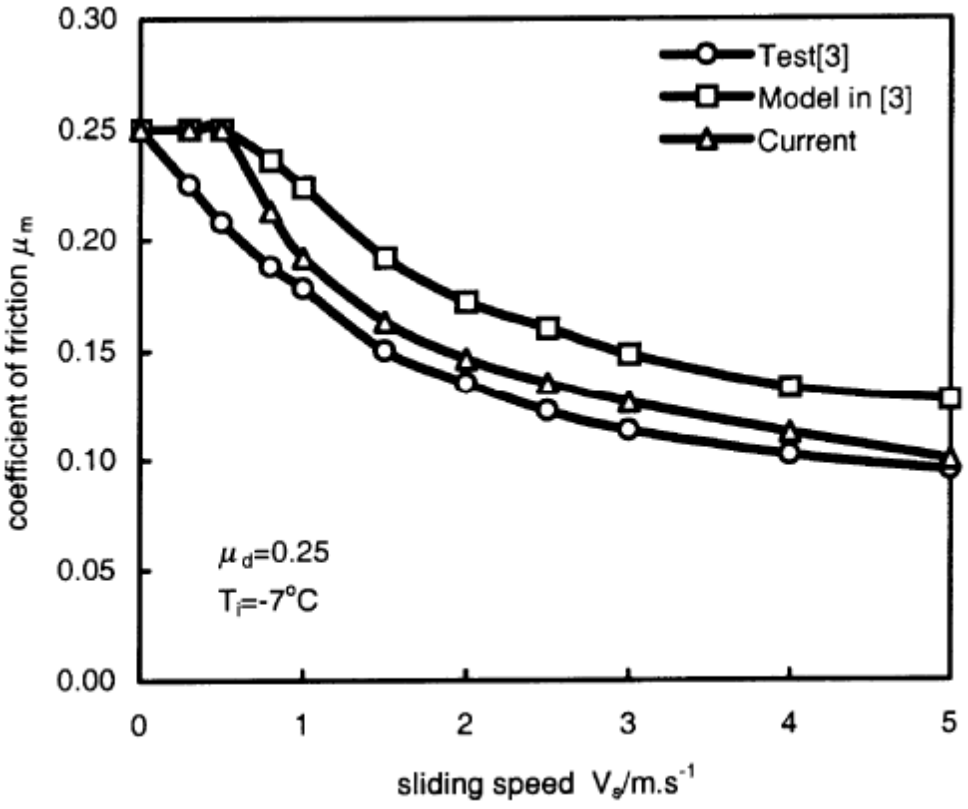

Figure 2-8. The change in the coefficient of friction versus the sliding speed [1].

The ability to manually control the translational speed of the carriage and the rotational speed of the tire means that the sliding speed and slip ratio can be manually adjusted. This would ideally allow for the comparison of the sliding speed and the slip ratio data seen in Figure 2-9 to the data obtained through the Terramechanics Rig.

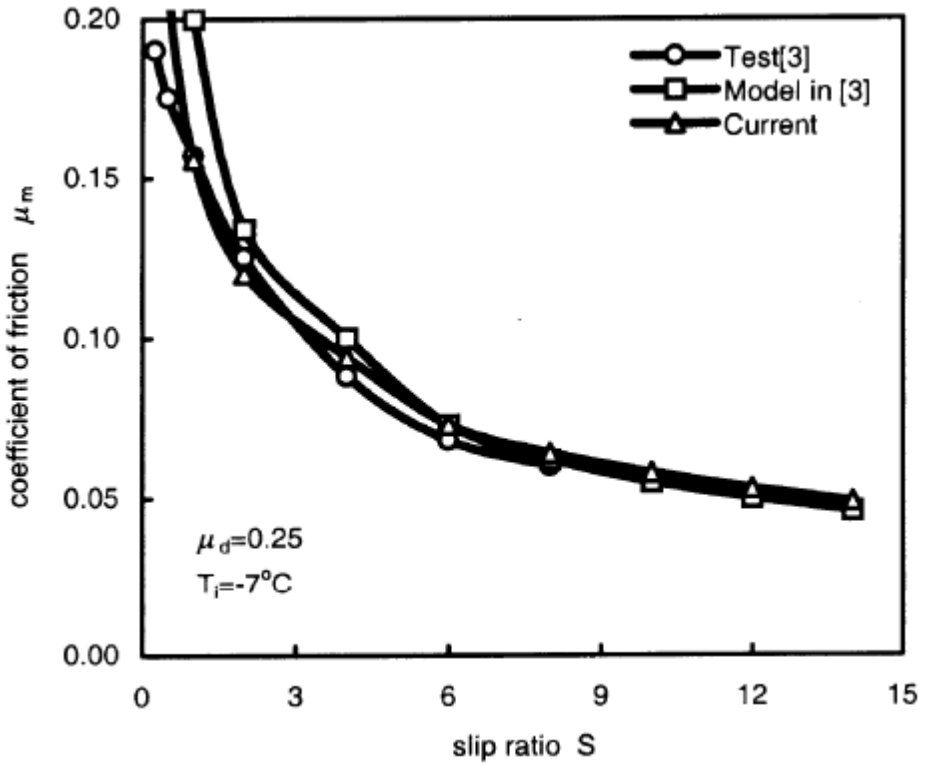

Figure 2-9. The change in the coefficient of friction with the change in slip ratio [1].

In [7] the authors also looked at the change in the coefficient of friction versus the normal pressure. One of the figures illustrating this relationship is reproduced here in Figure 2-10. The normal pressure is the normal force in the contact patch divided by the area of the contact patch. The ability to change the load in the contact patch will allow for the comparison of the normal pressure data observed from the Terramechanics Rig to the coefficient of friction data. It is estimated that at the higher end of testing, the normal pressure will be around 0.189 MPa.

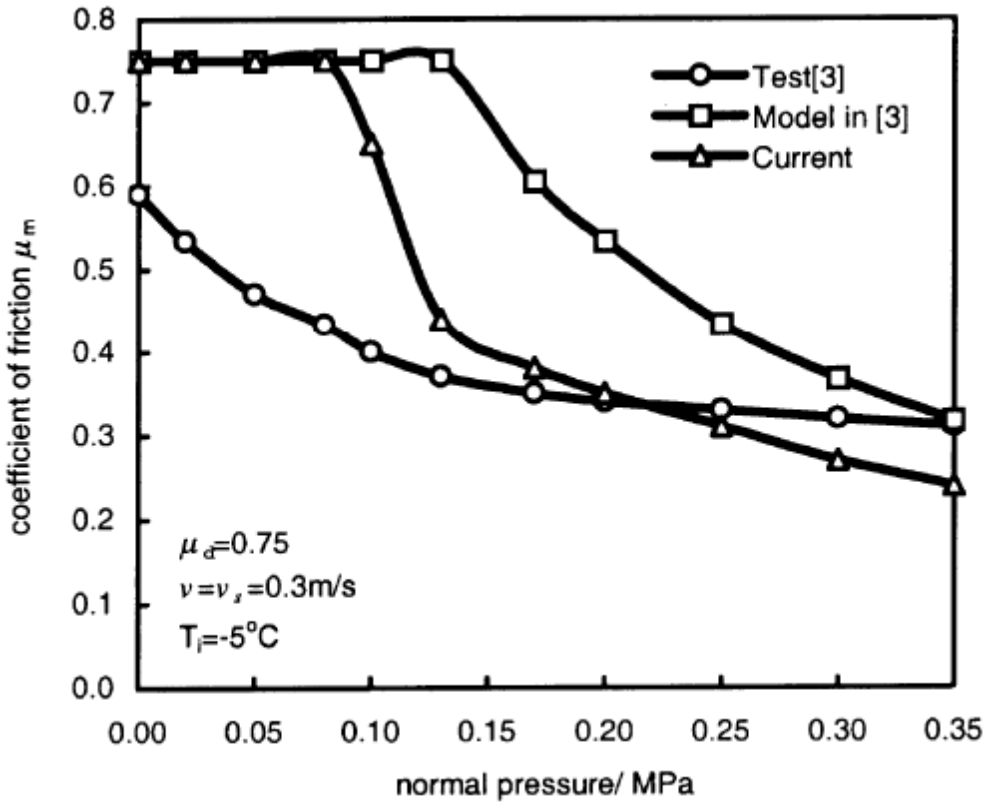

Figure 2-10. Change in the coefficient of friction versus the normal pressure. Experimental data marked by the open circles [1].

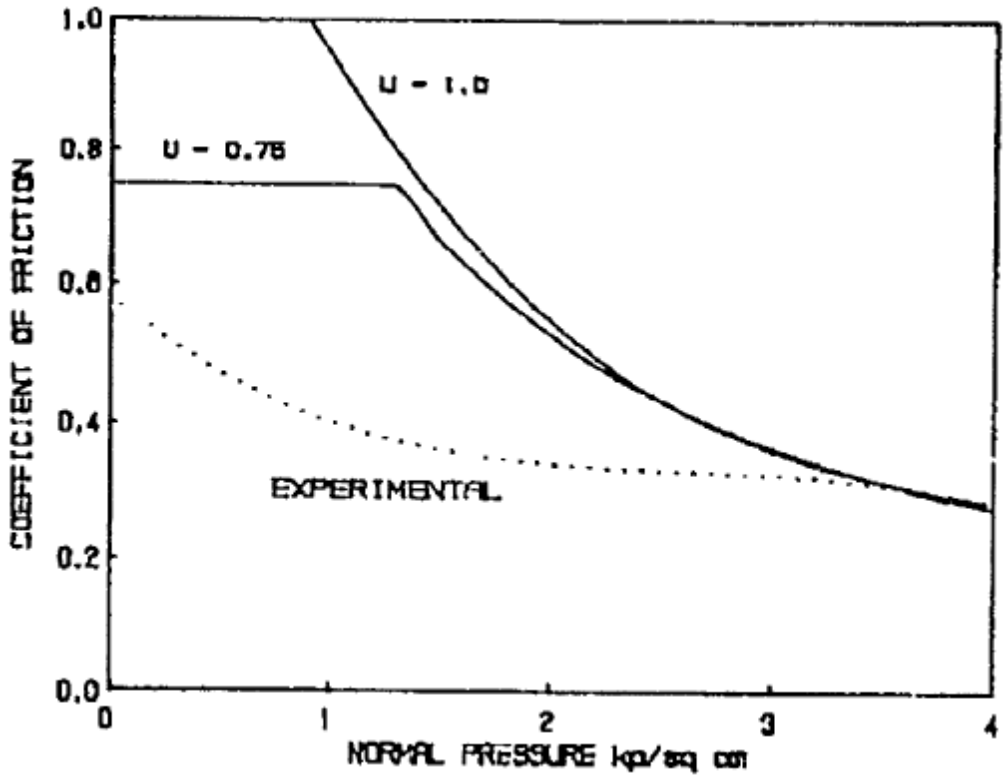

Figure 2-11. Graph of the normal pressure in kp/sq cm (kilopond per square centimeter) of a 10 sq cm rubber block. Experimental data from a 1970 study is compared to the calculations in the 1989 study, showing poor correlation between the data [8].

Similarly, in Tire Force Generation on Ice the authors used a 10 sq cm block on ice that was -5 °C (23 °F). This test was run at an equivalent velocity of 0.3 m/s, while the equivalent tangential velocity of the tire was changed. These researchers also observed that as the normal pressure increased, the coefficient of friction would decrease [8].

2.4 Review of Literature: Coefficient of Friction Models

In A Tire Traction Modeling for Use in Ice Mobile [1] the researchers made several assumptions in order to come up with a pneumatic tire-on-ice model. Their model is based on three sets of equations: conservation of mass, conservation of momentum, and energy

conservation equations. They made several assumptions that don't exist in reality but helped to develop a model that fairly accurately matched data they found in previous studies.

They assumed that the tire in their equation was rigid with a smooth surface that always remained parallel to the surface of the ice. Their contact patch was divided into two regions with dry sliding at the front of the contact patch and a wet region at the back of the contact patch, creating a film that separates the tire from the ice surface. This film was assumed to be laminar, or having parallel layers. Furthermore this fluid was assumed to be Newtonian, iso-viscous, and incompressible.

The coefficient of friction was assumed to be constant in the dry sliding region of the contact patch. The contact patch is several orders larger than the melting film thickness and the depth the heat penetrates. The heat produced by friction is one-dimensional and doesn't diffuse to the environment but is absorbed by the tire and the ice that is melted. A representation of this contact patch is given in Figure 2-12.

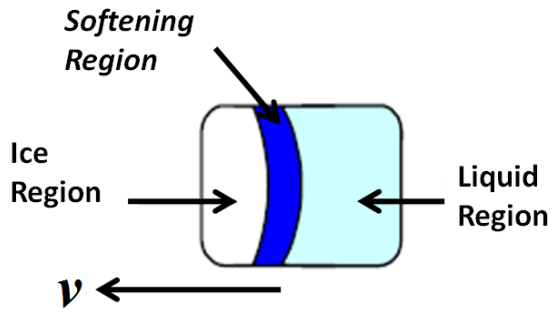

Figure 2-12. Revised schematic of the tire contact patch on ice. Determining the exact length of the softening region is currently impractical.

The coefficient of friction is derived through a series of equations. The first equation is to find the phase transition location, x_m. The second equation was used to find the film thickness, h. The final equation is used to find the average coefficient of friction, f_m. The phase transition location, x_m, was found in their previous work and is given by equation (2.1):

$$x_m = l - \frac{\pi U}{a_i}\left(\frac{\Delta T_m}{2q_d} k_i C\right)^2 \tag{2.1}$$

which requires the length of the contact patch, l; the speed of the axle, U; the thermal diffusivity of ice, a_i; and the difference between the temperature of the tire to the melting point of ice in equation (2.2), ΔT_m [3].

$$\Delta T_m = T_m - T_i = T_m - T_t \tag{2.2}$$

where the temperature of the ice, T_i, and the temperature of the tire, T_t, are assumed to be equal. Equation (2.3) below is used to define the coefficient, C, that is used in the phase transition location equation. The additional terms in the parenthesis are the frictional heat per unit dry area, q_d; the thermal conductivity of ice, k_i; and the coefficient C defined in equation (2.3):

$$C = C_t / C_i + 1 = \left(\frac{k_t}{\sqrt{\pi a_t}}\right) / \left(\frac{k_i}{\sqrt{\pi a_i}}\right) + 1 \tag{2.3}$$

The film thickness, h, can be calculated after the phase transition location using the equation (2.4)

$$C_1 - C_2 h - C_3 h^4 = 0 \tag{2.4}$$

which has numerous inputs and can be expanded to the equation below

$$\left[\eta U_s^2\right]-\left[2\Delta T_m\left(C_t+C_i\right)\left(U/x_m\right)^{1/2}\right]h-\left[\frac{p_0\rho H}{y_m\eta w^2}\right]h^4=0 \tag{2.5}$$

and solved for the film thickness, h, after all of the variables are input into the equation. This requires the dynamic viscosity of water, η; and the U_s, the sliding speed of the tire in the first set of equations.

The second set of equations uses the difference between the temperature of the tire to the melting point of ice [3], ΔT_m; the equivalent variables in equation (2.3) for the variables C_t and C_i; the speed of the axle, U; and the phase transition location, x_m, from equation (2.1).

The third set of equations requires the average pressure across the contact patch p_0, the density of water, ρ; the latent heat of fusion, H; the the dynamic viscosity of water, η; the breadth of the contact patch, w; and the coefficient y_m calculated using equation (2.6) below

$$y_m=\frac{y_{m1}}{y_{m2}} \tag{2.6}$$

and is broken down into equation (2.7) for y_{m1}:

$$y_{m1}=\frac{9}{8}\left(\theta_m+\frac{\pi}{2}\right)+\frac{1}{2}\sin\left(2\theta_m\right)-\frac{1}{32}\sin\left(4\theta_m\right) \tag{2.7}$$

and equation (2.8) for y_{m2}:

$$y_{m2}=\theta_m+\frac{\pi}{2}+\frac{1}{2}\sin\left(2\theta_m\right) \tag{2.8}$$

The variable θ_m is given below by equation (2.9):

$$\theta_m = \sin^{-1}\left(\frac{x_m - l/2}{l/2}\right) \tag{2.9}$$

With all of the variables input into the equation, the film thickness can be calculated. This value can then be input into the equation for the coefficient of friction, f_m given below

$$f_m = \frac{\eta U_s}{h}\frac{1}{p_0}\left(\frac{x_m y_{m2}}{\pi l}\right) + \frac{(\pi - y_{m2})(l - x_m)}{\pi l} f_d \tag{2.10}$$

which requires the previously stated variables and includes the dry coefficient of friction, f_d.

The researchers compared their calculated coefficient of friction against previous test data (they did not conduct tests themselves) and against a tire-on-ice model from 1989 [9]. In the comparison of the coefficient of friction versus the slip ratio, this model under-estimated the friction at lower slip ratio until a slip ratio of 4, while the older tire model more closely matched the test data but over-estimated the slip ratio until it reached a slip ratio of 4 [10].

The coefficient of friction was also compared against the sliding speed of the tire, U_s. In this case, the researchers' tire model more closely matched the test coefficient of friction, although slightly underestimating it (within a coefficient of friction of 0.01). The older tire model overestimated the coefficient of friction with a coefficient of friction greater than 0.01. For example, this means that for a sliding speed of 5 m/s, the test gave a coefficient of friction of 0.100 versus the older tire model giving a value of around 0.115.

They also compared their calculations of the coefficient of friction of a rubber block on ice versus the normal pressure, or the average pressure across the contact patch. Both models

greatly over-estimated the actual coefficient of friction from 0 to approximately 0.16 MPa (23.21 psi), but the researchers' model more closely matched the rubber slider. After 0.20 MPa (29.01 psi) the researchers' model did go below the observed values of the slider tests, giving a coefficient of friction at 0.35 MPa (50.76 psi) that was approximately 0.05 smaller than the actual value [10].

A year later the same researchers revised their previous tire model to create a simpler and more accurate tire friction model. In A New Method for Determining Tire Traction on Ice [2] the authors of [1] changed their previous assumptions and made a few new assumptions. They kept the idea that the tread was rigid and that its surface was perfectly smooth; the coefficient of friction was constant in the dry sliding region of the interface; the heat created by friction in the contact patch was considered to only flow into the ice and the tire, not the surroundings.

Their first new assumptions were that the contact pressure distribution was uniform across the interface. They called the region between the liquid and dry contact portions of the contact patch the melting region and assumed that the temperature stayed at the melting point of ice. The temperature of the tire and the ice surfaces was assumed to be equal to the bulk ice temperature (equilibrium temperature of the ice).

In order to derive their new coefficient of friction, they went through a series of derivations to determine the coefficient of friction in the contact patch. In addition, they created two equations for the coefficient of friction, one with a rectangular contact patch and one with an elliptical contact patch. The frictional heat generated in the dry region is given by equation (2.11) below

$$Q_d = \int_0^{x_m/v} q_d dt = \mu_d p_{av} s x_m \tag{2.11}$$

where the frictional heat per unit area in time is integrated from 0 seconds to the time given by dividing the length of the dry contact region, x_m, by the traveling speed of the vehicle, v. The integral equates to the dry coefficient of friction, μ_d, multiplied by the average contact pressure, p_{av}, the slip ratio, S, and the length of the dry contact region, x_m.

Similar to the frictional heat generated in the dry region, the frictional heat generated in the entire contact patch, Q_m, is given by equation below

$$Q_m = \mu_m p_{av} s l \tag{2.12}$$

which contains the average coefficient of friction across the entire contact patch, μ_m, instead of the dry region; and the length of the entire contact patch, l.

The total quantity of heat transferred from the melting patch into the tire, Q_t, is given by the equation (2.13) below

$$Q_t = 2k_t \Delta T_m \left(\frac{l - x_m}{\pi \alpha_t v} \right)^{1/2} \tag{2.13}$$

which requires the thermal conductivity of the tire, k_t; the difference between the temperature of the melting point of the ice and the temperature of the tire, ΔT_m; the total length of the contact patch, l; and the thermal diffusivity of the tire, α_t.

The total quantity of heat transferred from the melting patch into the ice, Q_i, is given by the equation (2.14) below

$$Q_i = 2k_i \Delta T_m \left(\frac{l - x_m}{\pi \alpha_i v} \right)^{1/2} \tag{2.14}$$

which requires the thermal conductivity of the ice, k_i; the difference between the temperature of the melting point of the ice and the bulk temperature of the ice, ΔT_m; the total length of the contact patch, l; and the thermal diffusivity of the tire, α_i.

Using the principle of thermal balance, the researchers derived equation (2.15) that was used to create the final equation for the coefficient of friction.

$$\left(Q_t + Q_i\right)\left(l - x_m\right)w = \left(Q_m - Q_d\right)\left(l - x_m\right)w \tag{2.15}$$

Inserting equations (2.13), (2.14), (2.12), and (2.11), respectively, into equation (2.15) for each of the heat generated terms, allows the equation to be rearranged in order to give the coefficient of friction for a rectangular contact patch below:

$$\mu_m = \mu_d \left(\frac{x_m}{l} \right)^2 + \left(\left(\frac{2k_i}{\sqrt{\pi \alpha_i}} \right) + \left(\frac{2k_t}{\sqrt{\pi \alpha_t}} \right) \right) \bullet \left(T_m - T_i\right) \left(1 - \frac{x_m}{l}\right)^{\frac{3}{2}} \left(\frac{l}{v} \right)^{\frac{-1}{2}} \left(p_{av} v_s\right)^{-1} \tag{2.16}$$

For the elliptical contact patch, the researchers used their own equation for an ellipse

$$\frac{\left(x - l/2\right)^2}{\left(l/2\right)^2} + \frac{y^2}{\left(w/2\right)^2} = 1 \tag{2.17}$$

to derive the area to be substituted into equation (2.15). From the new equation, equations (2.13) , (2.14), (2.12), and (2.11), respectively were inserted into each of the heat generation variables to provide the coefficient of friction for an elliptical contact patch,

$$\mu_m = \mu_d \left(\frac{x_m}{l} \right) y_{1\,m} + \left(\left(\frac{2k_i}{\sqrt{\pi \alpha_i}} \right) + \left(\frac{2k_t}{\sqrt{\pi \alpha_t}} \right) \right) \bullet (T_m - T_i) \left(1 - \frac{x_m}{l} \right)^{\frac{1}{2}} \left(\frac{l}{v} \right)^{\frac{-1}{2}} (p_{av} v_s)^{-1} y_{2\,m} \tag{2.18}$$

where the equation for the first y variable is

$$y_{1\,m} = \frac{1}{2} + \frac{\left[\arcsin\left(\frac{2x_m}{l} - 1 \right) \right]}{\pi} + \frac{1}{2\pi} \sin\left(2 \left[\arcsin\left(\frac{2x_m}{l} - 1 \right) \right] \right) \tag{2.19}$$

and the equation for the second y variable is

$$y_{1\,m} = \frac{1}{2} - \frac{\left[\arcsin\left(\frac{2x_m}{l} - 1 \right) \right]}{\pi} - \frac{1}{2\pi} \sin\left(2 \left[\arcsin\left(\frac{2x_m}{l} - 1 \right) \right] \right) \tag{2.20}$$

In the case of a wheel spinning, or the axle velocity equaling zero and a positive nonzero sliding speed, the researchers' derived another coefficient of friction for the fluid frictional resistance:

$$\mu_f = \frac{\left(\frac{2k_i}{\sqrt{\pi \alpha_i}} \right) \left(\left[\frac{2k_t}{\sqrt{\pi \alpha_t}} \right] / \left[\frac{2k_i}{\sqrt{\pi \alpha_i}} \right] + 1 \right) (T_m - T_i)}{p_{av} \sqrt{l v_s}} \tag{2.21}$$

The researchers compared the coefficient of friction of the rectangular contact patch of their new model versus the data from Hayhoe and Shapley's model from 1989. In a comparison of the coefficient of friction versus the sliding speed, the new model slightly overestimated the actual

data from the 1989 study, while the model from that older study overestimated the coefficient of friction by a value of approximately 0.04 to 0.05.

The coefficient of friction of the rectangular contact patch compared to the slip ratio showed that the new model very closely matched the data observed in 1989. The older tire friction model from 1989 followed the shape of the data, but did not match the data as well as the researchers' model.

The researchers also did a test of the coefficient of friction versus the pressure in the contact patch of a rubber block [1]. Their new model again more closely matched this data compared to the Hayhoe and Shapely model, but both models did not accurately follow the curve of the actual data, as seen in Figure 2-13. One reason for this may be the nature of a rubber block versus a rotating tire.

The study conducted by James Lacombe in Tire Model for Simulations of Vehicle Motion in High and Low Friction Road Surfaces [11] presented two different approaches to modeling a tire on an ice surface, because of the differences between the analysis of the lateral coefficient of friction and the longitudinal coefficient of the tire friction model. The lateral coefficient of friction was modeled through the use of the elastic beam theory by Timenshenko, with the shear force coming from tire to surface friction. The longitudinal coefficient of friction was modeled using the "Brush" model, also knows at the "Cantilevered Spoke" model. This model used a 2-dimensional contact patch with cantilevered spokes, shown in Figure 2-13. The contact patch was divided into two regions: the "static" region and the "slide" region, where the tire adheres to the dry ice surface and then slides on the on the slick ice, respectively [11].

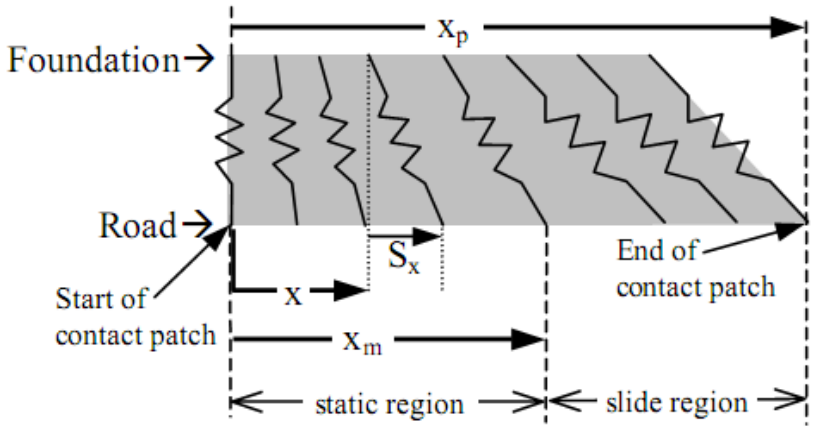

Figure 2-13. Diagram of the Brush model, with the tire rotating counterclockwise, or rolling to the left.

In the tire contact patch, the distance x is the length of leading edge of the contact patch to the first portion of the contact patch where the tire tread begins to stretch. The length of the "static" region is given the term x_m. The stretching term S_x is

$$S_x = \left(1 - \frac{V_x}{\omega R}\right) x \tag{2.22}$$

which has the inputs of the wheel rotation rate, ω, the tire rolling radius, R, and the velocity of the wheel center moving in the longitudinal direction, V_x [11]. This stretching term multiplied by the integration of the foundation stiffness, C_1, over the distance x = 0 to x = x_m creates an equation for the static region longitudinal friction force

$$f_{x,st} = \frac{C_1}{2}\left(1 - \frac{V_x}{\omega R}\right) x_m^2 \tag{2.23}$$

The tire foundation stiffness, C_1, is an empirical number that can obtained from a static pull test. The test is used to measure the longitudinal load and the displacement of the tire contact patch.

The slope of this resulting curve is calculated, and the value is divided by the length of the contact patch in order to determine a value for the foundation stiffness.

In the "slide" region of the tire contact patch the author assumed that the tire tread sliding properties were isotropic or uniform in all directions. This allowed for the use of a coefficient of friction, μ, that could be utilized to define the net sliding friction force vector, $f_{xy,sl}$, that would act in the opposite direction of the tire sliding motion. The magnitude of this force is equal to the product of μ and the normal force acting in the slide region, calculated with

$$f_{xy,sl} = \mu \frac{F_z \left(x_p - x_m \right)}{x_p} \tag{2.24}$$

which has the inputs of the normal force, F_z, the length of the contact patch, x_p, and the length of the static region of the tire contact patch, x_m.

In the longitudinal direction, or the x-axis, the sliding friction force, $f_{x,sl}$, is calculated using

$$f_{x,sl} = \left[\frac{\omega R - V_x}{\left(V_x^2 \mathrm{Tan}^2 \left(\alpha \right) + \left(\omega R - V_x \right)^2 \right)^{1/2}} \right] \mu \frac{F_z \left(x_p - x_m \right)}{x_p} \tag{2.25}$$

where the top line of the brackets, $\omega R - V_x$, is the sliding velocity in the x axis and the term on the bottom is the square root of the addition of the squares of the lateral direction and the of the longitudinal direction. This was derived from the concept of a "friction circle," which is actually shaped like an ellipse.

The current setup of the Terramechanics Rig does not allow the slip angle to be tested, only the toe angle. In this case, equation (2.25) can be reduced by setting the slip angle to zero in order to eliminate the tangent term. The new longitudinal sliding friction force becomes

$$f_{xy,sl} = \left[\frac{\omega R - V_x}{\left(\left(\omega R - V_x \right)^2 \right)^{1/2}} \right] \mu \frac{F_z \left(x_p - x_m \right)}{x_p} \tag{2.26}$$

which reduces to an equation that is equivalent to the net sliding force friction vector

$$f_{x,sl} = \mu \frac{F_z \left(x_p - x_m \right)}{x_p} \tag{2.27}$$

2.5 Review of Literature: Slip Ratio of Preceding Models

In the two preceding SAE models, the authors use a slightly different definition of the slip ratio. The slip ratio itself is a way to express the wheel velocity in relation to the vehicle velocity. The slip ratio, s, in the preceding literature was determined using equation (2.28) below:

$$s = \frac{U_c - U}{U} = \frac{U_s}{U} \tag{2.28}$$

where U_c is the tangential velocity of the tire (specifically the tread elements), U is the velocity of the axle. These equate to the speed of the tire, U_c, and to the actual speed of the vehicle, U. Subtracting the tangential velocity of the tire from the axle velocity ($U_c - U$) gives the sliding speed of the tire, U_s [10]. This slip ratio is similar to other definitions of the slip ratio given in

some vehicle dynamics books, with differences coming from the points of reference. A common method of determining the slip ratio in vehicle dynamics books is given in equation (2.29) below. The slip ratio, SR, in this equation is calculated from the angular velocities of the driven wheel, Ω, and the free-rolling wheel Ω_0 (no reference to the tire) [12].

$$SR = \frac{\Omega - \Omega_0}{\Omega_0} = \frac{\Omega}{\Omega_0} - 1 \tag{2.29}$$

3 Background of Pneumatic Tires: Tire Design & Mechanical Properties

The wheel was being used long before any tires were ever invented. The earliest depiction of the wheel is on a ceramic vase from around 3500 BC (called the Bronocice pot). Spoke wheels were invented a few thousand years later. One of the main methods of protecting the wheel, essentially a form of tire, was through the use of an iron rim around 1000 BC created by the Celtics [13]. Another method included leather, used by the Sumerians around 2500 BC. A wooden tire was created for chariots in ancient Egypt around 1500 BC. These tires consisted of strips of wood affixed to the wheels through leather bindings. These construction methods were used on and off again for centuries until the 19th century.

Charles Goodyear's invention of vulcanization, or the addition of sulfur to natural rubber with a long heating process, allowed for the usage of vulcanized rubber as a covering for the wheel. He claims to have invented vulcanized rubber in 1939, and was later awarded U.S. Patent # 3,633 for his invention. This lead to the creation of solid tires, and lead to experiments with vulcanized rubber that eventually produced pneumatic tires.

In 1846 Robert William Thomson created and was granted a patent for the pneumatic tire in France, and then in the United States in 1847. This was demonstrated briefly on horse drawn carriages but the lack of thinner rubber impeded the widespread usage of the pneumatic tire. In 1887 John Boyd Dunlop invented a pneumatic tire for a bicycle. Unaware of Thomson's invention he tried to file for a patent. His patent was denied but in 1988 he went on to produce the first commercial pneumatic tires [14].

The pneumatic tire is a complex piece of equipment. Since its introduction, its design has been added onto and modified for over 100 years. Pneumatic tires are used on many different

vehicles in order to provide traction, ride comfort, and improve handling. These vehicles include bicycles, motorcycles, tractors, other agricultural equipment, passenger cars, trucks, semi trucks, busses, and airplanes. In recent years, automobiles have accounted for more than 55 percent of pneumatic tires produced [15].

The tire is usually the only part of a vehicle touching the ground. This means that the tire has major effects on the handling of the vehicle, along with transmitting and dampening the forces exerted on the road to the vehicle itself. In a pneumatic tire 5% of the vehicle's weight is supported by the tire sidewall, while 95% of the vehicle's weight is supported by the air pressure contained inside the tire [16]. While supporting this weight, the tire controls the heading of the vehicle, and its traction and stability. Each tire has to operate for many thousands of miles while withstanding road irregularities, changes in temperature and environment, and the forces coming from the vehicle in stationary and moving conditions [17].

Winter tires have to take into account these concerns while dealing with extreme cold and low-friction surfaces. Snow tires have been developed that are able to provide a relatively high kinetic coefficient of friction in for pneumatic tires in snow of 0.20 compared to around 0.03 for tires on ice [18]. These tires dig into the snow with their large tread extensions, lugs, and wide gaps that allow snow to be grasped and released as a vehicle is driven through snow. Designing pneumatic tires for increased traction in snow, by increasing the friction between the tire and snow, has the inverse effect of reducing the friction of the tire on ice. In fact a tire tread design with smaller grooves is proven to work better on ice than one with large grooves.

3.1 Tire Nomenclature

Pneumatic tires are marked with a code on their sidewall that tells the user what size the tire is and different aspects about the tire. There are two systems of tire size nomenclature: P-metric, a system used within the United States, and Euro-metric. In P-metric, the P stands for passenger vehicles—the intended usage of these tires. The Euro metric has an identical code except for the "P" in front of the indicator and a different load capacity.

P-metric tires are rated slightly lower than their Euro-metric counterparts. Even with the same physical dimensions, the two tires use different load capacity calculations and inflation pressure tables. From these differences, the Euro-metric tires are rated slightly higher than P-metric tires with "standard" load range tires using a load pressure of 36 psi compared to P-metric tires using 35 psi. At the higher end, Euro-metric "extra load" tires are rated at 42 psi while P-metric "extra load" tires are rated at 41 psi [19].

The first part of the tire code is the tire section width; the second portion is the aspect ratio; the third portion of the code is the construction; the fourth portion the wheel diameter; and the optional fifth and sixth position are known as the load index and the speed rating. The tire section width is the measurement of the tire's width from sidewall to sidewall. The aspect ratio is the ratio of the cross-sectional height of the tire to its tire width measurement [20]. The construction refers to the type of ply that the tire is designed with: "B" for bias-belted, "D" for diagonal or bias ply, "R" for radial ply [21]. The wheel diameter refers to the diameter of the wheel—which is the size of the wheel that the tire was intended to fit on [20]. Additionally, tires sold in the United States are marked with a Department of Transportation (DOT) Serial Number that indicates the tire's conformance to the United States DOT's tire safety standards.

3.1.1 Tire Nomenclature: Tire Section Width

The tire section width is measured from sidewall to sidewall in millimeters. This measurement actually changes depending on the rim that the tire is mounted to. There is no specific guideline to what rim to use, and this is left up to the manufacturer's discretion. The industry's rule of thumb is that the tire section width changes approximately 2/10" (5.08 mm) per half inch change in the rim width. This can be noted in Table 3-1 for the example of a P205/60R15 size tire, which has a width of 205 mm on a 6 inch rim.

Table 3-1. Table of the measured section width compared to the change in the rim width [22].

Difference from Measuring Rim (in)	Rim Width (in)	Approximate Tire section width (in)
-0.5 (narrower)	5.5 in	8.03
Measuring Rim	6.0 in	8.23
0.5 (wider)	5.5 in	8.43
1.0 (wider)	6.0 in	8.63
1.5 (wider)	5.5 in	8.83

3.1.2 Tire Nomenclature: Aspect Ratio

The aspect ratio is the ratio of the cross-sectional height of the tire to its tire width measurement [20]. The aspect ratio provides the height of the cross section by calculating the value from the percentage of the section width (measurement from sidewall to sidewall) based on the rim selected by the manufacturer to measure the section width [22]. Using the previous

example of a 205 mm section width tire, with an aspect ratio code of 60 or 60%, the calculated cross-sectional height of this tire would be 123 mm [20].

3.1.3 Tire Nomenclature: Maximum Load

The maximum load of a tire is usually printed near the tire's bead, or the portion of the sidewall near the inner radius of the tire. As tires are a worldwide product, the maximum load is given in kilograms and pounds. For consumer tires, this value falls into two categories of tire load ranges: light truck and p-metric designs. Light truck tires have much higher inflation pressure ranges for their maximum loads and can carry a higher maximum load than P-metric tires. The passenger vehicle tires, or P-metric tires, are found on passenger vehicles and are rated to handle 100% of the load printed on the sidewall of the tire [22].

The difference in the load ranges between these tires comes from the internal construction. Two tires that look identical on the outside may actually be rated at two different loads because of stronger internal construction on one tire allows it to handle more air pressure which in turn allows it carry more weight. Furthermore the inflation pressure at the maximum load and the maximum inflation pressure are usually two different figures. A tire can be rated for a much higher maximum inflation pressure such as 42 psi, while the inflation pressure at maximum load may be 35 psi [22].

3.1.4 Tire Nomenclature: Construction Code Indicator

This alphabetical portion of the code gives the construction type of the pneumatic tire. There are usually three different letters that can be used here: "R," "B," and "D." Radial ply tires, or tires with laterally lined internal plies, are indicated by the "R." Belted bias ply tires, or tires with crisscrossed internal layers are indicated by the "B." The simpler bias-ply design is

indicated by the capital letter "D," indicating the diagonal plies of the design [21]. Simplified diagrams of these designs are seen in Figure 3-1.

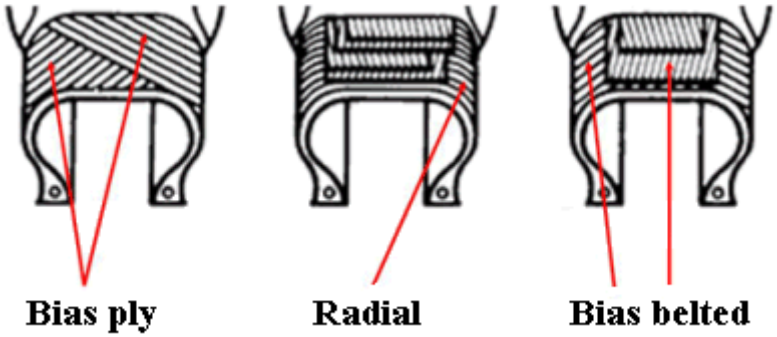

Figure 3-1. Cutaway of "diagonal" bias-ply tire, radial-ply tire, and the "bias-belted" or belted-bias tire [23].

3.1.5 Tire Nomenclature: Wheel Diameter

The wheel diameter is the measurement of the outer diameter of the wheel that the tire was designed to fit. This measurement is given inches. In the example tire, P205/60R15, the wheel diameter, or diameter of the rim, is 15 inches. To find the diameter of the tire, it must be calculated from the section aspect ratio to find the section height, then added to the wheel diameter [24]. In the example tire, the calculated cross-sectional height of this tire was 123 mm or 4.84 inches. Adding up the sectional height of the both ends of the tire and the diameter of the wheel—4.84, 4.84, and 15 inches—gives a diameter of 24.86-inch for the tire.

3.1.6 Tire Nomenclature: Load Index

The load index indicates the tires load carrying capacity, or the maximum load the individual tire can carry. Using the example tire, with a "standard load" capacity or load index of 84, the tire would be capable of supporting a mass of 1,102 pounds (500 kg) [25]. All P-metric tire is measured at "standard load" with an inflation pressure of 35 psi. The Euro-metric tires are measured at a "standard load" with an inflation pressure of 36 psi. The load index values and their carrying capacity are indicated in Table 3-2.

Table 3-2. The P-metric load index table.

Load Index	Pounds	Kilograms	Load Index	Pounds	Kilograms
71	761	345	91	1356	615
72	783	355	92	1389	630
73	805	365	93	1433	650
74	827	375	94	1477	670
75	853	387	95	1521	690
76	882	400	96	1565	710
77	908	412	97	1609	730
78	937	425	98	1653	750
79	963	437	99	1709	775
80	992	450	100	1764	800
81	1019	462	101	1819	825
82	1047	475	102	1874	850
83	1074	487	103	1929	875
84	1102	500	104	1984	900
85	1135	515	105	2039	925
86	1168	530	106	2094	950
87	1201	545	107	2149	975
88	1235	560	108	2205	1000
89	1279	580	109	2271	1030
90	1323	600	110	2337	1060

P-metric tires used on passenger cars and station wagons are rated to carry 100% of the load indicated on the tire's sidewall (or listed for the tire in industry load/inflation charts). However, if the same P-metric tires are used on light trucks, (pickup trucks and sport utility

vehicles for example), their carrying capacity is reduced to 91% of the load indicated on the tire's sidewall. This reduction in load results in causing light truck vehicle manufacturers to select proportionately larger P-metric sized tires for their vehicles to help offset the forces and loads resulting from a light truck's higher center of gravity and increased possibility of being occasionally "overloaded."

3.1.7 Tire Nomenclature: Speed Rating

The speed rating tells the user the maximum operating speed of the tire. Originally developed in Europe, the speed ratings are at relatively high speeds, far above the speed limits in most areas of the United States. The ratings are indicated by the letters in the chart in

Table 3-3. If the example tire had a speed rating of "U," the maximum operating speed would be 124 mph based on the construction of the tire. The rating of "U" is also applicable to light trucks [26]. These speed ratings are based on the maximum operating speed tested by the manufacturer.

Table 3-3. Speed rating chart providing the maximum operating speed and showing the division between passenger vehicles and light trucks [26].

SPEED SYMBOL	MAXIMUM SPEED	APPLIES TO PASSENGER CAR TIRES	APPLIES TO LIGHT TRUCK TIRES
*	above 149 mph (240 km/h)	YES	-
Y**	186 mph (300 km/h)	YES	-
W**	168 mph (270 km/h)	YES	-
V (with service description)	149 mph (240 km/h)	YES	-
H	130 mph (210 km/h)	YES	YES
U	124 mph (200 km/h)	YES	YES
T	118 mph (190 km/h)	YES	YES
S	112 mph (180 km/h)	YES	YES
R	106 mph (170 km/h)	-	YES
Q	99 mph (160 km/h)	-	YES
P	93 mph (150 km/h)	-	YES
N	87 mph (140 km/h)	-	YES
M	81 mph (130 km/h)	YES Temporary Spare Tires	-

3.2 Tire Nomenclature

Goodyear provided two tires to test on the Terramechanics Rig, . Both tires are identical except for their tread patterns. The “bald” tire had a smooth surface without any tread pattern, and the other tire had a generic winter tire tread pattern according to Goodyear. These tires came marked with the tire code “P255/55R18 104 H” with P indicating that they are passenger vehicle tires, seen in Figure 3-2.

Figure 3-2. View of the tire code on the pneumatic tire with winter tire tread pattern.

The 255 indicates a tire section width of 255 millimeters and the aspect ratio value of 55 indicated a calculation of 255 multiplied by 0.55 for a section height of 140.25 millimeters. The "R" letter indicates a radial-ply tire construction. The "18" is a wheel diameter of 18 inches or the diameter of the rim that the tire has been measured for. The load index is 104, which indicates a maximum load of 1984 lbf (900 kg). The speed rating of H indicates a tested max operating speed capability of 130 mph (210 km/h) and is designed for coupes and sport sedans [25]. According to Goodyear the sidewall is a VSB or Vertical Serrated Band sidewall [27]. This is simply the design of the sidewall seen in Figure 3-3.

Figure 3-3. Vertical Serrated Band (VSB) sidewall design [27].

3.3 Tire Construction

The modern pneumatic tire is a complex design. It features numerous layers starting from the sides with the bead and bead chaffers and sidewall; to the layers that compromise the contact patch and thread: the radial plies, steel belts, cap plies, and the shoulder. There are two main types of ply construction: bias ply and radial ply. The former came about from the formation of The Goodyear Rubber & Tire Company in 1898 [28]. The first radial ply tire was invented by Arthur W. Savage and granted a patent in 1916 [29]. In 1946 Michelin patented the steel-belted radial tire and introduced it to the consumer in 1948 [30].

Bias ply tires are constructed in layers of diagonal cords, where each successive ply layer crisscrosses the previous layer, and the rubber is embedded into and on top of these layers [28]. The cord or crowd angle is usually between 30 to 40 degrees [15]. The crowd angle is a measurement of the angle of the cords based on a peripheral line around the tire [31]. This allows the entire body of the tire to flex easily, giving it a smoother ride on rough surfaces in comparison to radial ply tires. The name "bias" comes from clothing since the pattern of the bias ply tire is similar to a woven fabric with diagonal lines [32]. For the first half of the 20th century, this tire was in widespread usage in passenger vehicles, before being superseded by radial tires.

Radial ply tires are constructed in parallel layers of plies, as seen in Figure 3-4. The cords that make up each ply layer run perpendicular to the bead at the edge of the tire. The design is supposed to reduced the friction between the plies and in turn reduce the rolling friction of the tire [33]. Compared to bias ply tires, they have a wider and more rectangular contact patch than and better ground pressure distribution. These features give radial tires better steering characteristics, distributed wear for longer tread life, and increased gas mileage than bias ply tires. The disadvantage of the design is that it is more complex and more expensive to produce and the ride quality is harsher or more stiff than bias ply tires [28].

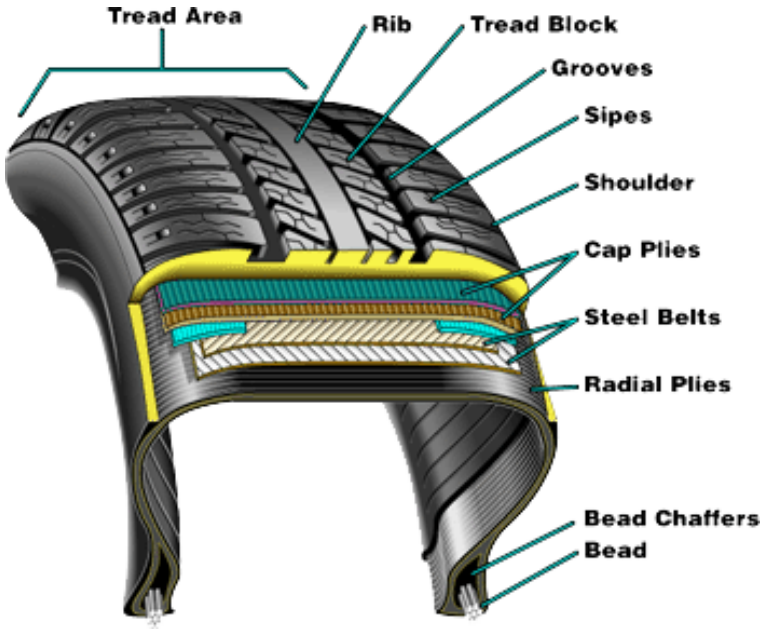

Figure 3-4. Schematic of the layers of a radial-ply pneumatic tire [34].

3.3.1 Tire Construction: Tread

The tread is the part of the tire that makes physical contact with the road surface. The tread is usually a thick rubber, or rubber/composite compound that has been formulated to give an application-specific appropriate level of traction and to not wear away quickly in this application. Over time different tread designs have been designed and tested, creating the generally geometrical shape of the lugs and voids formed by grooves, slots, and sipes [31].

Lugs are the part of the tire tread that stick out and actually make contact with the road surface. Non-symmetrical lug sizes around the circumference of a tire allow it to minimize noise levels at discrete frequencies the tire will experience in motion [31]. Voids are the spaces between the lugs and allow the lugs to flex [35]. Grooves are used to channel away water and run circumferentially around the tire. Sipes are valleys cut across the tire, almost perpendicular to the grooves and allow the water displaced by the grooves to escape from the sides of the tires. These sipes essentially create an edge on the tire that can cut and dig into a surface as seen in Figure 3-5 [35]. Cutting sipes into the tire has been found to increase traction on practically all road surfaces, notably and including wet roads, snow roads, and icy roads. As such, this design is usually found on snow or winter tires.

It has been theorized that the process of siping was invented in the 1920's by John Sipe, a slaughterhouse worker. Sipe's rubber-soled shoes continuously slipped on the wet and bloody floor of the slaughterhouse so he decided to try cutting thin slits into the rubber sole. He soon realized that "siping," or cutting these thin slits into rubber, could also be applied car tires to improve their traction. He patented the process but the idea took around 30 years to catch on.

Figure 3-5. Picture of the lateral sipes on an offroad tire.

A thirty-year old study by the US National Safety Council found that siping improved rolling traction on "glare ice" by 28 percent. The main drawback to this technique is that the sipes increase road noise and tire wear when a vehicle with the tires is just ran on a dry surface. Furthermore Consumer Reports does not recommend the practice because of those issues. Some companies such as Les Schwab believe that microsiping extends the life of a tire claiming that it reduces tire friction heat and wear. Winter tires, specifically snow tires, from Michelin and Bridgestone come siped from the factory. It has been observed that smaller sipes can be cut into tires any tire without negatively affecting the performance of that tire. This practice of microsiping, or cutting smaller sipes, usually a few millimeters in diameter, has even developed into an aftermarket.

The opposite of having all these geometric patterns in tires are treadless tires or usually called racing "slicks." On a dry surface racing slicks give the maximum traction of any tire design, but will have extremely poor traction on the slightest of wet surfaces.

3.3.2 Tire Construction: Belt

All radial ply tires utilize one or more belts, as seen in Figure 3-6. These belts increase the tire stiffness to ensure that the tire maintains its rigidity in the contact patch. In other words this maintains the contact between the tire tread and the road surface. Similar to a bias ply tire, the cords of the belt are angled but to a lesser degree, usually at a crown angle of 20 degrees [31].

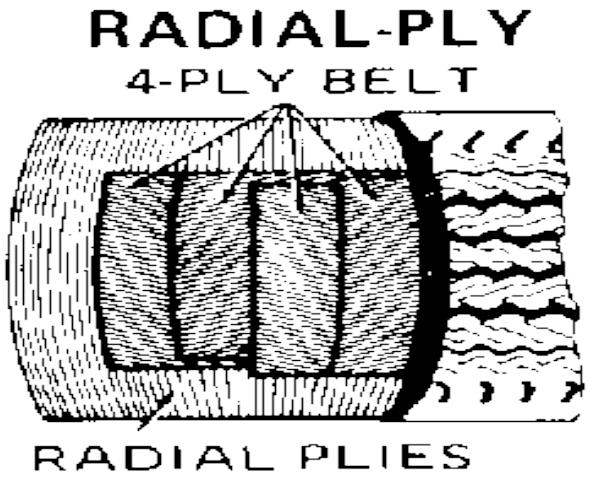

Figure 3-6. Illustration of the cords of the belt in a radial ply tire design [36].

3.3.3 Tire Construction: Breaker & Carcass

The breaker is located in between the tire tread/belt layer and the carcass of the tire. It is used for load impact softening while driving. This layer is created from rubberized plies formed

from steel or textile cord [37]. The carcass provides the shape of the pneumatic tire, and is the main load-bearing member. The semi-rigid frame of the carcass traps the compressed air trapped inside the tire. This compressed air and the structure of the tire absorb imperfections in the road, changes in the height of the road, and diffuse the vibrations caused by these imperfections. It consists of one or several plies of steel cord attached to the beads of the tire. The steel cord is covered in rubber to create each finished ply [38].

3.3.4 Tire Construction: Bead Wire

The bead functions as an anchor for the carcass and the sidewall. The steel cord that forms the bead is covered in the same rubber as the rest of the tire. The bead forms the inside loop of the tire and fits directly against the wheel or rim in order to transfer some of the load of the tire to the wheel [38].

3.3.5 Tire Construction: Sidewall

The sidewall is a more flexible and crack resistant rubber that covers the side of the carcass. It also covers part of the breaker that extends to the side of the tire. Its main purpose is to protect the side of the tire from damage [38]. This allows the sidewall of a radial-ply tire to flex independently of the tire tread. This ensures that there is less distortion of the tire contact patch and ensures a uniform tire contact patch. Comparing a radial-ply tire to a bias-ply tire, this makes for a wider, flatter, and more stable contact patch [33]. This also means that the tire has a better ground pressure distribution to ensure uniform friction and better traction [39].

3.3.6 Tire Construction: Tire Casing, Shoulder, and Crown

The tire casing is a definition of the main body of the tire separate from the tire tread. It's formed by the complete composite of plies of the tire without the layers that contain the tread pattern [40]. The shoulder is part of the tire measured from the outer edge of the tire to the sidewall of the tire [38]. In a simplified model, the material of the shoulder acts like a linear spring. The crown is the portion of the tire that contains the tread. This creates the contact patch when the tire is making contact with the ground [38].

3.4 Tread Pattern Construction

The tire tread is the portion of the pneumatic tire that makes physical contact with the road surface. As such, the geometrical construction of the tire tread is based on the environment the tire will be used in. Over time different tread designs have been designed through trial-and-error and some analysis for different operating conditions, creating the plethora of shapes that make up the contact patch. These geometrical shapes are classified as "grooves, lugs, voids, and sipes."

The grooves are literally grooves that wrap around the circumference of the tire. These grooves are used to channel away rain water, or melted snow and ice, from the center of the contact patch. The effect is usually seen as water being sprayed from the back of the contact patch as the tire moves forward. The lugs are the portion of the tire tread that sticks out and makes direct contact with the road surface. Non-symmetrical lug shapes and sizes around the circumference of a tire allow it to minimize noise levels at discrete frequencies the tire will experience while in motion. Voids are the spaces between the lugs and allow the lugs to flex.

Sipes are valleys cut across the tire, almost perpendicular to the grooves and usually parallel with the lugs. The sipes provide an additional path for the water displaced by the

grooves, allowing it to escape from the sides of the tire. Siping has been found to increase traction on practically all road surfaces, notably including wet roads, snow roads, and icy roads. As such, this design is usually found on snow or winter tires. The sipes essentially add edges onto the lugs that allow it to flex further and cut into a surface.

It has been claimed that siping was invented in the 1920's by slaughterhouse worker John Sipe. Mr. Sipe's rubber-soled shoes tended to slip on the wet and bloody floor of the slaughterhouse so he decided to try cutting thins slits into the rubber. He soon realized that "siping," or cutting these thin slits into rubber, could also be applied car tires to improve their traction. He patented the process around the 1920's but the idea took around 30 years to catch on.

A thirty-year old study by the US National Safety Council found that siping improved rolling traction on "glare ice" by 28 percent. The main drawback to this technique is that the sipes increase road noise and tire wear when a vehicle with the tires is just ran on a dry surface. Furthermore Consumer Reports does not recommend the practice because of those issues. Some companies such as Les Schwab believe that microsiping extends the life of a tire claiming that it reduces tire friction heat and wear. Winter tires, specifically snow tires, from Michelin and Bridgestone are shipped from the factory with sipes. Smaller sipes can be cut into tires without negatively affecting the performance. The practice of microsiping, or cutting smaller sipes, usually a few millimeters in diameter, has even developed into its own aftermarket.

Experimental observations for traction on ice and show are presented in Figure 3-7.

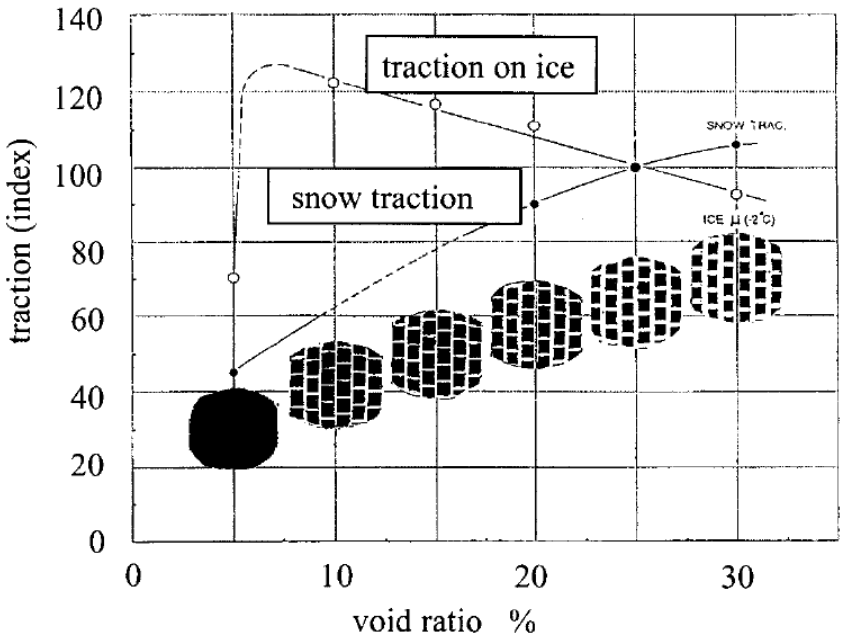

Figure 3-7. Observed traction on ice and snow versus the void ratio [35].

The generic winter tire tread on one of the tires provided by Goodyear has all of these characteristics, seen in Figure 3-8. There are four grooves that run the circumference of the tire. There are lugs around the edges of the tire that have siping that extends from the grooves to the edge of the contact patch. Additionally it has larger sipes that come from the sidewall to the edge of the contact patch. These lugs have about two millimeters of space between them, the voids. The four grooves separate the inner tread into 3 pieces, with a zipper-like pattern of siping and voids.

Figure 3-8. AVDL Goodyear pneumatic tire with generic winter tire tread pattern.

3.5 Chemical Composition of the Tire

The tread is usually a thick rubber or rubber/composite compound that has been formulated to give an application-specific appropriate level of traction and is supposed to give the tire a life of tens of thousands of miles. One chemical used to expand the flexibility of the tire and increase its traction on ice is brominated isobutylene-co-para-methylstyrene (BIMS).

Tires are usually constructed from a combination of vulcanized rubber and styrene-butadiene rubber (SBR). Vulcanized rubber is a created from natural rubber that has been made more durable through the addition of heat and sulphur. Natural rubber by itself is a molecule called polyisoprene and this process creates a cross-linked version of the molecules in the new product. SBR is a synthetic rubber copolymer that maintains its stability well as it ages, and has high abrasion resistance from the additives in the copolymer, giving it ideal properties for a vehicle tire.

3.6 Effective Rolling Radius

The radius of a tire in rotation is not the same as that of tire that is at rest. As the wheels provide power to, or drive, the vehicle the radius of the rotating tire slightly increases. This feature is called the effective rolling radius, R_e. To determine this effective rolling radius requires taking several measurements of the tire at different states. The unloaded circumference is measured around the widest portion of the tire tread first—with the tire suspended—to determine the unloaded radius of the tire, R_u. The loaded radius of the tire, R_1, is taken when the tire is on a flat surface and the contact patch is loaded to a specified mass. The difference between these two measurements, Δ_t, is found by subtracting the loaded radius from the unloaded radius [17]. The unloaded radius and Δ_t are used to estimate the effective radius in equation (3.1).

$$R_e = R_u - \frac{1}{3}\Delta_t \tag{3.1}$$

The estimated effective rolling radius from the calculation was compared to actual observations from the Terramechanics Rig. The power to the Terramechanics Rig was cut off and the calibrated sensor readings were used to get consistent load readings. Utilizing just the weight of the carriage, sensor assembly, bolts, rim, and tire, the effective rolling radius was found by manually moving the carriage and recording the circumference through the use of a reference line on the tire. The observed effective rolling radius for the smooth tire at 35 psi was compared to the calculation above and found to have a percent error of 0.306%. According to the equation, the effective rolling radius will increase as the load on the tire increases. An example of the effective rolling radius calculations that were carried out is given in Table 3-4.

Table 3-4. Table of the calculations for the effective radius of the tire subject to the weight of the carriage.

Carriage Mass (Approximately 700 lbf)			
		INCHES	CM
Unloaded tire circumference (inches)	C_t =	91.75	233.045
Unloaded Radius Calc			
C_t / 2 (pi)	R_u =	14.60246603	37.09026371
R_1 = loaded radius	R_1 =	13.75	34.925
DELTA_t = R_1 - R_u	Delta_t =	-0.852466029	-2.165263713
EFFECTIVE ROLLING RADIUS (R_e)	R_e =	14.88662137	37.81201828

3.7 Tire Friction on Various Surfaces

Tire friction values are usually measured with a locked-wheel towed trailer [41] or some piece of equipment that can hold a piece of tire tread stationary while it is being dragged along the surface. This would provide a coefficient of friction for the kinetic friction value. For the speed that the rig travels at, less than two miles per hour, typical values for dry asphalt are 0.80 to 1.2. On a "traveled" surface this decreases to a range of 0.6 to 0.8 [42]. For a block of rubber on ice, the kinetic coefficient of friction has been recorded as 0.15 [43].

The exact method to determine the rolling resistance coefficient was unknown. Typical car tires on concrete had a rolling resistance of 0.010 to 0.015. A looser surface has a higher rolling resistance, where a typical car tire is reported to have a rolling resistance of approximately 0.3. To contrast this, a railroad has a rolling resistance range of 0.00002 to 0.001. The lower values correspond with less force required to rotate the tire.

4 Characteristics of Ice and Tire Friction on Ice

Ice is one of the least desirable surfaces to encounter in a vehicle. The traction of a vehicle on ice is dependent upon the smoothness of the ice, the temperature of the ice, the temperature of the tires, the speed of the vehicle, the pressure the vehicle exerts on the ice and so on. The physical properties of ice literally shift due to the temperature of the ice and its surroundings. Below -10 °C ice is a very hard and moderate-friction surface. Above -10 °C the ice surface becomes *weaker*, or more malleable than ice below -10 °C [44].

The friction of rubber on ice does not obey Coulomb's Law. In regards to friction, Coulomb's law explains that the normal force exerted on one surface from another surface—regardless of the contact area—determines the amount of friction between the two surfaces [44]. Additionally, the kinetic friction of the surfaces would be independent of the sliding velocity between the two surfaces. Essentially Coulomb's Law is a series of observations that have been credited to Coulomb, Amontons', Da Vinci, Euler, and several other scientists [45]:

1) Force of friction is directly proportional to the normal load
2) Force of friction is independent of the actual contact area
3) Kinetic friction is independent of sliding velocity

Rubber and its derivatives do not follow Coulombs' Law exactly. In fact no deformable elastic substances do. The best example is a car tire, as the mass of the vehicle, or the normal load exerted on the tire, causes the contact patch to deform. Depending on the type of tire, it can either flatten out (radial ply) or slightly rise up in the middle of the contact patch (bias ply), also determined by the inflation pressure and the amount of plies. On an ice surface, this means that

the tire should actually have an increased amount of friction as it is stretched out—assumedly because there is an increase in the asperities between the two surfaces.

In fact the amount of friction of a rubber pneumatic tire on ice appears to be more dependent on the temperature of the rubber and the ice, and is affected by a far lower degree from the pressure in the contact area or the normal force exerted on the ice [46]. Above -10 °C the surface of ice has been described as weak; and in comparisons against rubber it has been observed that the malleable surface of ice is the chief component of friction and not the viscoelastic properties of the rubber [46]. This "friction behavior" of the tire is directly related to its mechanical performance [47].

4.1 Water Layer Formation

Ice is defined by the Miriam-Webster's dictionary as frozen water [48]. The freezing point of water is commonly known as a temperature of 32°F (0°C), with a density of 1000 kg/m^3. At this temperature (and a pressure of one atmosphere or 101 kPa) the ice and water are actually in equilibrium, also known as the ice point [49]. This promotes the formation of a layer of water between ice and any surface that comes in contact with it.

This thin film of water has been observed in numerous experiments and there is "strong evidence" of a water layer forming on ice causing the low coefficient of friction [of most materials] observed on ice. The authors of "The Mechanism of Sliding on Ice and Snow" believed that the friction between two pieces of was caused by the viscous shear (resistance from the fluid from parallel motion of two bodies) in the water layer between the two pieces [50]. This viscous shear would be reduced with one less fluid surface, but the effect would potentially still be present.

4.2 Differences in the Formation of Ice

The formation of ice is affected by a number of parameters. The temperature of the ambient air in a room can affect how quickly the ice can form and change the texture of the surface while the ice is forming, and while the ice is sitting in the test area [51]. Air bubbles can lower the density and strength of the ice. The rate of freezing affects the formation of crystals and air bubbles inside the ice [1]. If the ice is being frozen by way of a moving platform or rotating drum [that would hold the ice] it can be affected by the rate of the water flow [52].

4.3 Main Factors that Affect Tire Friction on Ice

Differences in the coefficient of friction between a pneumatic tire and an ice surface can be caused by a number of factors. These include the chemical composition of the tire, the chemical composition of the ice surface, surface roughness, the mechanical properties of the ice and the tire, the temperature, the humidity, normal load, inflation pressure, slip ratio, sliding velocity, and so on.

In this experiment we maintained a number of variables while modifying variables that the Terramechanics Rig allows adjustments for. Only two tires were provided for this series of experiments so the chemical properties of the tires are assumed identical. The mechanical properties are as closely related as possible with the exception of the additional dynamics present with the tread elements.

The temperature and humidity were very difficult to control but by testing during the morning, evening, and cooler days, the humidity and temperature factor was limited. The humidity ranged between 60% and 70%. The temperature during the tests was 72 or 73 °F (22.2

or 22.8 °C). This was of course higher than the cooling system was designed for, but it could maintain a film-free surface at these ranges.

Surface asperities can increase the friction between the tire and ice. The test surface in the Terramechanics Rig was reconditioned after each set of test runs. The Rig allowed three tire passes before it had to be resurfaced. Resurfacing was conducted by scraping the ice surface smooth with a steel-blade floor scraper and using a resurfacing cloth from Custom Ice Inc. The resurfacing cloth was soaked with warm tap water at a temperature of 108 °F (42.2 °C) and dragged across the test area on the ice. This required 30 minutes to an hour to completely refreeze, after which tests could be run on the surface again.

The inflation pressure and normal load were controlled at the carriage of the Terramechanics Rig. The inflation pressure and normal load change the size and shape of the contact patch. The inflation pressure could be adjusted manually with an inflation gun. The normal load was controlled by an air tank connected to the air springs.

The carriage speed was maintained at a consistent 7.4 cm/s while the slip ratio was adjusted at the tire through the PiCPro controller program. The slip ratio greatly affects the coefficient of friction of a pneumatic tire on ice, or any surface for that matter.

5 Test Equipment

This chapter gives an overview of the test equipment utilized in the tests carried out in this study. The first section discusses the equipment on and the capabilities of the Terramechanics Rig in the Advanced Vehicle Dynamics Lab (AVDL). The second section covers the data acquisition system. The third section covers the Tekscan Pressure pad used to verify the normal load and record the size and shape of the contact patch. The fourth section explains the ice making equipment.

5.1 Test Equipment: Terramechanics Rig

The AVDL Terramechanics Rig consists of the following main components: the test chamber, the support structure, actuation, and controls [53]. The rig's chamber was designed to enable a variety of testing scenarios. The interior of the rig is 25 feet long and 6 feet wide (71 inches) and is capable of holding soil, sand, ice and practically any surface that can stay confined within the steel container. On the sides of the container are L-brackets that run the length of the rig longitudinally. These allow for the 25 one-foot wide steel C-channels to be placed at two heights, enabling two different test heights. These C-channels, illustrated here in Figure 5-1, are 2 inches in height and weight 80 lbs each.

Figure 5-1. Steel C-channel (1 of 25) that formed the test bed.

Prior to this study, other tests have been conducted in the Terramechanics Rig using the lunar soil simulant GRC 1 for metal wheels. The experiments covered in this thesis utilized the test bed for the creation of ice, and tested pneumatic tires on this surface. These tests were conducted on the upper height that provides 10 inches of test height. The thermal exchange between the ice and its surroundings was lowered by placing two layers of one-inch R5 foam insulation directly between the ice and the test surface, as seen in Figure 5-2. The foam was covered with two sets of 6 mil plastic sheeting in order to ensure that the ice surface support was watertight for the creation of ice. This reduced the available test height to eight inches.

Figure 5-2. The foam insulation that sits above the steel C-channels.

The motor that provides torque to the wheel, the gear box, and the sensor hub are found on the wheel carriage assembly. In addition, this structure holds the linkage systems that can be employed to control the camber and the toe angle. This structure can be moved up and down (along the z-axis in the sensor's reference frame) on linear rails attached to the figure-4 shaped structure that holds the wheel assembly structure in place. This number "4" shaped assembly also has linear bearings on the bottom of the structure that run perpendicular to the length of the rig. These linear bearings allow it to move laterally on a pair of parallel linear rails that sit on the bottom structure of the carriage, as seen in Figure 5-3.

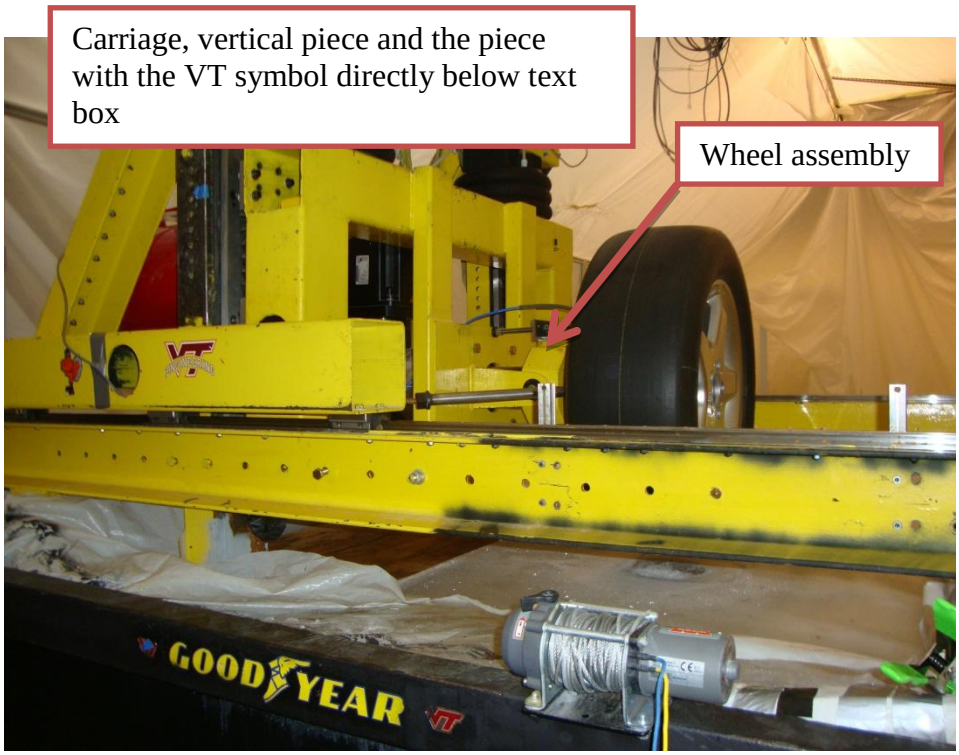

Figure 5-3. Image of the carriage of the Terramechanics Rig.

The actuation of the rig is provided by two motors. The longitudinal motion of the wheel carriage is provided by a motor located at the far end of the rig (i.e., where the carriage is pictured in Figure 5-2). The rotation of the wheel is provided by a motor located on the wheel assembly structure, which can be identified in Figure 5-3.

5.1.1 Test Equipment: Terramechanics Rig: Enclosure Modifications

The aluminum and Plexiglas enclosure around the Terramechanics rig was not sufficient to regulate the temperature inside the area. A large 6 mil plastic sheet was utilized to try and decrease the heat transfer between the enclosure area and the surroundings, seen in Figure 5-4. It

was able to consistently lower the temperature about 5 F (2.22 °C) compared to the outside of the enclosure or the rest of the lab.

Figure 5-4. The plastic sheeting surrounding the enclosure.

5.1.2 Test Equipment: Terramechanics Rig: Air Springs and Modifications

The Terramechanics Rig was constructed to handle a plethora of loading and offloading scenarios, such as the normal load applied to the wheel can be set from zero to 18 kN. Previous research conducted on the rig created offloading conditions by utilizing long cylindrical air springs attached to the vertical carriage in order to essentially pull up the carriage by way of the horizontal I-beam. This I-beam is visible in Figure 5-5, which also shows the holes drilled into the beam that would allow the carriage to be locked in place laterally.

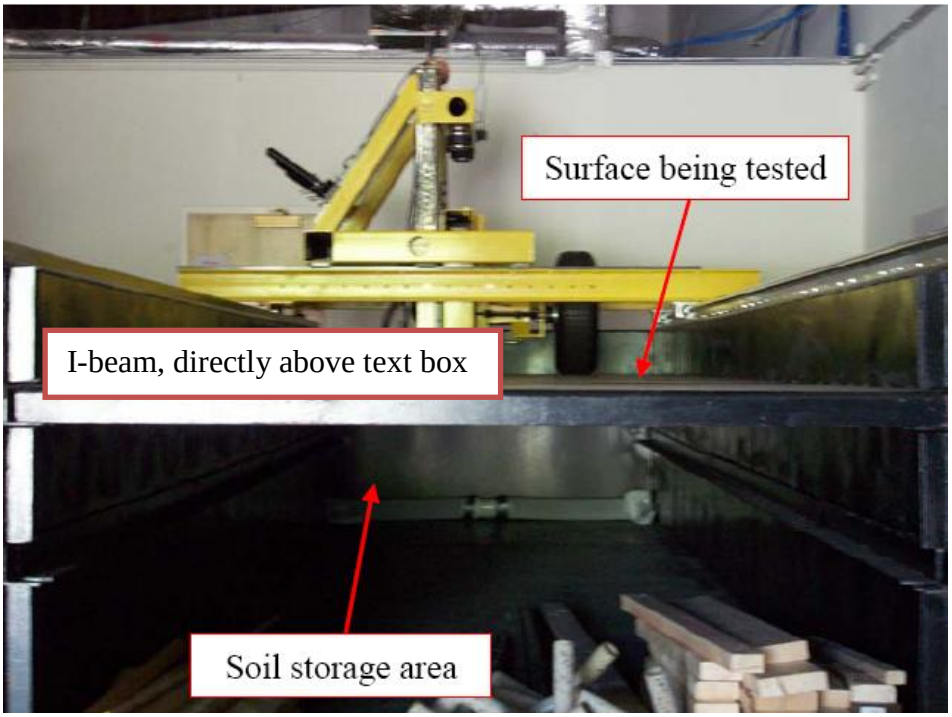

Figure 5-5. Image of the empty Terramechanics Rig.

Alternatively, offloading can be obtained using a steel construct that could hold Olympic weight plates (weightlifting plates) mounted on the slanted face of the 4-shaped member, also seen in Figure 5-5. For loading scenarios, a steel-square crossbar was used above the motor carriage to push down on it.

A previous version for loading the wheel utilized the crossbar attached to the 4-shaped member in order to push down on the carriage with two air springs, on the far ends of the crossbar. The previous set of air springs was a pair of Goodyear "Super-Cushion Air Springs," model # 1B5-510. These springs were rebranded springs created by ITT Enidine Inc., rated to provide up to 2,446.4 N (550 lbf) at a maximum pressure of 689.48 kPa (100 psi). These springs

had a stroke, or displacement capability, of 76.2 mm (3 inches), from a minimum height of 45.72 mm to 12.192 mm (1.8 inches to 4.8 inches) of maximum operating height [54].

During initial tests using these springs it was noted that they would not be able to provide enough force—along with the weight of the carriage pushing down on the tire—for the low-weight test scenario of approximately 6672 N (1500 lbf) to be exerted on the tire, let alone the higher scenario of about 8896 N (2000 lbf) required. Furthermore, the crossbar shifted from a completely horizontal position, verified at 0 degrees through the use of a digital level, to above positive 15 degrees as measured from the horizontal axis (the x axis of the measurement system), as the force of the air springs pushed on the crossbar and the vertical motor carriage, moving the crossbar in the process. The original setup of this crossbar utilized two grade 8 bolts on both sides; approximately one and one-quarter of an inch from each other. Both bolts were secured through washers and locknuts in slotted holes. This configuration was meant to allow the crossbar to be moved inward and outward as required, but created a situation in which the crossbar would not maintain its position when subjected to a large amount of force.

To obtain the testing conditions required for the present study, air springs that could generate more force were needed. A pair of large triple convolute bellow air springs, Goodyear 3B12-305's, able to generate the forces required, (being rated for a capacity of up to 12.9 kN (2900 lbf) each and a maximum operating pressure of 689.48 N (100 psi) were used. These air springs were 33.02 cm (13 inches) in diameter, compared to the previous ones that were only 15.24 cm (6 inches), and had a stroke of 33.528 cm (13.2 inches) to 7.62 cm (3 inches). Their minimum height was 12.192 cm (4.8 inches) compared to 4.572 cm (1.8 inches) for the smaller air springs [55]. These springs were rated to a minimum operating temperature of -29ºC (-20ºF)) [55]. Testing the new air springs with the original carriage setup quickly showed that the

crossbar needed to be reinforced and the air springs moved closer to the center of both the crossbar and the vertical carriage.

After consulting with Michael Craft, senior research associate at CVeSS, the setup was modified on-the-fly. The bolts were moved further apart and a set of metal bars were installed in a triangular configuration in order to hold the crossbar securely in place with grade 8 bolts, as seen in Figure 5-6. These metal bars were created from an extraneous piece of steel in the lab. Each bar was 1.27 cm (0.5 inch) thick, 7.62 cm (3 inches) wide, and approximately 27.3 cm (10.75 inch) long.

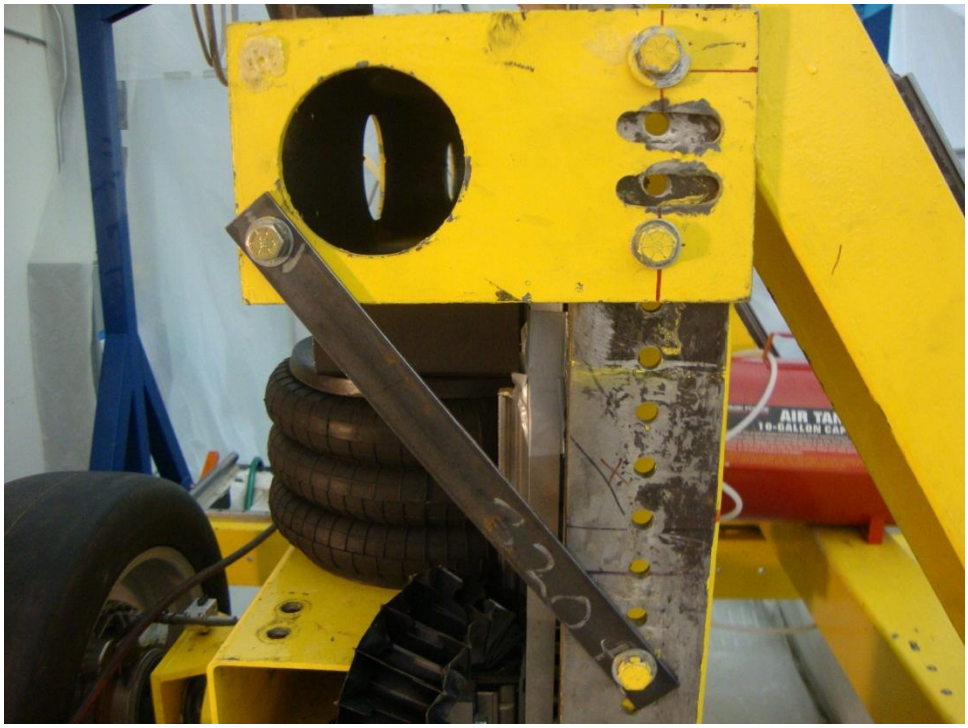

Figure 5-6. Side view of the reinforced crossbar.

Furthermore, the location of the air inlet and the size of the air springs necessitated additional hardware. A pair of 3 inch (7.62 cm) wide steel squares were mounted at the top of

the air springs in order to mount the air springs centrally on the crossbar instead of having to offset them because of the air inlets. This also provided enough space for the usage of two 3/4 inch (1.905 cm) male to 1/2 inch (1.27 cm) female adapters for the inlets. The squares and the adapters can be seen in Figure 5-7.

Figure 5-7. Close-up of the steel squares used to center the air springs on the crossbar above.

The female end of these adapters were mated to the ½ inch (1.27 cm) threaded end of the quick connects. These quick connects were used in conjunction with the 3/8 inch (0.9525 cm) air hoses that filled each air spring from a 10-gallon air tank, as seen in Figure 5-8.

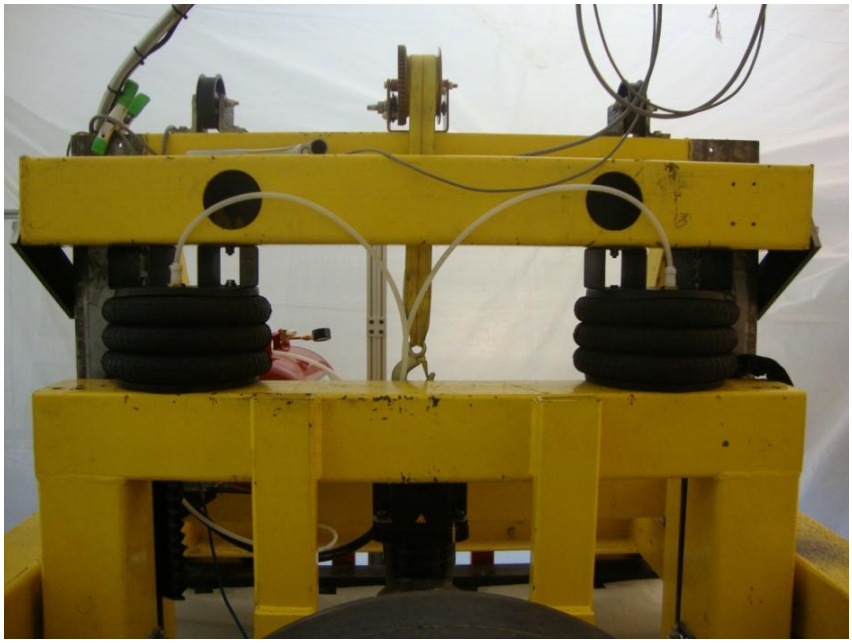

Figure 5-8. Air springs, air hoses, and red 10-gallon air tank (in the back of the image behind the left spring).

Initial tests of this configuration confirmed that it was more than adequate to handle the forces required for this study. The reinforced crossbar was very stable and stayed locked firmly in place during movement tests. Interestingly enough, the 10 cm (4 inches) of ice supported by the steel C-channels cracked in several locations under the weight generated in the contact patch of the smooth tire. These cracks ran from around the contact patch and spread for a foot up to about two feet out laterally. The air springs required close to 137.9 kPa (20 psi) to generate 8673.8 N (1950 lbf) in the contact patch, in addition to the 222.4 N (50 lbf) of the smooth pneumatic tire. This was at a stroke height of 22.86 cm (9 inches).

The graph illustrating the load versus deflection curves provided by Goodyear for xxxx is presented in Figure 5-9.

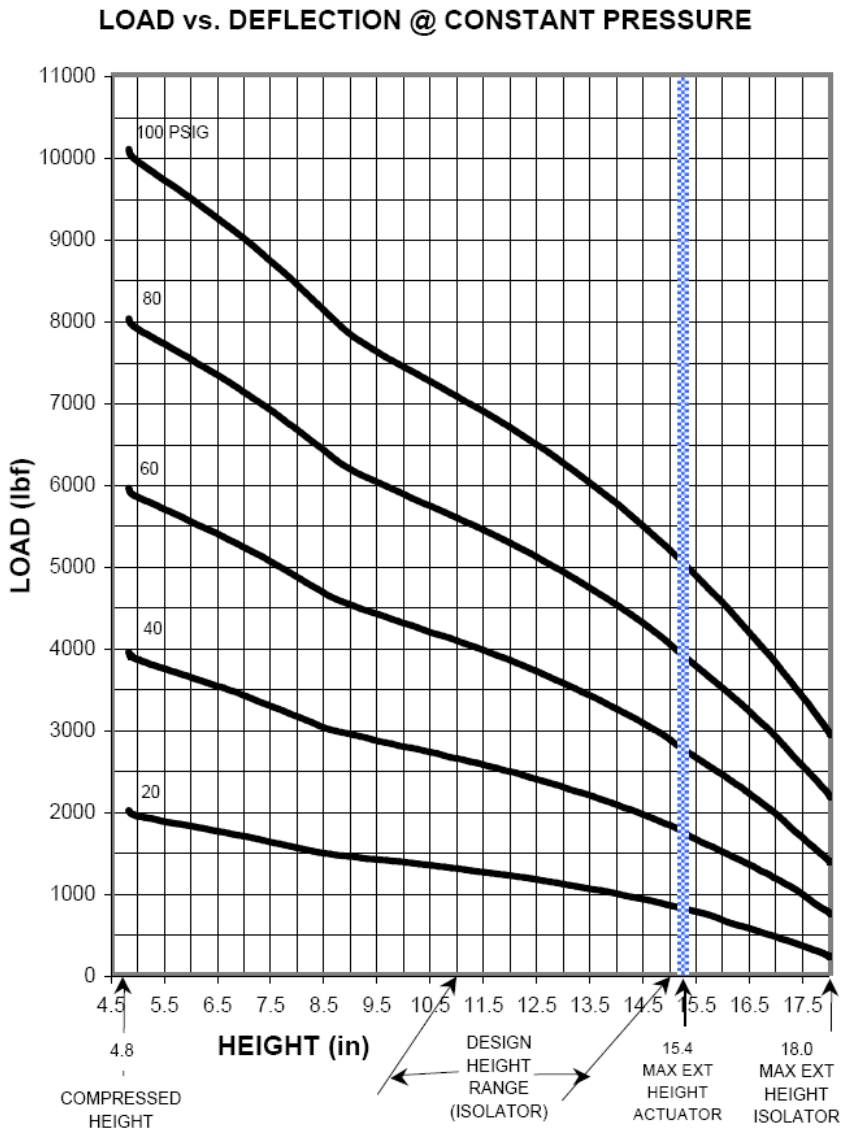

Figure 5-9. Goodyear graph of load versus height per psi rating [56].

5.2 Test Equipment: Kistler RoaDyn P650 Wheel Force Sensor

The Terramechanics Rig utilized a RoaDyn P650 Wheel Force Sensor (WFS) from Kistler, where the portion of the sensor or dynamometer illustrated in Figure 5-10. This sensor uses piezoelectric load cells to measure the forces and moments of a wheel or tire. Piezoelectric

technology relies on crystalline materials that can generate an electric charge when they are deformed. Kistler uses load cells made with quartz crystal material.

Figure 5-10. The dynamometer that contains the four load cell pairs [57].

Kistler has different models ranging from three load cells to six load cell pairs. The P650 model utilizes four load cells. With the increased number of load cells comes increased accuracy of the measurements. The four load cell pairs of the P650 sensor are placed in a square formation centered in the dynamometer. The "charge signals" of each opposing load cell pair are amplified by charge amplifiers, so that cells do not dissipate this charge [58]. The load cells measure the signals in an analog manner and these signals are filtered and digitized simultaneously by the dynamometer. These signals are arranged with a micro controller at the dynamometer that also PCM-codes the signals, thus creating a digital representation of the analog signals.

To collect this information from the dynamometer, the system utilizes a type of antenna called a stator. The stator allows the data to be wirelessly transmitted through by pairing it with

a transmission ring serially connected to the dynamometer, shown in Figure 5-11. The stator and transmission ring are also responsible for providing power to the hub sensor through inductively coupled coils in both units.

Figure 5-11. The transmission ring [57].

The sensor is read and controlled by the RoaDyn Remote Emulator program—which is used instead of a hardware remote control unit. This allows a piece of hardware with a serial connector, in this case the Terramechanics Rig laptop, to mimic the functions of a RoaDyn Remote. This remote works through the On-Board Electronics.

The System 2000 On-Board Electronics is a control box that uses a set of electronic circuit boards including digital signal processors. There is one series of cards for each sensor hub. One DSP is responsible for data handling, the offset, the angle adjustment, and lever arm adjustment. The other DSP handles output data management and controls the touch screen of a remote control unit or the Remote Emulator controller, seen in Figure 5-12.

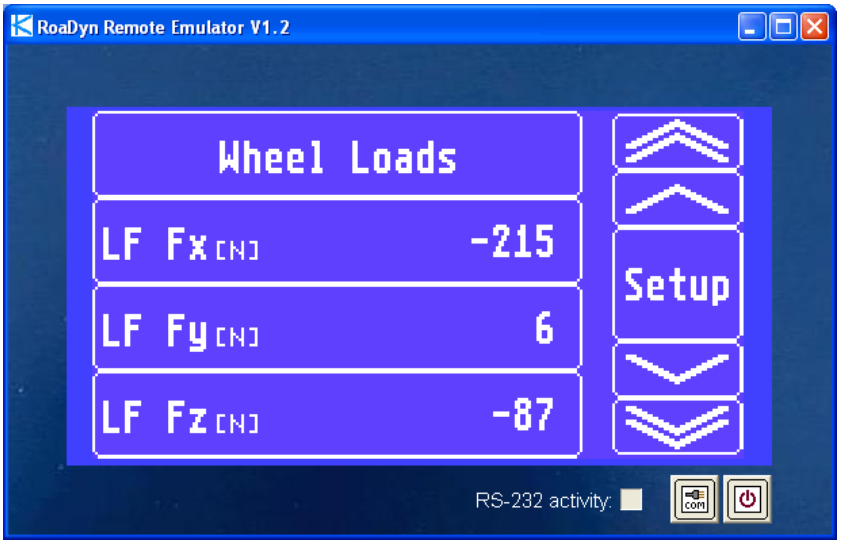

Figure 5-12. Image of the Remote Emulator controller (screenshot).

5.3 Test Equipment: Terramechanics Rig Computers

The main computer containes the software to actuate the carriage and the hub motor, PiCPro MMC Limited Edition, the data acquisition software LMS Test.Lab 8b, and the camera software "Logitech Webcam Software." This computer is a Dell Vostro 200 tower with an Intel Core 2 Duo 4300 processor rated at 1.8 GHz. The computer has 250 GB SATA hard drive and 2 GB of DDRAM. It was upgraded to allow the use of two monitors at a time. Despite the overall speed of the computer the speed of the software was limited by the connection to the data acquisition hardware and the speed of communications between the actuation hardware and the software.

5.4 Test Equipment: Motion Control Software and Hardware

The PiCPro MMC Limited Edition software is a ladder-based programming language that actuates the position of the rig in the longitudinal direction and the rotational velocity of the hub

motor using “ladder units” and also provides the position and the speed of both on the Terramechanics Rig in ladder units and ladder units per minute, respectively. The core structure of the programming was created by G&L Motion Control. The actual angular and longitudinal speeds are programmed manually at AVDL and calculated based on the need of each specific test. The effective rolling radius of the tire is needed to program the desired slip ratio between the tire and the testing surface. The rolling radius and the desired tangential speed help to determine the appropriate angular velocity.

The PiCPro controller communicates via an SCSI connection and utilizes a USB adaptor to connect to the Terramechanics Rig computer. The adapter is an Ultra-160 SCSI interface capable of handling up to 160 megabytes/s of data. The program itself however is limited to a communication speed of 115.2 kilobytes, identified as 115,200 baud in the program, and far slower than the hardware.

5.5 Test Equipment: Data Acquisition

LMS Test.Lab is the data acquisition software package. It records the data from the Kistler sensor hub and the string potentiometer mounted on the wheel carriage, utilized when the displacement of the center of the hub in the vertical direction needs to be recorded. Currently there is no way of acquiring the speed of the longitudinal access or its location in the data acquisition software, although the PiCPro software does give real-time information on the speed and position based on feedback from the controller hardware. The Test.Lab software records the forces on each axis (F_x, F_y, F_z), the moments about each axis (R_x, R_y, R_z), and the height of the string potentiometer. Additionally, the angular position and the angular velocity of the hub are also recorded. The software can be set to record data for any duration of time and in any

increment of a second. The bandwidth frequency (half the sampling frequency) and the frequency rate can be set to change rate of data acquisition.

After the data is collected, it can be graphed in a variety of methods through LMS Test.Lab; most useful for the purposes of this experiment are the Front-Back plots. An example of a data comparison can be seen in Figure 5-13. All data collected can be exported to a variety of file formats; most useful is a .txt or text file format that can be exported to Matlab. Another useful method was exporting the data as .csv or comma-separated variable that allows the data to be used in a spreadsheet program such as Microsoft Excel.

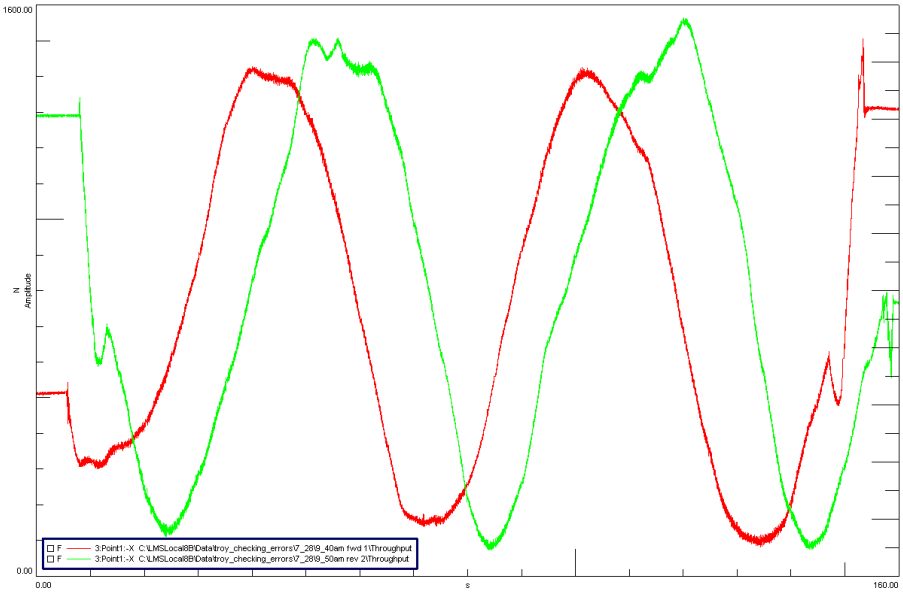

Figure 5-13. Example of the graphing ability of LMS Test.Lab.

The observed readings are collected through an LMS data acquisition system called LMS SCADAS. The LMS SCADAS hardware is a front-end specifically designed for data acquisition in the engineering field. SCADAS is the acronym for supervisory control and data acquisition (SCADA) system. SCADA systems can be used to control and monitor a variety of equipment.

For the purposes of the Terramechanics Rig at AVDL, the system merely has to monitor the data being sent from the analog Kistler system and to convert it into a digital signal for storage on the computer [59].

The system has four PQA-II cards (programmable quad amplifier) that can accept an AC, DC, or ICP input. There are 16 voltage and ICP (intelligent communication processor) channels in the four cards. The system utilizes a BNC connector, or a coaxial cable connector that has a twist-on bayonet mount connector for each channel. The three forces and three moments, angular velocity and anglular position are recorded using eight of these channels. The string potentiometer is connected to the ninth channel. The system also has an unused Programmable Dual Tacho Module (PDT), with two channels, that could be used for measuring the rotational speed of a shaft or disk [59].

5.6 Test Equipment: Pressure Pad

AVDL's pressure pad hardware is a Tekscan I-Scan Pressure Measurement System comprised of the Magna PCI Expansion System, data handle, and several pads including a pair of MatScan® 3150 pressure pads, as seen in Figure 5-14. The system can create 2D or 3D images and video of the contact profile or contact patch of an object.

The Magna PCI Expansion System is designed to hold Tekscan's PCI board (PC Interface Board SR-2). This board allows the system to communicate with the computer and interpret the Tekscan hardware. The Magna device is connected to the Terramechanics Rig laptop via a PC Card connector (PCMCIA). The data handle allows the system to use multiple types of pressure pads, and is connected to the Magna PCI Expansion System through a

proprietary 6-pin mini-DIN serial connector. The handle interfaces with the pressure pads using a slot that physically connects matching contact points on the pressure pad's sensor tab.

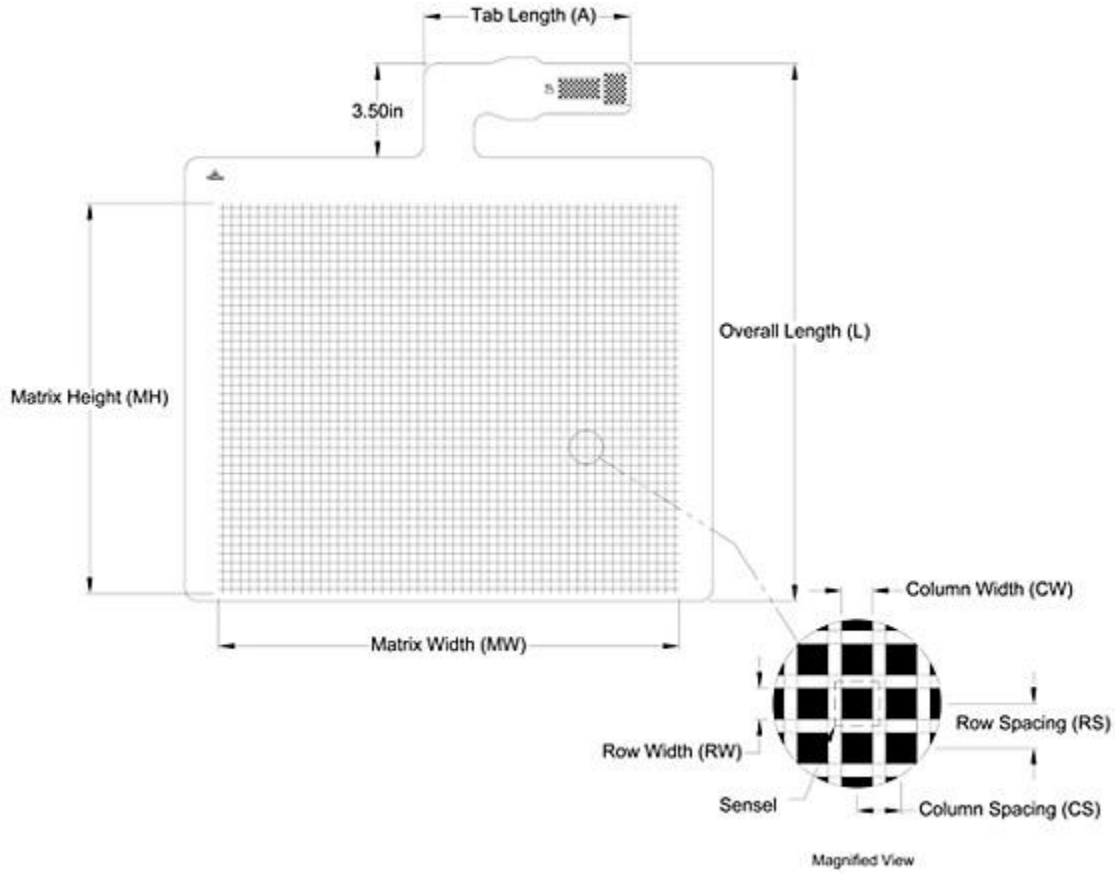

Figure 5-14. MatScan® pressure pad [60].

The pressure pads used are MatScan® 3150 low-profile floor mat pads, diagram illustrated in Figure 5-14, designed for measurements such as a bare human foot. One 50.8 cm by 49.911 cm (20 inches by 19.65 inches) pressure pad has a sensor area of 36.88 cm by 43.59 cm (14.52 inches by 17.16 inches). Within this sensor area are 44 rows and 52 columns for a combination of 2288 sensels, with a sensel density of 9.2 sensels per square inch (1.4 sensels per square centimeter) 59.35 sensels per cm square) and a resolution of 330 mils (0.330 inches) [61].

A sensel is a square section of the sensor comprised of two horizontal and two vertical strips of sensors [60]. The MatScan® sensor has a sensor tab on one side that is inserted into a "handle."

The Tekscan system reads the pressure data in the form of raw sum readings. The sensor has to be calibrated in order to get the force values from these raw sum readings. For this purpose the Tekscan equilibrator was utilized to give an exact and even pressure to the sensor. This reading was then double-checked and modified as necessary to give a reading that was as accurate as possible. The process of equilibrating—flattening out or equalizing the initial readings of the system—and calibrating the pressure pads is described in the Tekscan manual.

5.7 Test Equipment: Ice-Making Equipment

The ice surface in this experiment was created on top of the C-channels of the Terramechanics Rig. The ice-making equipment was previously purchased from the company Custom Ice, Inc. The ice-making equipment comprises of three main components: the MiniMate ice rink refrigeration unit, the Roll-Out-Rink piping system, and the hoses that connect the refrigeration system and the piping.

The MiniMate ice rink refrigeration unit is permanently installed outside the Center for Vehicle Systems and Safety (CVeSS) lab, seen in Figure 5-15. A diagram of the system can be seen in Figure 5-15. The unit utilizes the refrigerant R404a, or a blend of hydroflourocarbon and other refrigerants, in order to cool down the ethylene glycol found in the supply and return connection hoses. The unit works in units of Fahrenheit and can be set from 0 F (-17.78 °C) to over 100 F (37.78 °C). Custom Ice, Inc. describes the system being capable of providing three tons of refrigeration at design conditions of 18 F (-7.8 °C) LWT (leaving water temperature, or the temperature of the water chilled by the system). The system was designed to work in

weather conditions up to 45-50 F (7.22-10 °C) and is rated to provide up to 12 months of operation with a full tank of refrigerant. The ice-making conditions at AVDL during the months of June and July 2010 varied between 70 to 90+ F (21.1–32.2+ °C).

Figure 5-15. The MiniMate Chiller refrigeration unit

Custom Ice, Inc. provided the "Roll-Out-Rink" "portable ice floor piping system" that was custom-made to fit the six foot (71") by twenty-five foot space of the interior of the Terramechanics Rig, as the pipes actually come in sets of "piping rolls" that are 4 feet (1.22 m) wide and 25 feet (7.62 m) long. The pipes themselves are half-inch (1.27 cm) plastic pipes spaced 1.5 inch (3.81 cm) apart from each other, and held in place with integral spacer strips. These spacers maintain the separation between the pipes and flatten out the surface—otherwise the piping would just roll up and twist upon itself. These plastic pipes were joined to three

copper pipes, each one inch (2.54 cm) thick. The far end of rolls had one copper pipe, while the other end had two 1-inch (2.54 cm) bars—one for the supply connection and one for the return connection. The pipes on that end had copper headers for the supply and return connection hoses.

The supply and return connection hoses were approximately 20 feet (6.1 m) long and connected the MiniMate unit to the piping system, seen in Figure 5-16. These were 1.5 in (3.81 cm) diameter flexible PVC hoses. (PVC is the abbreviation for polyvinyl chloride, a thermoplastic resin created from the polymerization of vinyl chloride [62].) Each hose was a single-feed device that circulated ethylene glycol from the glycol pump inside the MiniMate unit to piping system. The source of ethylene glycol was the glycol tank that was mounted inside the lab.

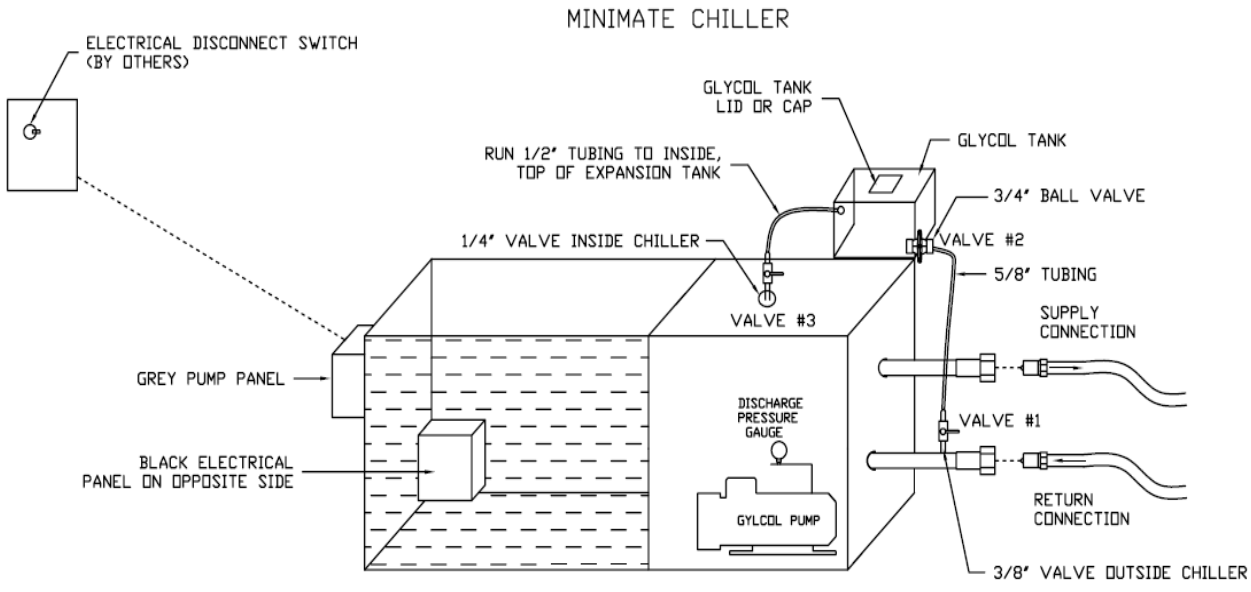

Figure 5-16. The MiniMate Chiller refrigeration unit diagram.

5.7.1 Test Equipment: Ice-Making Equipment: Creation of Ice Test Surface

The Terramechanics Rig is designed to handle multiple surfaces on its test bed. For the creation of ice in the rig, the previous test surface—a form of sand called lunar soil simulant, GRC 1—had to be removed from the container. After removing the sand, the rig had to be outfitted to contain the ice and the subsequent condensation. The ice itself was created using the MiniMate ice rink refrigeration unit, the Roll-Out-Rink piping system, and the hoses that connect the refrigeration system and the piping. The MiniMate unit had to be turned on for 24 hours before actually making ice, in order to warm-up the crankcase heaters.

While this occurred, the twenty-five C-channels that comprise the structure of the test surface were moved from the lower L-channels to the upper L-channels. A 6 mil plastic sheet was placed under the steel C-channels in order to collect any condensation that could form underneath, affixed to the interior sides of the rig and the lower L-channels. A six foot (10.8 m) long 2-by-4 beam (5.08 cm by 10.16 cm) was placed at the opening end of the rig in order to stop any water that might form on the bottom of the rig from escaping the container. This was affixed at the bottom by silicon sealant.

The top of the C-channels were covered with 2 inches (5.08 cm) of pink foam insulation. This foam insulation was sealed using duct tape. Above this, two sheets of 6 mil thick plastic sheeting were used to ensure that the rig was watertight. These sheets were affixed to the sides of the container with gorilla tape, a stronger and stickier form of duct tape. Any suspected holes or tears were covered with tape on both sides of the plastic sheets. The Roll-Out-Rink system was placed onto this prepared surface. Due to the bending of the hoses, only one side of the system could be perfectly aligned to the side of the rig. The Terramechanics Rig and hub allow

for testing from the middle of the surface to the right side of the container (facing the rig from the computer station), or the side furthest from the side bay door.

Ice was created by using the inside garden hose faucet and a 50-foot (127 m) garden hose. The temperature of the water averaged 70 F (21.1 °C). The plastic pipes were first flooded to approximately the top of the hoses, and allowed to freeze completely. From this point on, ice was created by spraying water on top of the solid ice at a thickness of 1/8 inch (3.175 mm) to ¼ inch (6.35 mm) per layer, verified using a clear plastic ruler. This continued until the test height of 4 inches (10 cm) was reached, as per equation (5.1) from a Cold Regions Research and Engineering Laboratory (CRREL) found in an internal report by Jeffrey Biggans.

$$h = 4\sqrt{p} \tag{5.1}$$

The calculated thickness of ice versus allowable load, for free-floating ice using the CRREL equation is illustrated in

Table 5-1.

Table 5-1. Calculated thickness of ice versus allowable load, for free-floating ice using the CRREL equation.

Allowable Load (Pounds)	Allowable Load (Short Tons)	Theoretical Ice Height (in.)	Theoretical Ice Height (Fraction in.)
200	0.1	1.26	1 1/4
400	0.2	1.79	1 4/5
600	0.3	2.19	2 1/5
800	0.4	2.53	2 1/2
1000	0.5	2.83	2 5/6
1200	0.6	3.10	3
1400	0.7	3.35	3 1/3
1600	0.8	3.58	3 4/7
1800	0.9	3.79	3 4/5
2000	1	4.00	4

6 Design of Experiment

This chapter details the design of experiment for the single-wheel tests utilizing the Terramechanics Rig in the Advanced Vehicle Dynamics Lab (AVDL) at the Center for Vehicle Systems and Safety (CVeSS) at Virginia Tech. The design of experiment went through several iterations until settling on one design that would provide the results that could be used to compare the data to previous studies. These tests involved combinations of four different sets of factors: a matching pair of tires—one smooth or bare tire without any tread and the other a tire with a generic winter tire tread pattern; two different levels of normal load applied to the axle of the wheel, one at 75% of the nominal load of the set of tires and the other at 100% of the nominal load of the set; two sets of tire inflation pressures, one at the 100% of the recommended tire pressure at maximum load (35 psi, 241.32 kPa) and the other at approximately 75% (26 psi, 101.26 kPa) of the recommended tire pressure at maximum load; and three different levels of slip ratio, the first at a slip ratio value of 0, the second at slip ratio value of 10, and the third at slip ratio value of 20. An initial set of tests were run to determine which factors were not relevant to tire friction on ice, in order to eliminate irrelevant tests. After this run, a second set of tests were carried out in order to see which factors significantly influenced tire friction on ice and if there were any interactions between factors up to a level of third order interactions.

6.1 Design of Experiment: Main Experiment

The number of test runs and number of parameters had to be pared down from previous design of experiment versions due to the large number of runs needed. It was determined through the literature review and pre-testing that the best way to collect data was to create a series of tests that would vary the tire setup, tire inflation pressure, normal load, and the slip ratio

at a bulk ice temperature of 23 degrees Fahrenheit. This temperature coincided with previous studies that tested at -5°C (23°F) and other temperatures around that value, in addition to being physically practical during the summer testing period [1].

The temperature choice was based on the literature review and testing out the system during the summer. Temperatures within a few degrees of the freezing points were very difficult to maintain in 90+ °F weather. A temperature of 23 °F was found to be a good a mix between setting the temperature of the system too high to form ice, and setting it so low that it would not correspond to previous studies and would strain the refrigeration system. It was found that the ice surface maintained a thin film of water at temperature above 77 °F (25 °C) or "room temperature." This required all testing to be conducted in the morning or evening during warmer days, or whenever the inside of the lab was around this temperature on cooler days, to stay as close as possible to the dry friction conditions used for the theoretical analysis in this study.

Ideally, these measurements would be adjusted in the order stated. The tire would have to be present on the Kistler hub, first, in order to allow for the adjustment of the other parameters. Additionally, the tire setup would be the most physically demanding and time consuming task in the series. The inflation pressure would be adjusted while the tire was mounted to the hub. The normal load would then be adjusted after the hub has been calibrated, in order to verify the setting. The slip ratio adjustment would be carried out through the software on the Terramechanics Rig computer. These adjustments would be randomized using the statistical analysis software JMP 8.

The tire setup parameter had two levels. The Advanced Vehicle Dynamics Lab (AVDL) received two pneumatic tires from The Goodyear Tire & Rubber Company (Goodyear). Each tire had the designation "P255/55R18 104 H." One tire was a bald tread tire (or smooth tread

tire) that did not have any tread pattern. The other tire had a "generic winter tread pattern" with a number of lugs, grooves, and other design patterns. Both tires had the same dimensions with a section width of 255 mm (10 inches). The tires can be seen in Figure 6-1.

Figure 6-1. The two tires provided by Goodyear, with two different tread patterns: one bald tire and one tire with a generic winter tread pattern.

Two levels of inflation pressure were specified for testing. The tires from Goodyear were rated for a maximum load of 1984 lbf (8824.32 N) at 35 psi (241.32 kPa) of inflation pressure [63]. It was suggested by technical contacts at Goodyear that we should test the tires at this maximum load and at 75% of the this load, or 1488 lbf (6618.95 N). These loads would be double-checked utilizing the Tekscan pressure pad system. The same idea was used for the inflation pressure, testing it at the recommended inflation pressure of 35 psi (241.32 kPa) and at the lower level, 75% of that value, at 26 psi (179.26 kPa) to observe the effects of this under-inflation on the coefficient of friction at the tire-ice interface.

Based on the literature review, three levels of slip ratio were selected. Most publications on the friction of tires on ice begin at zero slip. The maximum recorded slip usually stops around a slip ratio of 18-20. One example of this can be seen in Figure 6-2.

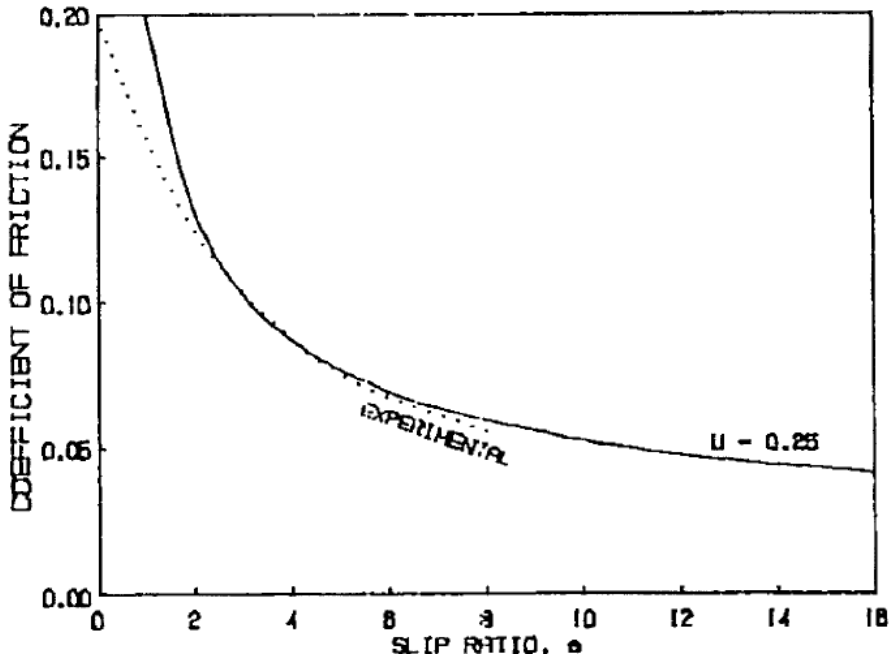

Figure 6-2. Graph of "driving traction" in a previous tire friction on ice study where they observed the coefficient of friction versus the slip ratio [8].

As mentioned earlier, the slip ratios selected were 0, 10 and 20, meaning that the tangential speed of the tire would be faster than the rig above the value zero. The tests would be carried out at a "vehicle speed" of 0.25 m/s if possible, which correlates to the speed of the entire wheel carriage longitudinally along the Terramechanics Rig. The wheel speed was varied using the motor assembly. Through the software, we could control the angular speed of this motor, so the actual amount of slip would be accomplished by first calculating the effective rolling radius of the tire, and then using it to provide the needed tangential tire speed. Using the constant speed of the rig, and varying the hub speed, these values for the slip ratio were carried out using the

PiCPro motor control program. The exact values of slip ratio were computed from equation (1.7). The largest speed value of the motor that moves the carriage longitudinally can provide is approximately 1.62 m/s (3.62 mph) with the provided tires. Thus, a carriage speed of 7.4 cm/s could be used to set the slip ratio while allowing the full range of slip ratios to be tested. Several values of calculated slip ratios are given in Table 6-1.

Table 6-1. Table of the slip ratio calculation, values utilized are highlighted in green.

Tire Speed (cm/s)	Vehicle Speed (cm/s)	CALCULATED SLIP RATIO
0	7.4	-1
7.4	7.4	0
14.8	7.4	1
22.2	7.4	2
29.6	7.4	3
37	7.4	4
44.4	7.4	5
51.8	7.4	6
59.2	7.4	7
66.6	7.4	8
74	7.4	9
81.4	7.4	10
88.8	7.4	11
96.2	7.4	12
103.6	7.4	13
111	7.4	14
118.4	7.4	15
125.8	7.4	16
133.2	7.4	17
140.6	7.4	18
148	7.4	19
155.4	7.4	20

The Terramechanics Rig only allows for the testing of one tire at a time, while the speed of both motors can have multiple iterations per test run. While this meant that multiple slip

ratios could be explored during one test, it was decided that the most accurate readings would be accomplished utilizing the full length of the test surface to test one slip ratio. A testing matrix was developed from the previous parameters and can be seen in Table 6-2

Table 6-2. Test Parameters.

Testing Matrix				
	# of Parameters / Levels	**Level 1**	**Level 2**	**Level 3**
Tire Setup	2	Smooth Tread (No Tread)	Winter Tread	
Temperature Condition	1	Below Freezing -5 ˚C (23 F)		
Tire Inflation Pressure	2	26 PSI (141.26 kPa)	35 PSI (241.32 kPa)	
Normal Load	2	1488 lbf (6619 N)	1984 lbf (8825 N)	
Slip Ratio	3	0	10	20

At first it appeared that this design could be completed using a full factorial design. This however proved to be incorrect as the possibility of having to change the tire setup for each test run would be extremely time-consuming and impractical. For this reason a split-plot design using the "Custom Design" design of experiment (DOE) tool in JMP 8 was required. A screen capture of the tool can be seen in Figure 6-3.

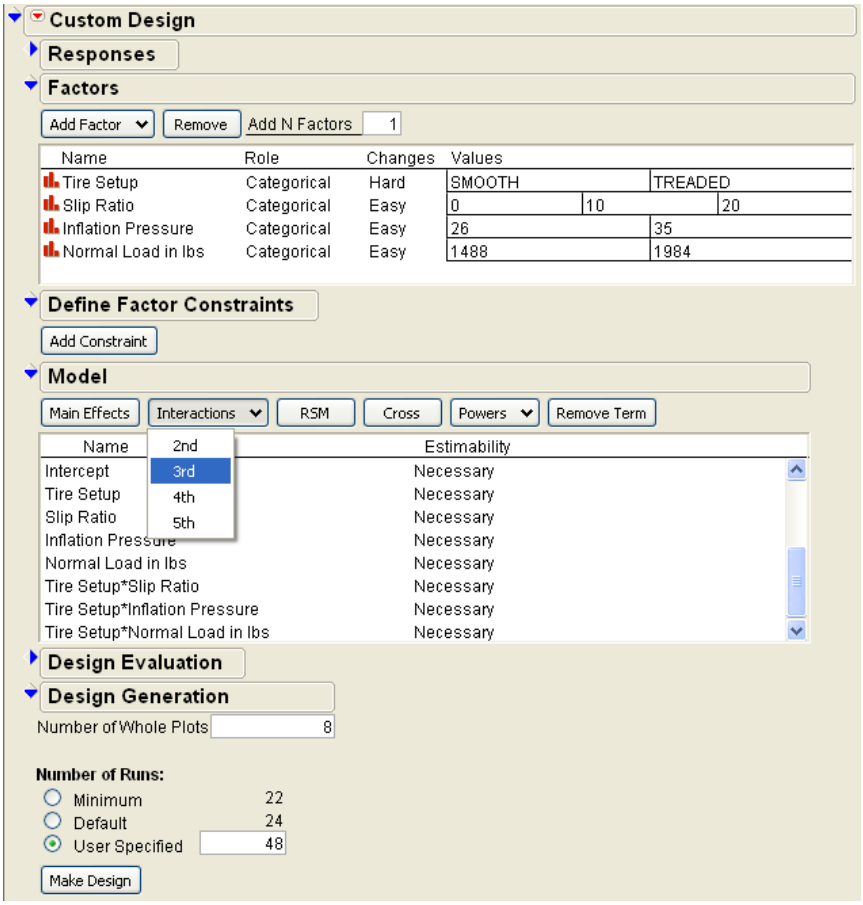

Figure 6-3. Setting up the third-order interactions in JMP 8.

The first step in the custom design was to set up the responses, which were the "calculated friction" and "drawbar pull." The second step was to define the factors, which were the "tire setup," "normal load," "inflation pressure," and the "slip ratio." The tire setup was a dichotomous or qualitative variable known as "categorical" variable in JMP. The normal load, inflation pressure, and slip ratio were qualitative variables labeled as "continuous" variables in JMP. However, in order to get the three levels of the slip ratio and an even number of combinations between each level, the slip ratio was changed to a 3-level categorical variable. The "changes" category allows a user to setup how *difficult* it is to modify a factor (and create split plot designs, split-split plot designs, and so on). The "tire setup" was set to "Hard" in order

to create the whole plot level, since changing the tire for each test run would be extremely time consuming and physically demanding. It was not necessary to "Define Factor Constraints" for this experiment because all of the factors could be varied independently of one another.

The "Model" category specified what effects and interactions were being analyzed in the design of experiment. The default was only the singular or "main" effects, which were filled with the "tire setup," "normal load," "inflation pressure," and the "slip ratio." With all of the factors except the slip ratio having two levels, the "interaction" button was used to create all of the third and second order interactions (three-way and two-factor interactions) in one step. The "Fraction of Design Space Plot" and "Relative Variance of Coefficients" were also ignored for this experiment.

If the design had been a full factorial design, it would require 24 runs to complete one set of data. To alleviate possible measurement errors, it has been decided that three runs will be performed for each configuration in the design of experiment, and the values averaged. Thus, three iterations would require 72 runs total. In order to have three data points for each test combination and carry out a reasonable amount of tests per day, the split-plot design used 12 whole plots to create 12 random tire changes. After randomizing the twelve whole plots, the other factors were randomized within each whole plot. This was carried out using the "Number of Whole Plots" setting set to 12. The "Number of Runs" was set to the "User Specified" amount of 72—which was randomized based on the whole plot instead of being completely random and required an even greater amount of time to complete all of the tests. After this was completed, the "Make Design" button did just that. The first section of this design can be seen in Table 6-3.

Table 6-3. Example of the design created by JMP with spaces marked with dots for user input of the observed data.

	Whole Plots	Tire Setup	Slip Ratio Setting	Inflation Pressure	Normal Load	Drawbar Pull	CALC Friction
1	1	TREAD	10	26	1488	-435.38	0.13205262
2	1	TREAD	0	26	1984	877.49	-0.2002183
3	1	TREAD	20	35	1488	-513.9	0.15355141
4	1	TREAD	0	35	1984	1075.9	-0.2527302
5	1	TREAD	10	35	1488	-378.93	0.11825452
6	1	TREAD	0	26	1488	882.48	-0.272388
7	2	TREAD	20	35	1984	-538.04	0.12291625
8	2	TREAD	10	35	1488	-72.741	0.0276929
9	2	TREAD	20	26	1984	-490.54	0.12201563
10	2	TREAD	10	26	1984	-494.85	0.11656392
11	2	TREAD	10	35	1984	-448.21	0.10045245
12	2	TREAD	0	26	1984	1312.4	-0.3073515

After a design has been randomly created from JMP, the "Design Generation" category becomes the "Design" category and displays the table with the randomly generated test combinations. From there, JMP allows a user to modify the "Prediction Variance Profile," "Fraction of Design Space Plot," "Prediction Variance Surface," and "Relative Variance of Coefficients"—which again were unnecessary for this experiment. Under the "Output Options" partition, the "Make Table" button created a copy of the table of values with space to input the responses for each test run.

After the responses were collected in the table, the "Model" command "run script" was used to bring up the "Fit Model" dialog that allows a user to determine exactly what parameters they want to analyze. Using the "Run Model" command, the proper analysis was carried out and the results generated. The results show the probability that specific interactions are statistically relevant. This analysis is covered in the next section.

6.2 Design of Experiment: Test Procedure and Slip

For each set of runs, a series of steps were performed in order to change all the parameters and do so in a timely fashion. Additionally, while power was going to the rig and work needed to be completed, the keyed emergency shutoff nearest the Terramechanics Rig computer was turned off and the remote for the Rig was turned off. This ensured that no power was going to the system so that an accident such as a dropped remote will not trigger movement in the carriage or tire. The Kistler sensor had to be at a height that the tire could be rotated in place to re-calibrate it after it was mounted. This required the use of the pulley system mounted to the top of the carriage. This pulley used a ratchet mechanism and had to be manually ratcheted by physically climbing on top of the carriage to turn the mechanism with a socket wrench.

The first step was to mount a tire or change the tire depending on the test. The five-point rims on which the tires were mounted on used a central disc that located (centered) the tire and wheel on the Kistler hub. These pair of discs were made of aluminum and made to fit the rim firmly to the central nub on the Kistler sensor. The rims were held in place with five 9/16 inch (1.43 cm) diameter and 1.5 inch (3.81 cm) length hex bolts. Each time the tire was re-installed, these bolts were removed and re-installed using a compressed air ratchet. Completely changing tires required approximately eight minutes for one person to complete due to the weight of the tire (65 lbf, 222.41 N) and the need to mount the tire vertically while lining up the five holes—a tough task because of the small area ledge of the hub used to balance the tire on. At this point, the tire pressure could also be checked using the inflation gun. The PiCPro program for a specific test was also loaded at this time.

The entire resurfacing process took between one and two hours to complete. Waiting for the ice to refreeze took up the bulk of this time. Resurfacing was necessary when the available testing surface was completely used up (when the tire had run once across all of the resurfaced ice), before the very first test of the day, or if there were noticeable irregularities on the ice surface. The first step for this process was to scrape the very top of the ice with the floor scraper—going over the portion of the ice that would be tested upon—until the blade moved smoothly across the surface. This process took a little under 5 minutes to complete. Afterwards this blade was dried off to limit the amount of rust that would form on the carbon steel blade.

The second step was to manually soak the resurfacing towel with warm water from the faucet near the Terramechanics Rig (so that the towel was completely wet and slightly dripping). This water was approximately 110 °F (43.33 °C) after being warmed up for a few minutes at the faucet. This resurfacing towel was connected to a hand-made "T"-shaped assembly that allowed the towel to be drawn across the testing surface while lightly wetting the surface. In some cases this layer of water froze within half an hour, but for nearly all of the tests, it took one to two hours for this layer of water to freeze.

The next steps were to calibrate the sensor while it was in the air, lower the tire, and then inflate the air springs to get the correct normal load. The tire was calibrated by spinning it in place at a rate of 250 degrees per second (approximately 162 cm/s or 3.62 mph tangential speed). This calibration spin was stopped and the remote turned off; then the tire would be lowered directly onto the ice. The pulley would then be removed from the motor assembly to ensure that there was nothing holding it up [besides the tire]. Next the system was loaded to the desired normal load, confirmed with the Kistler hub. This was done by using the inflation gun and manually monitoring the force reading in the z-axis on the Remote Emulator. The sensor hub

with a tire gave a reading of approximately -380 to -400 N when hanging in the air, as the z-axis of the Remote Emulator treats any forces exhibited downward on the sensor as negative, and any ground forces pushing on the bottom of the sensor as positive. This meant that the sensor assembly, hub adapter, and tire weight had to be subtracted from the reading on the Remote Emulator in order to get the correct load. These steps required up to approximately 5 minutes to complete.

Once these physical parameters were setup, the first test run could be conducted within a few minutes of calibrating the sensor. These readings would be collected through the LMS Test.Lab software. Once a successful test was completed, the test run data would be accepted and a new movement program would be loaded for the next test scenario. The rig would be moved back into a convenient position for access, and the power to the rig would be cut off using the key and the remote. Afterwards, the sensor and tire had to be raised off of the ground, the inflation pressure was changed if necessary, and the Kistler sensor was spun in place and recalibrated. Additionally the carriage would be moved laterally to a fresh portion of the ice surface. These steps could be repeated three or four times depending upon the condition of the available ice test surface. Once this was completed, the tire would be raised a final time and the power to the Terramechanics Rig would be shut down. The tangential speed at the tire, the carriage speed (i.e., vehicle speed), the slip ratio, and the slip velocity are presented in Table 6-4.

Table 6-4. Ladder Units per minute (LU/min) values utilized in PiCPro to control the movement of both axes of the Terramechanics Rig.

Tire Speed (cm/s)	***Tire Speed (LU/min)***	Vehicle Speed (cm/s)	***Vehicle (LU/min)***	CALCULATED SLIP RATIO	CALCULATED SLIP SPEED
0	***0.00***	7.4	***255417.8709***	-1	-7.4
7.4	112,130.69	7.4	255417.8709	0	0
14.8	***224,261.38***	7.4	***255417.8709***	1	7.4
22.2	***336,392.07***	7.4	***255417.8709***	2	14.8
29.6	***448,522.76***	7.4	***255417.8709***	3	22.2
37	***560,653.45***	7.4	***255417.8709***	4	29.6
44.4	***672,784.14***	7.4	***255417.8709***	5	37
51.8	***784,914.83***	7.4	***255417.8709***	6	44.4
59.2	***897,045.52***	7.4	***255417.8709***	7	51.8
66.6	***1,009,176.21***	7.4	***255417.8709***	8	59.2
74	***1,121,306.90***	7.4	***255417.8709***	9	66.6
81.4	1,233,437.59	7.4	255417.8709	10	74
88.8	***1,345,568.27***	7.4	***255417.8709***	11	81.4
96.2	***1,457,698.96***	7.4	***255417.8709***	12	88.8
103.6	***1,569,829.65***	7.4	***255417.8709***	13	96.2
111	***1,681,960.34***	7.4	***255417.8709***	14	103.6
118.4	***1,794,091.03***	7.4	***255417.8709***	15	111
125.8	***1,906,221.72***	7.4	***255417.8709***	16	118.4
133.2	***2,018,352.41***	7.4	***255417.8709***	17	125.8
140.6	***2,130,483.10***	7.4	***255417.8709***	18	133.2
148	***2,242,613.79***	7.4	***255417.8709***	19	140.6
155.4	2,354,744.48	7.4	255417.8709	20	148

In Summary, the procedure for each test was:

1) Engage the safety mechanisms—the key shutoff and power off the remote
2) Mount the tire in the air
3) Check and/or change the inflation pressure
4) Load the PiCPro program for a specific movement/test scenario
5) Resurface the ice with the floor scraper and resurfacing towel
6) Allow 10-15 minutes for the ice to freeze
7) Lower the carriage and set the appropriate normal load using the Kistler sensor
8) Carry out the specific program/test
9) Collect the data in LMS and accept the results if the test was successful
10) Turn off the power to the rig when it is in a place where the parameters can be physically adjusted
11) Raise the sensor/tire and repeat steps 4 through 10 as needed.
12) Turn off the power to the Terramechanics Rig when all the necessary tests were completed and raise the tire off of the ice surface.

7 Results and Discussion of Results

The readings from the Kistler sensor are based on the ISO 4130 coordinate system seen in Figure 7-1. For all of the tests, the data has been recorded starting the carriage in the negative direction of the x-axis of the Kistler system, i.e., moving towards the computer desk in the lab. It was observed that if the wheel is moving faster than the Terramechanics Rig's carriage, or the "vehicle," that there will be a net negative force in the forward direction—which is the negative x-axis of the Kistler system meaning a negative value read for the drawbar pull, for example. Conversely, if the carriage, or vehicle, is moving faster than the tire—a negative slip ratio condition—there is a net positive force read by the system.

If the tire is dragged forward by the carriage/vehicle, the force is actually positive in the x-axis. At the hub, where the Kistler sensor is located, this force will be read as negative. In comparison, if the tire was simply dragged along in the forward direction, the force acting on the tire would be positive.

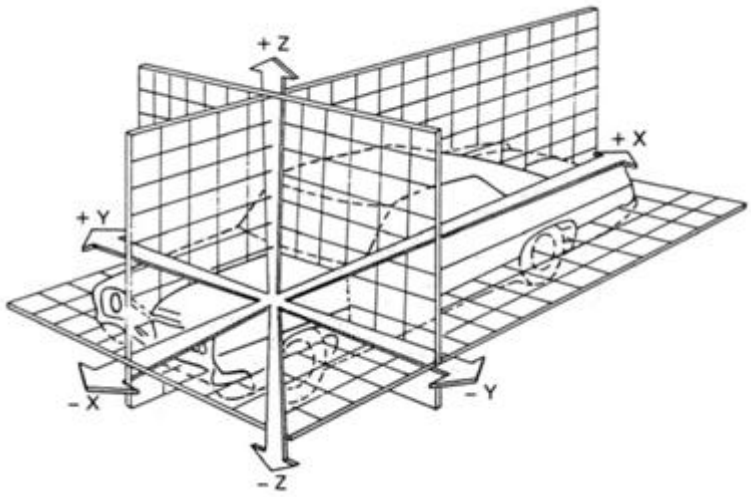

Figure 7-1. Depiction of the ISO 4130 coordinate system (modified picture).

In order to directly compare the data observed to the data from published studies, the collected data was transformed to the SAE system. The coordinate system can be seen in Figure 7-2.

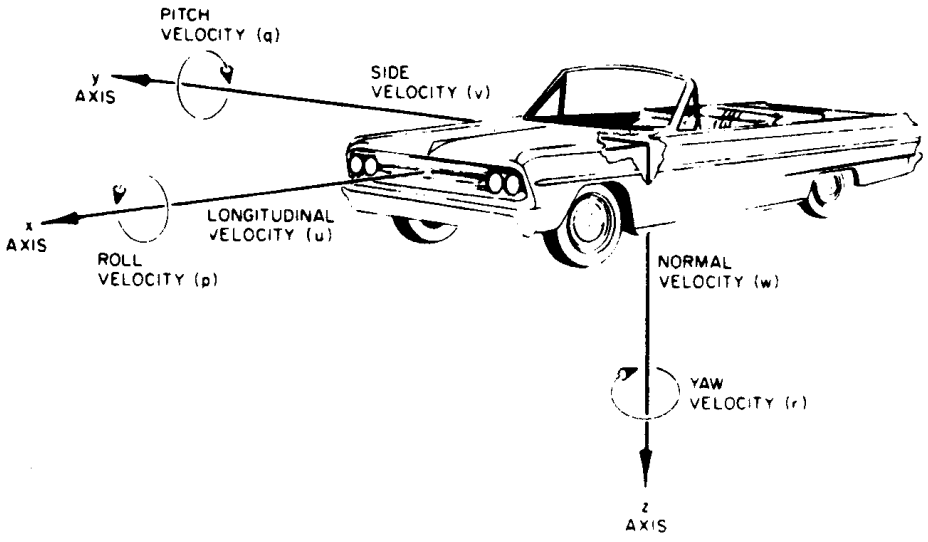

Figure 7-2. The SAE coordinate system [64].

7.1 Results and Discussion of Results: Filtering the Data

JMP's custom design tool allowed for a completely randomized set of test combinations. This plan of action dictated the order in which these tests were carried out. Each test run, ignoring the preparation, ran for approximately 80 seconds. Observing the data in LMS Test.Lab, the normal force (Figure 7-3) in every test run followed a sinusoid-like curve. The pattern of the curves is more than likely from the rotation of the sensor and tire assembly, as there could be imbalances in the sensor and the tire that could not be accounted for. Furthermore the system is rotating, and the recording of a rotating sensor would naturally be a sinusoidal curve. Regardless of the tire tread, both tires had jagged normal load curves at higher slip ratios.

Figure 7-3. The normal force on the tire measured in the same direction as the positive z-axis by the Kistler hub [65].

It can be noticed from Figure 7-4 that the normal load measured by the system stayed within about ±5% of the nominal value for the first 70 seconds of testing. After all of the data was collected, it had to be exported one axis at a time as a text file. These data files were imported into Matlab. Matlab code was written to filter the data at a Nyquist frequency of 80 Hz with a cutoff frequency of 6. The filter was a fourth-order Butterworth filter, which would have a minimal "rippling" effect while filtering the data. The accuracy of the study has been improved by reducing the variation of the normal load data, which was done by using only the data recorded for a normal load that fell within ±2% of the nominal value.

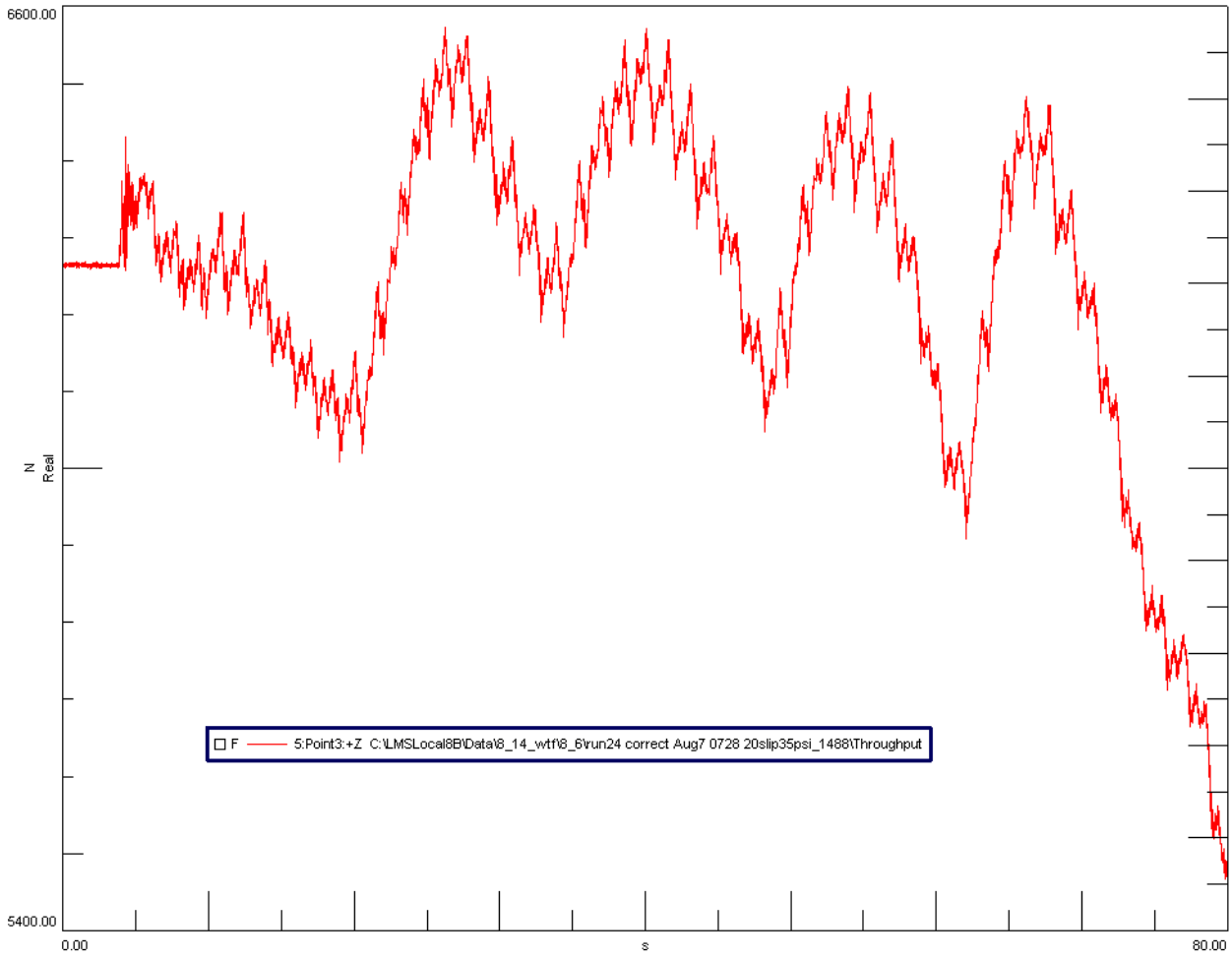

Figure 7-4. Example of z-value test data observed in LMS Test.Lab. The pattern of the load is sinusoidal but has jagged peaks. This data would be filtered before usage.

The noise observed in this signal could have come from numerous sources. The spinning Kollmorgen AKM73P electric motor made a constant whining sound as it rotated. This could have from load variations inside the motor, the tolerance of the components, the speed of the spinning motor, or a number of unknown variables. Additionally this electric motor was mated to a gearbox for a 60:1 reduction; the gearbox could have created more friction and noise from the reduction gearing. The range of the test values was taken as an offset of the signal from the Kistler sensor. This meant that the weight of the tire with tread (and sensor elements), which

read as -380 N in the air, was subtracted from the reading on the ground, 8445 N, to obtain the required 8825 N (1984 lbf) test level. Similarly, the low normal force test level of 6620 N (1484 lbf) was read as 6240 N at the sensor, and had a range of 6115.2 to 6364.8 N. The data for the each run was then averaged to obtain one data point in the design of experiment. The complete set of data collected is found in Appendix B.

The filtered data was next input into [the table created in] JMP. An excerpt of the data is given in Table 7-1.

Table 7-1. An excerpt of the data in the table generated and filled in JMP 8.

	Whole Plots	Tire Setup	Slip Ratio Setting	Inflation Pressure	Normal Load	Drawbar Pull	CALC Friction
1	1	TREAD	10	26	1488	-435.38	0.13205262
2	1	TREAD	0	26	1984	877.49	-0.2002183
3	1	TREAD	20	35	1488	-513.9	0.15355141
4	1	TREAD	0	35	1984	1075.9	-0.2527302
5	1	TREAD	10	35	1488	-378.93	0.11825452
6	1	TREAD	0	26	1488	882.48	-0.272388
7	2	TREAD	20	35	1984	-538.04	0.12291625
8	2	TREAD	10	35	1488	-72.741	0.0276929
9	2	TREAD	20	26	1984	-490.54	0.12201563
10	2	TREAD	10	26	1984	-494.85	0.11656392
11	2	TREAD	10	35	1984	-448.21	0.10045245
12	2	TREAD	0	26	1984	1312.4	-0.3073515
13	3	SMOOTH	20	26	1984	-168.74	0.04723988
14	3	SMOOTH	0	26	1488	79.04	-0.008788
15	3	SMOOTH	10	35	1488	-129.48	0.04077419
16	3	SMOOTH	10	35	1984	-162.17	0.0396151
17	3	SMOOTH	20	35	1984	-187.83	0.04728295
18	3	SMOOTH	20	35	1488	-111.09	0.03529537
19	4	TREAD	0	26	1488	921.47	-0.2849317
20	4	TREAD	0	35	1488	679.09	-0.210496

7.2 Results and Discussion of Results: Observed Data

A table containing all the experimental results is found in Appendix B. It was found that the values for the drawbar pull (force in the x-axis) were negative while the torque (moment about the y-axis) was positive for all tests with positive slip. As mentioned earlier, the Kistler P650 records data using as the sign convention of the ISO 4130 coordinate system that has the force in the x-axis pointing in the opposite direction of forward motion. Utilizing the data collected, the coefficient of friction was calculated from the drawbar pull using equation (8.1):

$$DP = F_{tractive} - F_{resistive} = \frac{T}{r} - \left(\mu_{rolling}\right) F_z \tag{8.1}$$

The drawbar pull, *DP*, is the net force of the tractive force (or tractive effort) minus the resistive force (or resistive effort). The tractive force is the torque, *T*, divided by the effective rolling radius of the tire, r_{eff}. The resistive force or rolling resistance, $F_{resistive}$, is the product of the rolling friction coefficient, $\mu_{rolling}$, and the force in the z-axis. The equation can be rewritten to solve for the rolling coefficient of friction:

$$\mu_{rolling} = \frac{-DP + \dfrac{T}{r_{eff}}}{F_z} \tag{9.2}$$

For each configuration in the test matrix, the values were eventually tested three times, each in the randomized set of test runs. The drawbar pull and the torque for each set was averaged among the three runs for each combination of parameters. The average rolling resistance was calculated at each of these set of averaged points, seen in Figure 7-5 (for the smooth tire) and in Figure 7-8 (for the winter tread tire). The normalized drawbar pull can be seen in Figure 7-6 (smooth tire) and in Figure 7-10 (winter tread tire). The normalized tractive effort is given in Figure 7-7 (smooth tire) and in Figure 7-11 (winter tread tire).

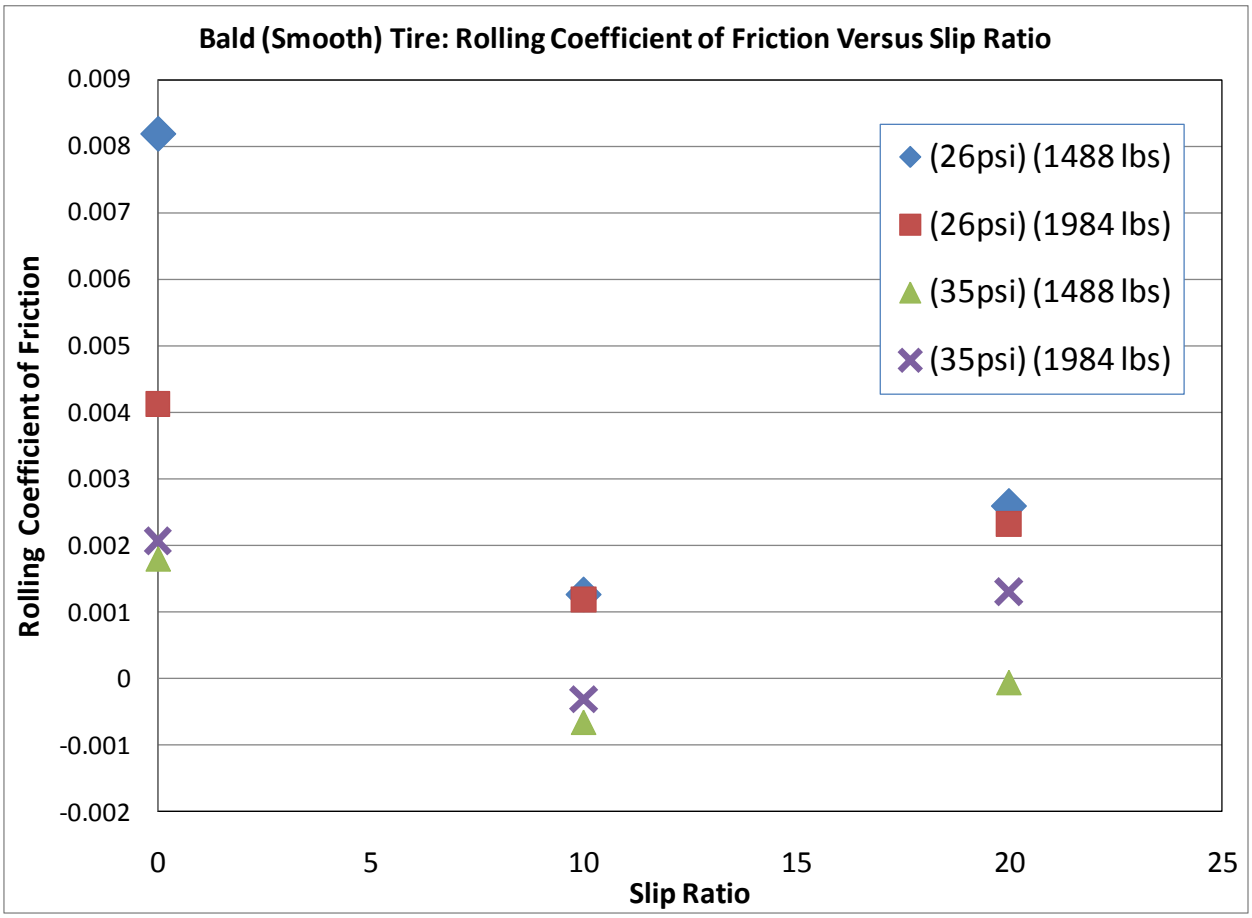

Figure 7-5. Coefficient of rolling friction versus the slip ratio for the bald (smooth) tire.

The coefficient of rolling friction for the smooth tire followed a similar trend for each test run. The biggest difference in the observations of the data was the inflation pressure at different slip ratios. It was expected that the slip ratio would continually decrease as the slip ratio

increased, but for the smooth tire the calculated coefficient of friction increased as the slip ratio changed from 10 to 20.

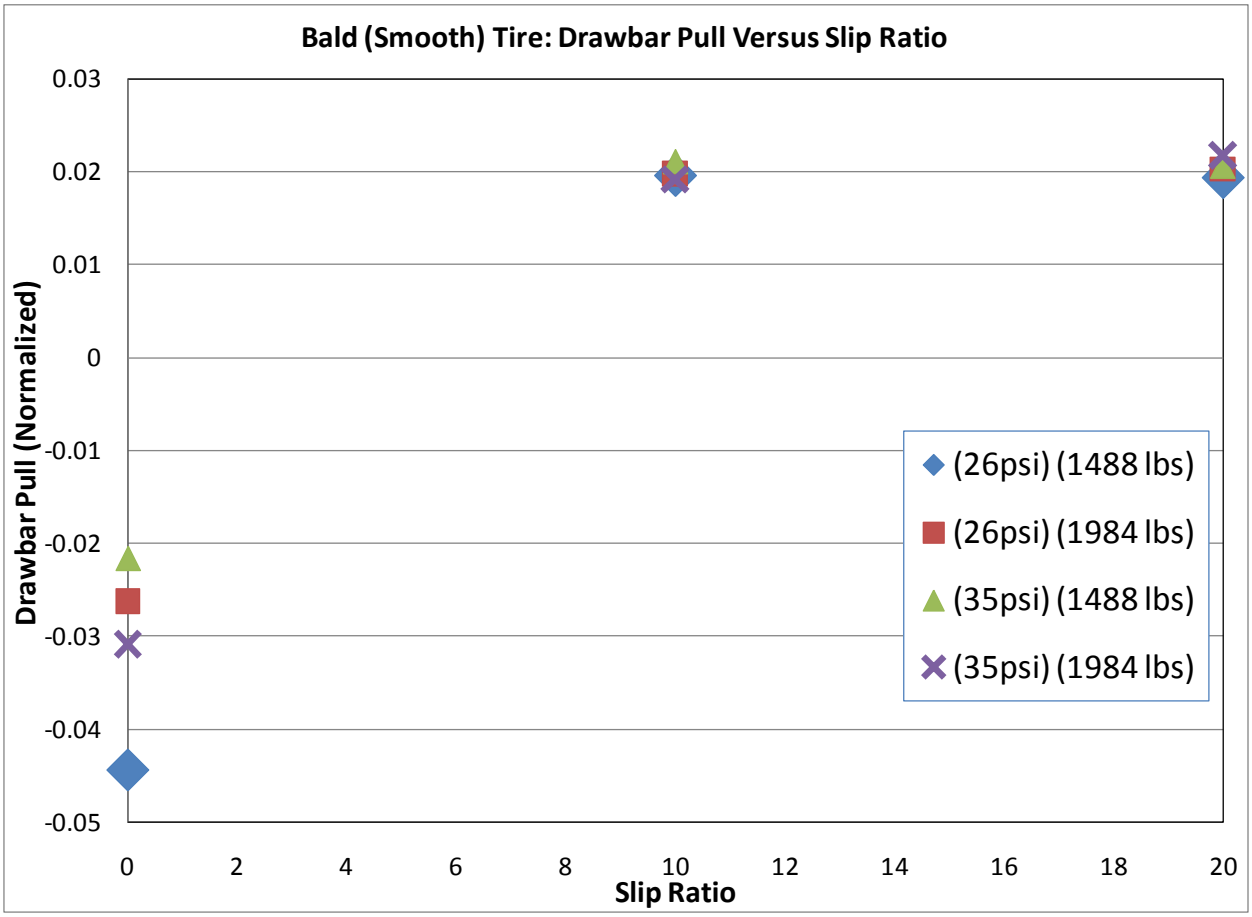

Figure 7-6. The normalized drawbar pull versus slip ratio for the bald (smooth) tire.

The drawbar pull for the smooth tire increased as the slip ratio increased. The drawbar pull for the smooth tire had a similar trend for each combination of experiments. This shape and direction of this trend is similar to the data observed from the Terramechanics Rig for tests conducted with the lunar soil simulant GRC 1.

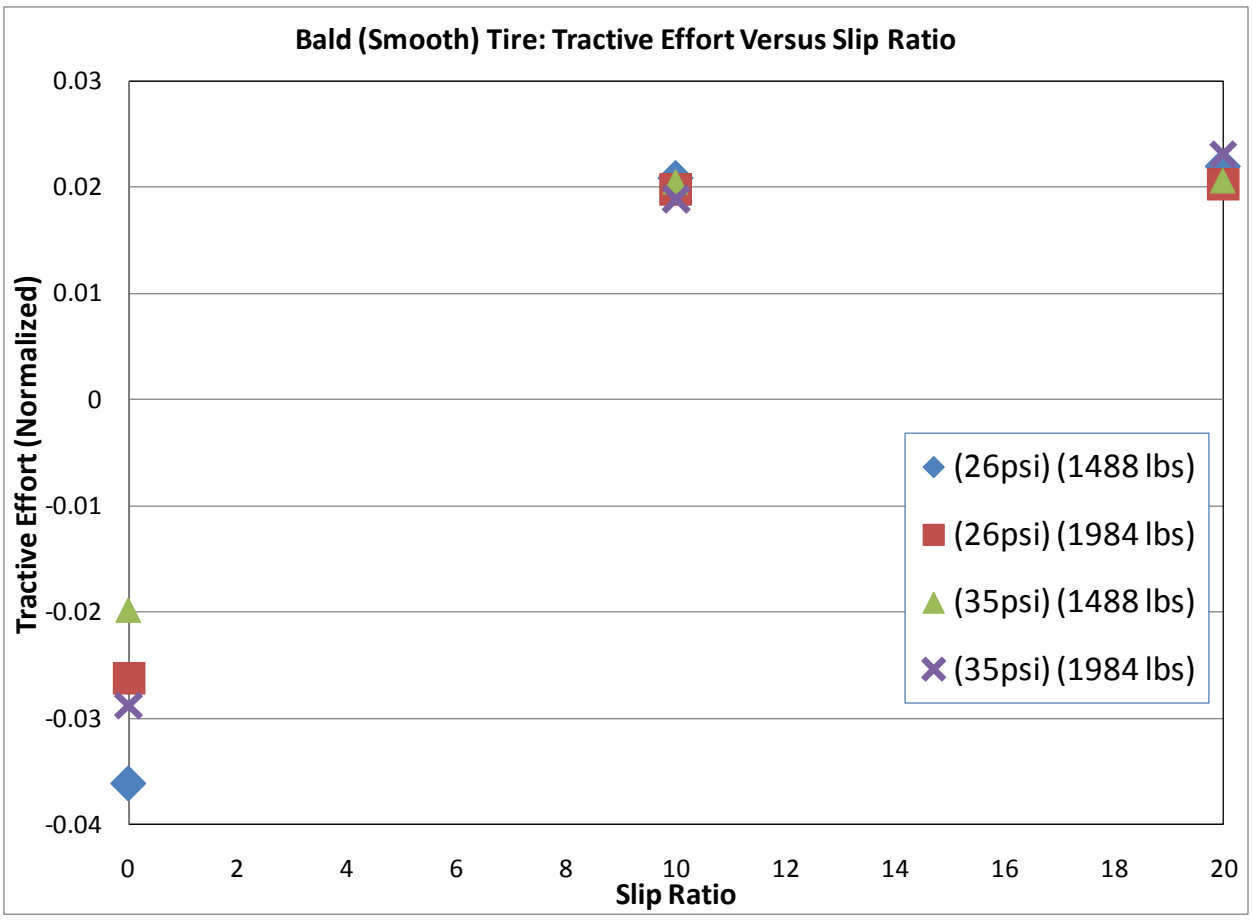

Figure 7-7. The normalized tractive effort for the bald (smooth) tire.

The normalized tractive effort followed an almost identical pattern to the normalized drawbar pull. The tractive effort increased as the slip ratio increased. This illustrates that the applied torque also increased with the increase in velocity of the tire.

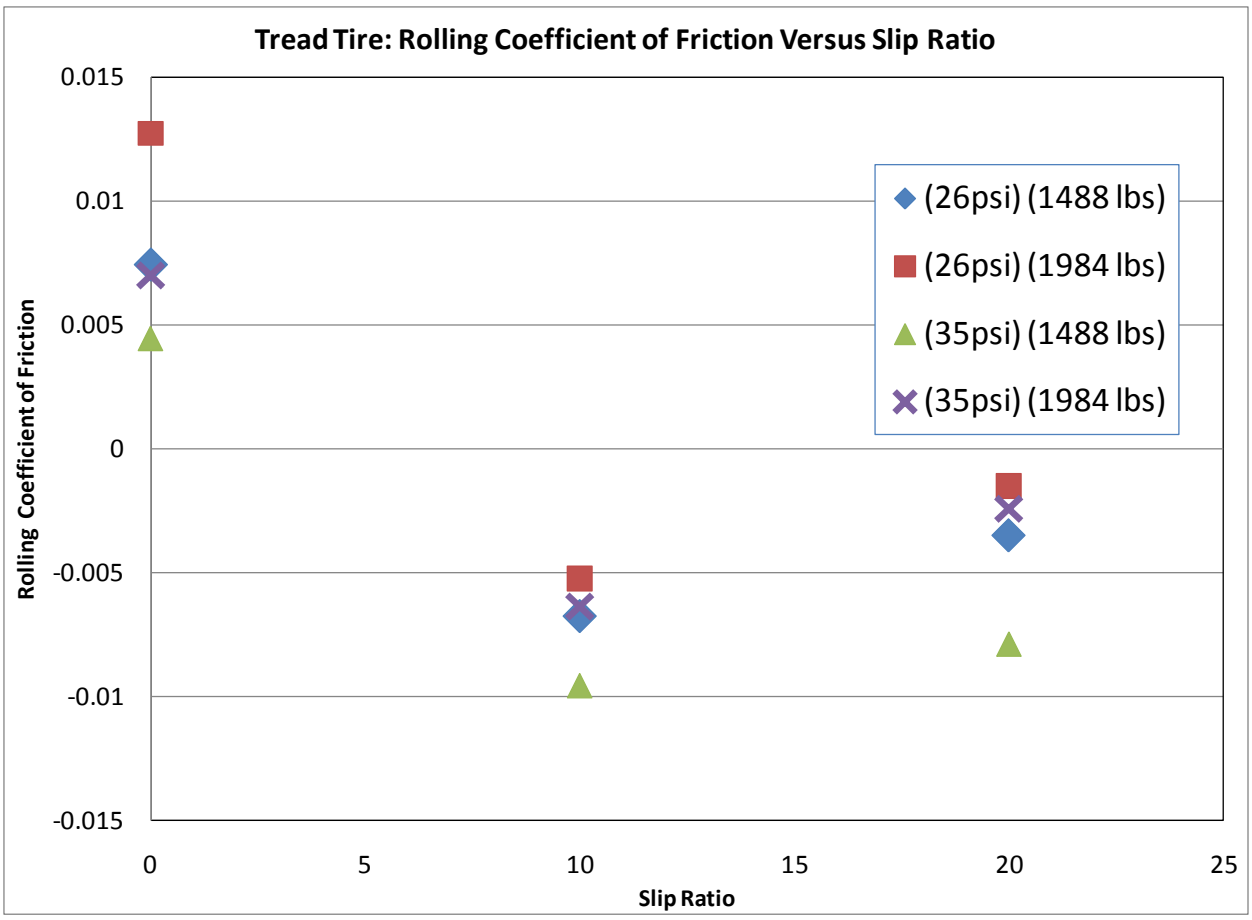

Figure 7-8. Coefficient of rolling friction versus the slip ratio for the tire with the winter tread pattern.

The coefficient of rolling friction for the tire with the winter tread pattern followed a similar trend for each test run. The biggest difference in the observations of the data was the inflation pressure at different slip ratios. It was expected that the slip ratio would continually decrease as the slip ratio increased, but for the tire with the winter tread pattern the calculated coefficient of friction increased as the slip ratio changed from 10 to 20. There was a noticeable difference between the tests of the winter tread pattern tire at the inflation pressure of 35 psi (241.32 kPA) and 1488 lbf

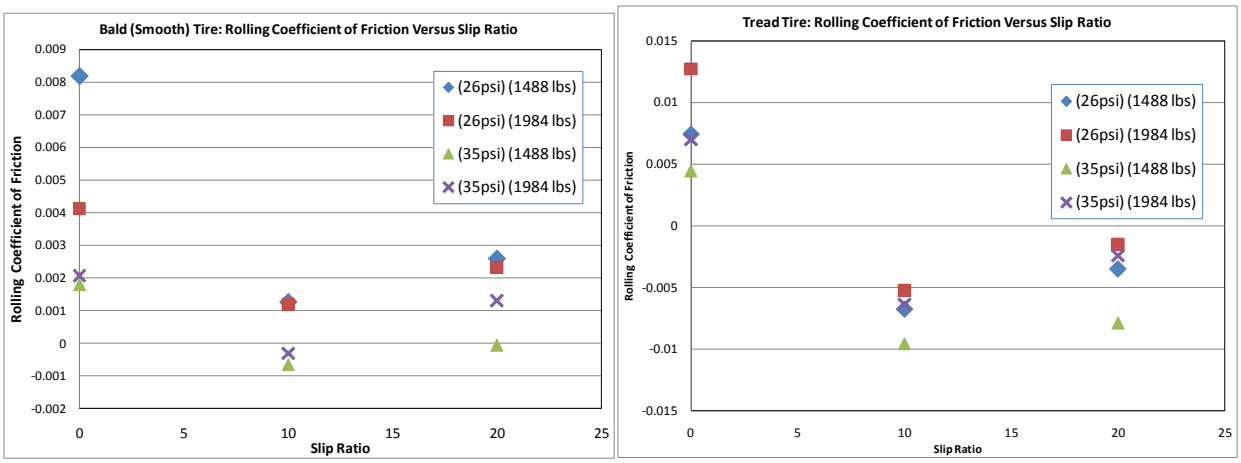

Figure 7-9. Comparison of the two coefficients of rolling friction.

The calculated coefficient of rolling friction was slightly higher for the tire with the winter tread pattern at zero slip, seen in Figure 7-5, Figure 7-8, and Figure 7-9. As the slip increased in this experiment, the bald tire had a slightly higher calculated coefficient of friction for a slip ratio of 10 and 20. Since these figures are calculated from actual recorded data, it can be assumed that there may be a slight error in the rolling coefficient of friction, because any adjustment of the effective rolling radius would change the direction and position of the calculated coefficient of rolling friction. A smaller effective rolling radius would increase the coefficient of rolling friction in the positive direction. A larger effective rolling radius would increase the coefficient of rolling friction in the negative direction, making the coefficient of rolling friction "negative" in terms of the calculation.

It can be assumed that the scale of the numbers was affected by the test conditions. Despite efforts to test at the coldest temperatures during the night, the temperature of the air was much higher than the ice and it can be assumed that this promoted a water layer that may not have been completely visible. Alternatively, the difference in the bulk ice temperature and the

ambient air may have promoted the formation of a larger water layer than would be naturally observed [if the temperature of both sources was below freezing]. These conditions could have led to a "wet" ice or non-dry test scenario. This increased water layer may have led to the Rig creating less torque than it would have used to overcome completely "dry" friction, and in turn would lower the recorded drawbar pull or force in the x-axis.

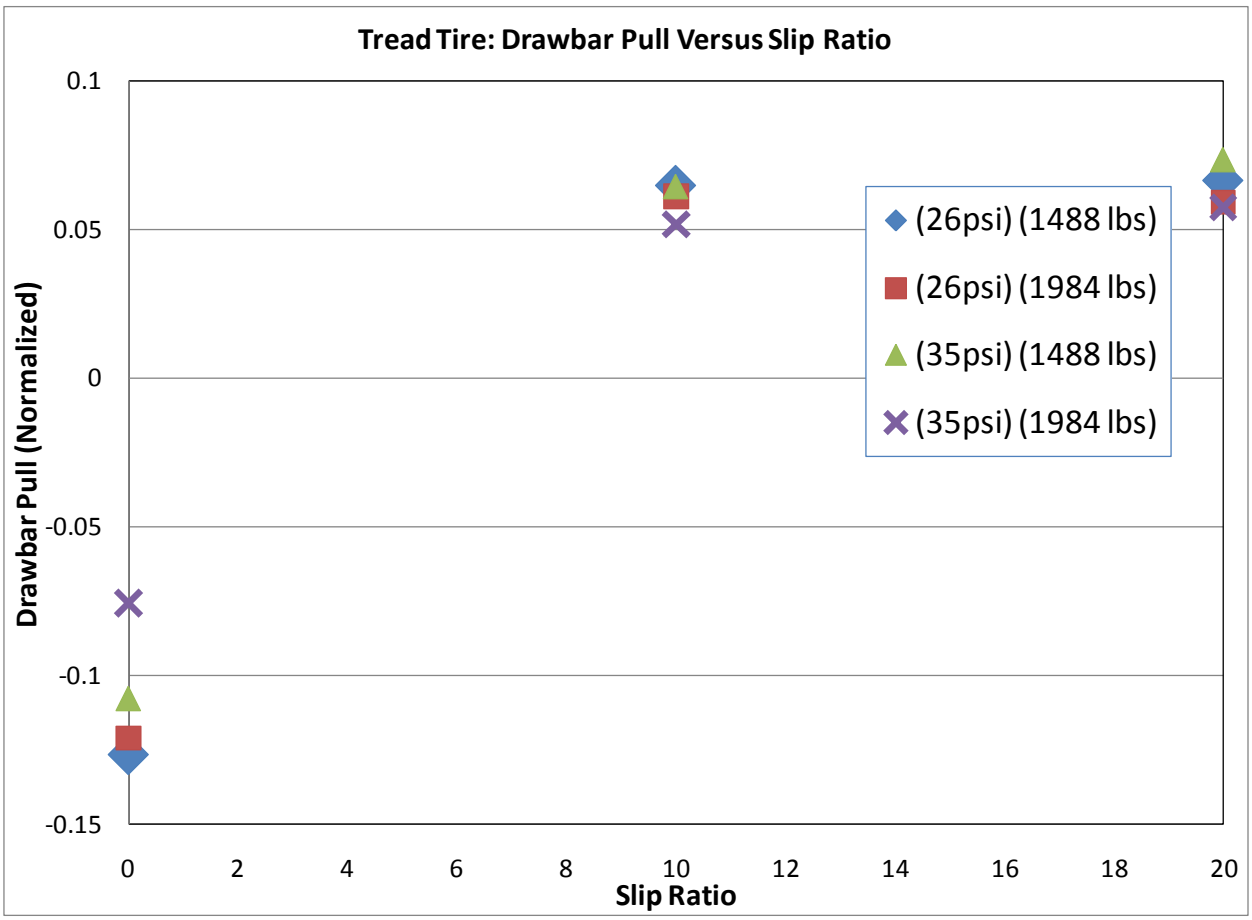

Figure 7-10. The observed drawbar pull versus slip ratio for the tire with tread.

The drawbar pull for the tire with the winter tread pattern increased as the slip ratio increased. The drawbar pull for the tire with the winter tread pattern had a similar trend for each

combination of experiments. This shape and direction of this trend is similar to the data observed from the Terramechanics Rig for tests conducted with the lunar soil simulant GRC 1.

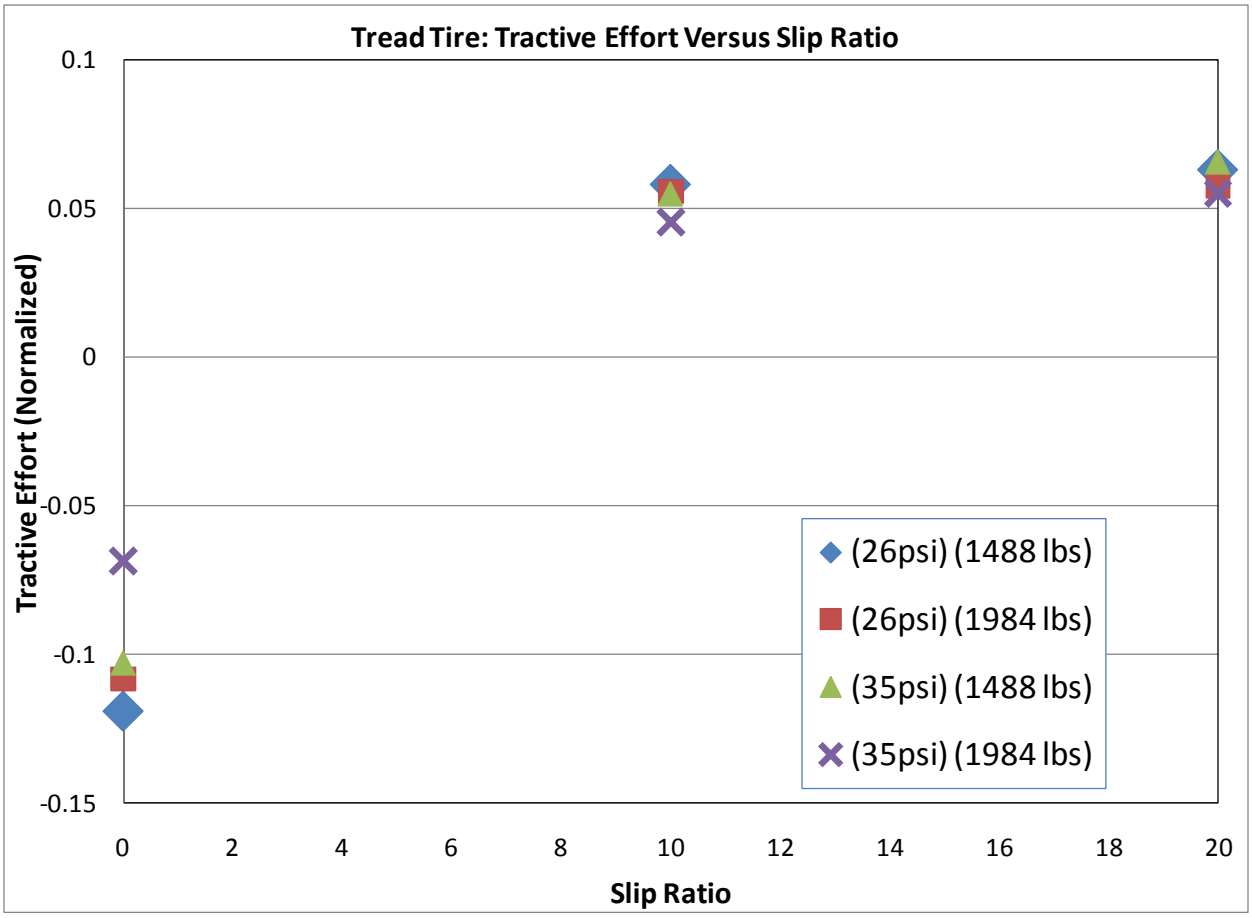

Figure 7-11. The normalized tractive force for the tire with tread.

The normalized tractive effort, Figure 7-11, for the tire with the winter tread pattern followed an almost identical pattern to the normalized drawbar pull measurements. The tractive effort increased as the slip ratio increased. This illustrates that the applied torque also increased with the increase in velocity of the tire.

The observed drawbar pull was lower for the bald tire (around 0.02 at a slip ratio of 10 and 20) than the observed drawbar pull for the tire with tread (around 0.05 at a slip ratio of 10 and 20). As the slip ratio increased, the drawbar pull on both tires increased with increasing slip ratio. Likewise, as the slip ratio increased, the tractive effort between the tire with tread and the ice increased. Each set of tires followed a similar trend. This data was taken at a temperature of approximately 72 °F (22.2 °C).

For comparison,we revisit the results presented in [7] for the coefficient of friction versus the slip ratio, shown in Figure 7-12, and versus the sliding speed, shown in Figure 7-13.

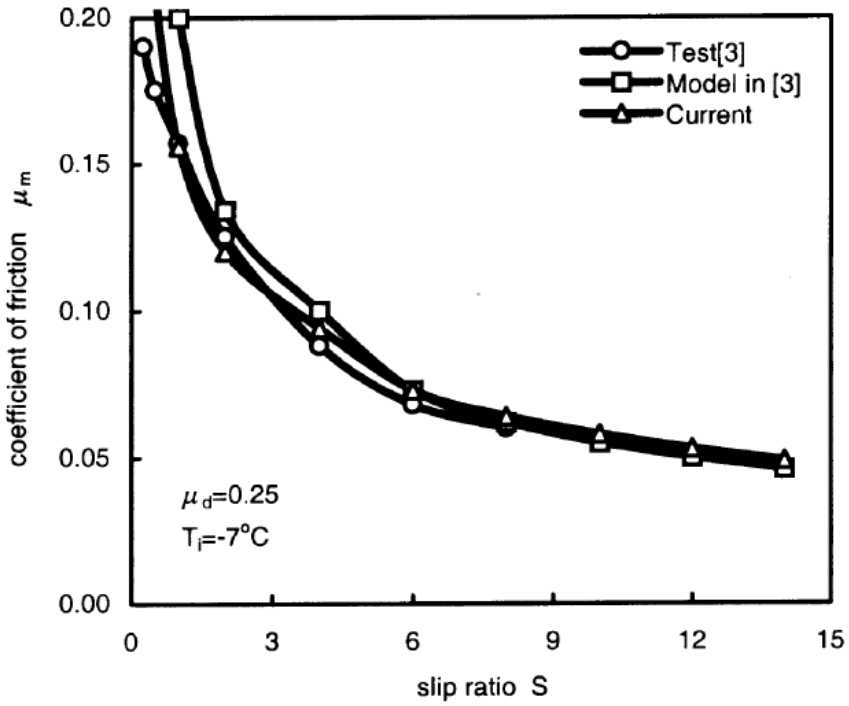

Figure 7-12. The coefficient of friction versus the slip ratio in a previous study, called the "traction force" [1].

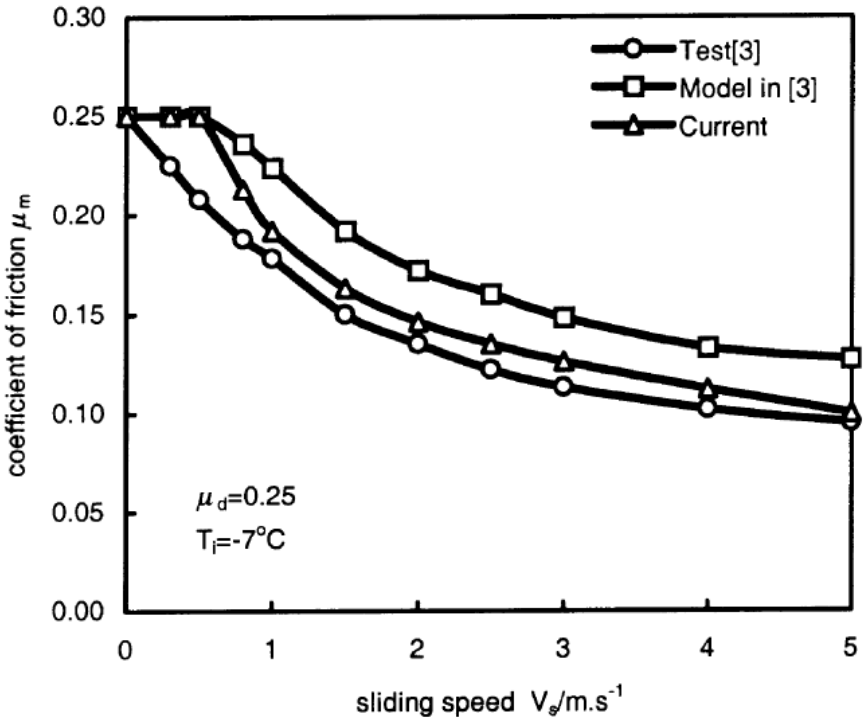

Figure 7-13. Locked tire coefficient of friction [1].

According to the observed results, the rolling coefficient of friction for the tires on ice slightly increased with increasing slip ratio. This was the opposite effect observed in previous studies, which have coefficients of friction that lower as the slip ratio and sliding speeds increase. The magnitude of the force in the x-axis or the drawbar pull observed from the Kistler sensor decreased as the slip ratio increased, indicating that the tires were slipping more on the ice and losing traction. The smooth tire had a smaller magnitude on the drawbar pull, indicating that it had less traction on the ice.

7.3 Results and Discussion of Results: Statistical Analysis

The model for the data collected in this study was setup using the restricted maximum likelihood (REML) method, seen in Figure 7-14. REML is used as a method to fit linear mixed models. This method is a standard analysis used by statisticians, for things such as finding missing data or in complex designs with multiple variance components. The nature of the custom design meant that the variance was estimated. This lead to degrees of freedom that depended upon the data—giving degrees of freedom that were not integers commonly seen in less complex experimental designs.

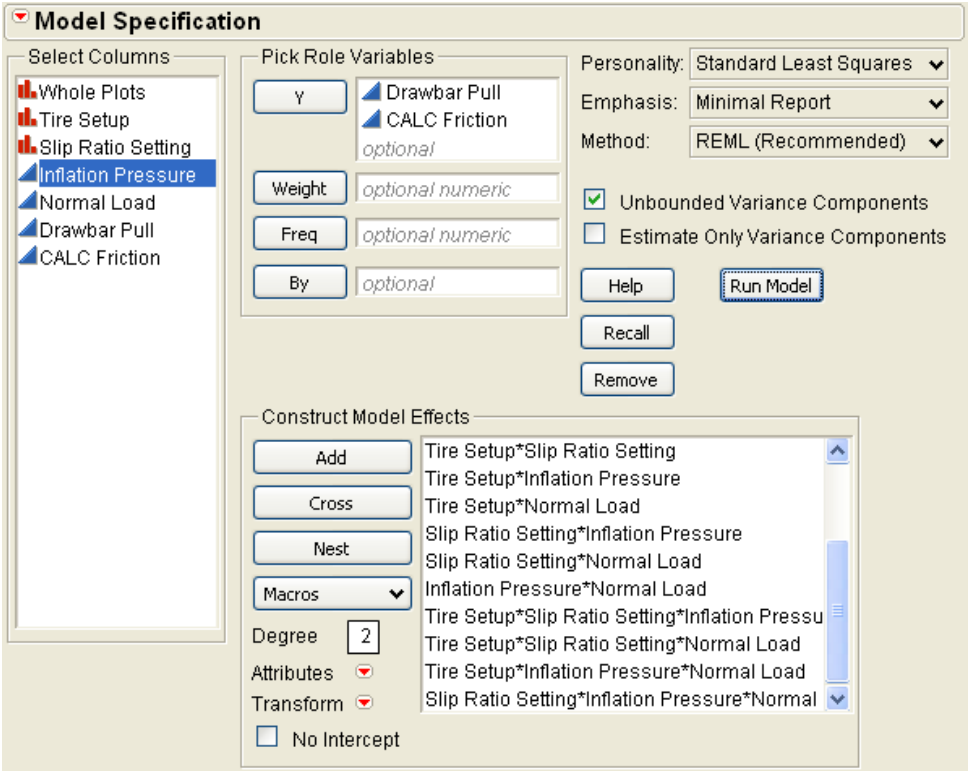

Figure 7-14. The model specification menu in JMP, used to create the model that will analyze the data.

The model provides parameter estimates or estimates of the factors that make up the full model of the response (drawbar pull). It also calculates the standard error and the probability of the factor affecting the response. This is done by using a hypothesis test that sets each parameter equal to zero in order to determine if its effect is "significant" or is a main factor in the response. The parameter estimates can be seen in Table 7-2. The data used in the analysis was left unadjusted, so that the response has the signs that were directly observed from the system.

Table 7-2. Table of the parameter estimates.

Parameter Estimates

Term	Estimate	Std Error	DFDen	t Ratio	Prob>|t|
Intercept	-36.99658	22.52855	6.73	-1.64	0.1463
Tire Setup[SMOOTH]	-1.706278	22.52855	6.73	-0.08	0.9418
Slip Ratio Setting[0]	514.65418	26.59088	41.82	19.35	<.0001*
Slip Ratio Setting[10]	-243.5216	26.59008	41.75	-9.16	<.0001*
Inflation Pressure(26,35)	-27.253	18.76696	41.5	-1.45	0.1540
Normal Load(1488,1984)	-22.33589	19.32899	46.45	-1.16	0.2538
Tire Setup[SMOOTH]*Slip Ratio Setting[0]	-304.6227	26.59054	41.89	-11.46	<.0001*
Tire Setup[SMOOTH]*Slip Ratio Setting[10]	135.76191	26.59018	41.75	5.11	<.0001*
Tire Setup[SMOOTH]*Inflation Pressure	4.315245	18.76698	41.56	0.23	0.8193
Tire Setup[SMOOTH]*Normal Load	0.2382187	19.32939	46.45	0.01	0.9902
Slip Ratio Setting[0]*Inflation Pressure	-70.78582	27.96827	48.94	-2.53	0.0146*
Slip Ratio Setting[10]*Inflation Pressure	50.271029	26.79277	43.25	1.88	0.0674
Slip Ratio Setting[0]*Normal Load	33.264381	27.33655	46.43	1.22	0.2298
Slip Ratio Setting[10]*Normal Load	-18.01132	26.74065	42.71	-0.67	0.5042
Inflation Pressure*Normal Load	-10.94727	19.46749	47.18	-0.56	0.5765
Tire Setup[SMOOTH]*Slip Ratio Setting[0]*Inflation Pressure	16.861169	27.96796	48.95	0.60	0.5494
Tire Setup[SMOOTH]*Slip Ratio Setting[10]*Inflation Pressure	-24.88954	26.79225	43.28	-0.93	0.3581
Tire Setup[SMOOTH]*Slip Ratio Setting[0]*Normal Load	-37.76086	27.33737	46.4	-1.38	0.1738
Tire Setup[SMOOTH]*Slip Ratio Setting[10]*Normal Load	27.467241	26.7412	42.77	1.03	0.3101
Tire Setup[SMOOTH]*Inflation Pressure*Normal Load	11.894069	19.46825	47.25	0.61	0.5442
Slip Ratio Setting[0]*Inflation Pressure*Normal Load	-18.7691	27.43451	47.02	-0.68	0.4972
Slip Ratio Setting[10]*Inflation Pressure*Normal Load	0.724105	27.72614	48.19	0.03	0.9793

In the model above, the slip ratio setting, the combination of the slip ratio and the tire setup, and the combination of the slip ratio and the inflation pressure were found to be significant. The parameter estimate broke apart the categorical variables of the slip ratio and the

tire setup. The slip ratio variable effect was reduced to two levels for the parameters. The slip ratio of 0 was compared to the slip ratio at 20. The slip ratio of 10 was compared to the slip ratio at 20. In this case, both slip ratio levels were significantly different from a slip ratio of 20.The fixed effects table can be seen in Table 7-3. The estimates column gave the coefficient for each term in the model created by the least squares method. The standard estimate is the standard deviation of the distribution of the given parameter estimate. "DFDen" is the degrees of freedom in the denominator. The t-ratio is the statistic is a ratio between the estimate and the its standard error, which can be used to determine if the given parameter is significant.

Table 7-3. Fixed effects test in JMP.

Fixed Effect Tests

Source	Nparm	DF	DFDen	F Ratio	Prob > F
Tire Setup	1	1	6.73	0.0057	0.9418
Slip Ratio Setting	2	2	41.82	187.4781	<.0001*
Inflation Pressure(26,35)	1	1	41.5	2.1088	0.1540
Normal Load(1488,1984)	1	1	46.45	1.3353	0.2538
Tire Setup*Slip Ratio Setting	2	2	41.86	65.8784	<.0001*
Tire Setup*Inflation Pressure	1	1	41.56	0.0529	0.8193
Tire Setup*Normal Load	1	1	46.45	0.0002	0.9902
Slip Ratio Setting*Inflation Pressure	2	2	44.5	3.4039	0.0421*
Slip Ratio Setting*Normal Load	2	2	45.34	0.7449	0.4805
Inflation Pressure*Normal Load	1	1	47.18	0.3162	0.5765
Tire Setup*Slip Ratio Setting*Inflation Pressure	2	2	44.52	0.4401	0.6468
Tire Setup*Slip Ratio Setting*Normal Load	2	2	45.3	1.0380	0.3624
Tire Setup*Inflation Pressure*Normal Load	1	1	47.25	0.3733	0.5442
Slip Ratio Setting*Inflation Pressure*Normal Load	2	2	47.36	0.3026	0.7403

The significant variables were investigated further by the use of interaction plots in Figure 7-15 and Figure 7-16. In Statistics, the main effects and interaction plots use connected lines to show the trend of the observations—they do no imply that all of the data will show that trend.

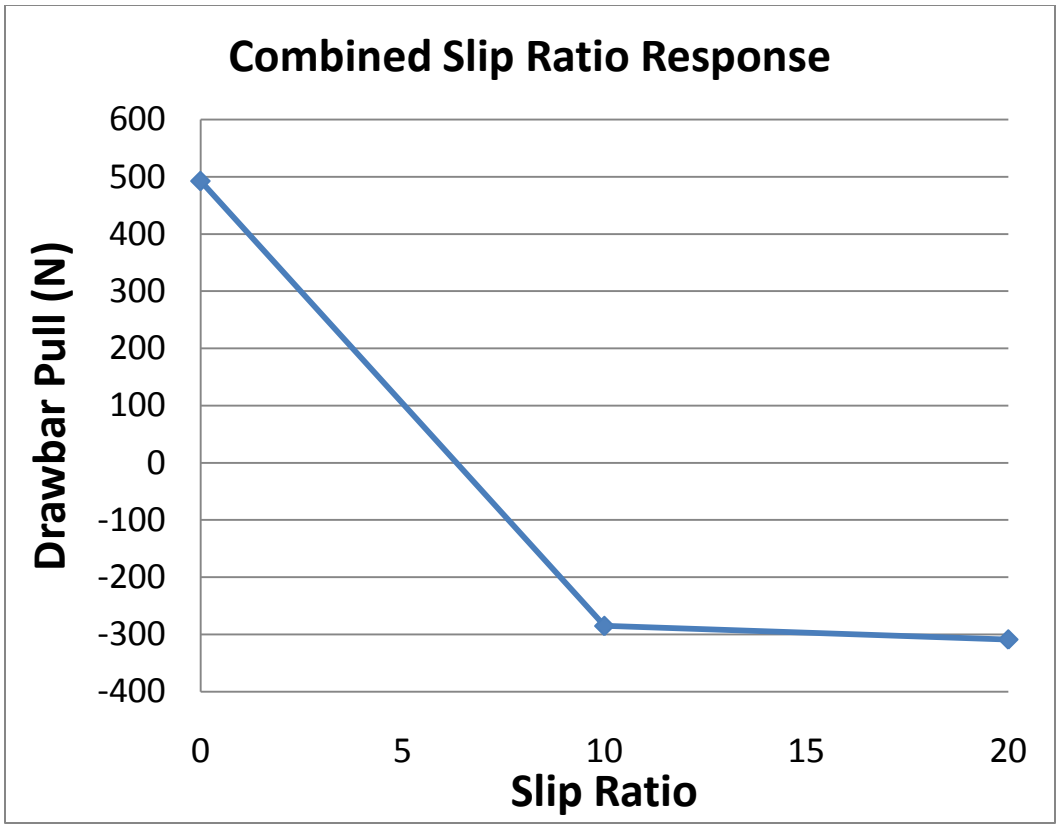

Figure 7-15. Graph of combined slip ratio response. Shows that slip ratio has a significant effect on the response (Fx).

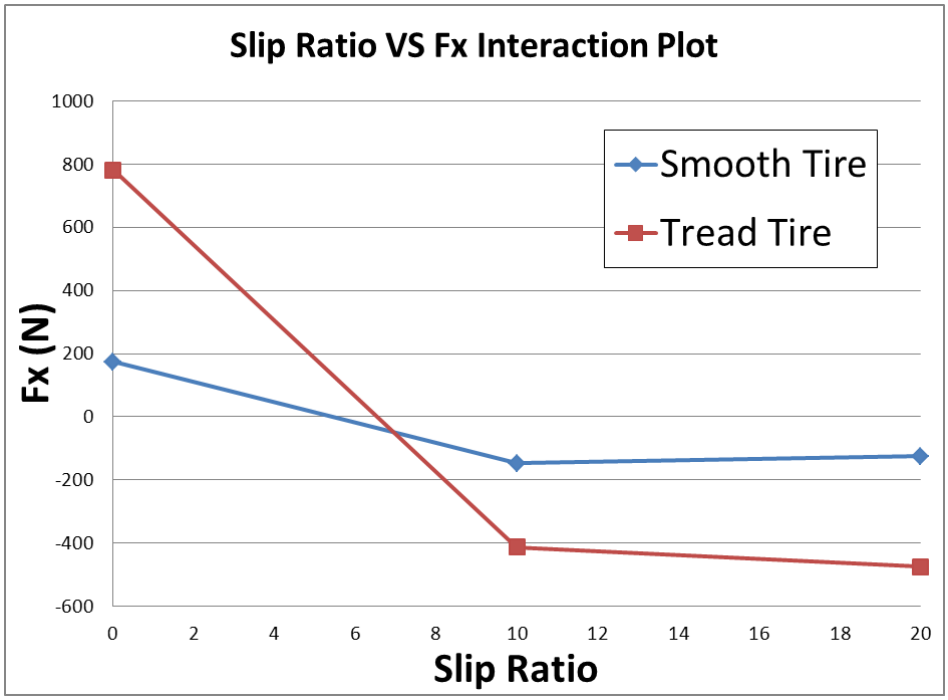

Figure 7-16. Interaction plot of the slip ratio and tire setup. The crossing lines indicate that there is an interaction between both variables.

This data indicates that the analysis could be redone by removing the normal load. This was carried out again by modifying the model and removing the normal load effect and all interactions with the normal load. This created a reduced model that was carried out again in JMP, seen in Figure 7-17. Some of the variables that did not have a significant effect on the response were left in the model because it works in a hierarchical manner—any single factor in a two-factor or three-factor interaction has to remain.

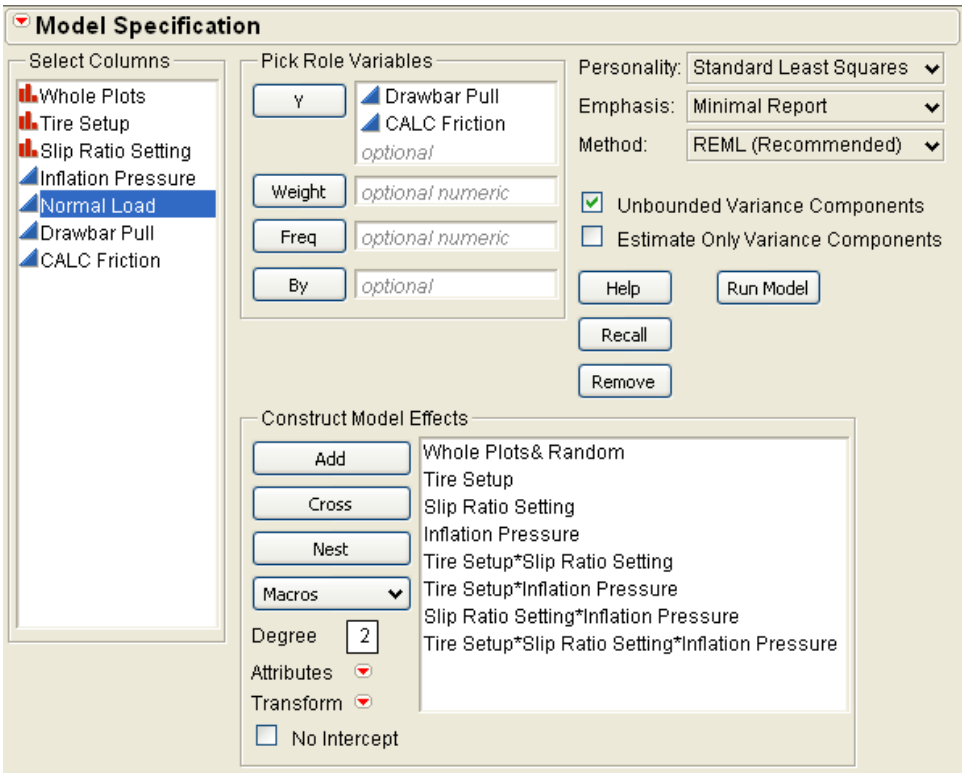

Figure 7-17. The model specification menu in JMP, used to create the model that will analyze the data.

The new model provided new parameter estimates or estimates of the factors that make up the full model of the response (drawbar pull). It also calculated the standard error and the probability of the factor affecting the response. This data can be seen in

Table 7-4 and Table 7-5.

Table 7-4. The parameter estimates for the reduced model.

Summary of Fit

RSquare	0.908331
RSquare Adj	0.89669
Root Mean Square Error	149.8482
Mean of Response	-36.9966
Observations (or Sum Wgts)	72

Parameter Estimates

Term	Estimate	Std Error	DFDen	t Ratio	Prob>|t|
Intercept	-36.99658	21.54242	9.676	-1.72	0.1177
Tire Setup[SMOOTH]	-1.706278	21.54242	9.676	-0.08	0.9385
Slip Ratio Setting[0]	513.94288	25.3175	56.18	20.30	<.0001*
Slip Ratio Setting[10]	-243.5663	25.31685	56.16	-9.62	<.0001*
Inflation Pressure(26,35)	-27.13798	17.8768	55.97	-1.52	0.1346
Tire Setup[SMOOTH]*Slip Ratio Setting[0]	-304.3423	25.31685	56.16	-12.02	<.0001*
Tire Setup[SMOOTH]*Slip Ratio Setting[10]	135.8686	25.3175	56.18	5.37	<.0001*
Slip Ratio Setting[0]*Inflation Pressure	-70.32122	26.376	62.57	-2.67	0.0098*
Slip Ratio Setting[10]*Inflation Pressure	50.39438	25.47513	57.69	1.98	0.0527

Table 7-5. The fixed effect estimates for the reduced model.

Fixed Effect Tests

Source	Nparm	DF	DFDen	F Ratio	Prob > F
Tire Setup	1	1	9.676	0.0063	0.9385
Slip Ratio Setting	2	2	56.19	206.2293	<.0001*
Inflation Pressure(26,35)	1	1	55.97	2.3045	0.1346
Tire Setup*Slip Ratio Setting	2	2	56.19	72.5325	<.0001*
Slip Ratio Setting*Inflation Pressure	2	2	58.76	3.7888	0.0283*

The reduced model confirmed that the slip ratio has a significant response on the force observed in the x-axis. The tire setup combined with the slip ratio setting, and the slip ratio setting versus the inflation pressure were also noted as significant to the response in the x-axis. The DFden is the degrees of freedom for the denominator.

The split-plot design that has been created, has the following statistics model seen in equation (9.2):

$$y_{ijklm} = \mu + \rho_m + \alpha_i + \beta_j + \gamma_j + \tau_k + (\alpha\beta)_{ij} + (\alpha\gamma)_{ik}$$
$$+(\alpha\tau)_{il} + (\beta\gamma)_{jk} + (\beta\tau)_{jl} + (\gamma\tau)_{kl} + (\alpha\beta\gamma)_{ijk} \quad (9.2)$$
$$+(\alpha\beta\tau)_{ijl} + (\alpha\gamma\tau)_{ikl} + (\beta\gamma\tau)_{jkl} + \delta_{ik} + \varepsilon_{ijklm}$$

Where μ is the grand mean, ρ_m is the replication term, $\alpha_i, \beta_j, \gamma_j, \tau_k$ are the first-order means. The interaction terms are $(\alpha\beta)_{ij}$, $(\alpha\gamma)_{ik}$, $(\alpha\tau)_{il}$, $(\beta\gamma)_{jk}$, $(\beta\tau)_{jl}$, $(\gamma\tau)_{kl}$, $(\alpha\beta\gamma)_{ijk}$, $(\alpha\beta\tau)_{ijl}$, $(\alpha\gamma\tau)_{ikl}$, and $(\beta\gamma\tau)_{jkl}$. The whole plot error is δ_{ik}. The subplot error is ε_{ijklm}. For the purposes of this analysis, the error terms were not expanded upon, but the model was simplified by through analysis.

The reduced model has some first, second, and third-order interactions and was essentially the following simplified statistical model in equation (9.3):

$$y = \beta_0 + \beta_0 * tire\ setup + \beta_2 * slip\ ratio + \beta_{12} * slip\ ratio^2$$
$$+\beta_3 * inflation\ pressure + \beta_{12} * tire\ setup * slip\ ratio \quad (9.3)$$
$$+\beta_{122} * tire\ setup * slip\ ratio^2 + \beta_{12} * slip\ ratio * pressure$$

Where the β terms are simply the coefficients for each factor.

Each set of factors in the model has a coefficient, a concept similar to the slope in a linear (line) equation. From the parameter of the reduced model, the inputs are -37 for the intercept, -1.7 for the setup, 514 for the first slip ratio setting, -243 for the second slip ratio setting, and -27

for the pressure. The two-level combinations have the inputs of -304 for the setup and slip ratio level one combination, 136 for the setup and slip ratio level two, -70 for the pressure and slip ratio level one, and 50 for the pressure and slip ratio level two. Equation (9.4) gives the reduced model.

$$\begin{aligned} y = &-37 - 1.7(setup) + 514(s_1) - 243(s_2) - 27(pressure) \\ &- 304(setup)(s_1) + 136(setup)(s_2) \\ &- 70(pressure)(s_1) + 50(pressure)(s_2) \end{aligned} \tag{9.4}$$

The categorical slip value separated the levels of the slip ratio. Where (s_1) is the slip ratio setting at zero and the (s_2) is the slip ratio setting at 10. This model has is conditional where (s_1) is 1 for a slip ratio of zero and 0 otherwise. For (s_2) is 1 for a slip ratio of ten, and the value is 0 otherwise. For different models this means that (s_1) and (s_2) are equal to 0, for slip ratio 20. This created three different equations depending upon the slip ratio, showing the zero slip condition in equation (9.5):

$$\begin{aligned} y = &-37 - 1.7(setup) + 514(s_1) - 27(pressure) - 304(setup)(s_1) \\ &+ 70(pressure)(s_1) \end{aligned} \tag{9.5}$$

Equation (9.6) shows the slip ratio of 10:

$$\begin{aligned} y = &-37 - 1.7(setup) - 243(s_2) - 27(pressure) \\ &+ 136(setup)(s_2) + 50(pressure)(s_2) \end{aligned} \tag{9.6}$$

And a slip ratio of 20 is in equation (9.7) below:

$$y = -37 - 1.7(setup) - 27(pressure) \tag{9.7}$$

The analysis in JMP was able to show which main effects and interactions were statistically significant, or mainly responsible for the changes in the observed drawbar pull and coefficient of friction. For the main effects—the individual variables that were adjusted in the test—the slip ratio was significantly relevant to the drawbar pull response. The second order interaction of the tire setup and slip ratio and the tire setup and inflation pressure were statistically significant. By going through the analysis, a reduced model for the response was created from equation 9.2.

7.4 Results and Discussion of Results: Pressure Pad

The Tekscan I-scan pressure pad software and one MatScan® # 3150 pressure pad were used to record the pressure distribution, mass, size, and the shape of the contact patch of both tires. Screenshots of the readings from the tire with the generic winter tire tread are given below in Figure 7-18 and Figure 7-19. The data was taken at 72 F (22.2 °C) and at an inflation pressure of 35 psi (241.32 kPA).

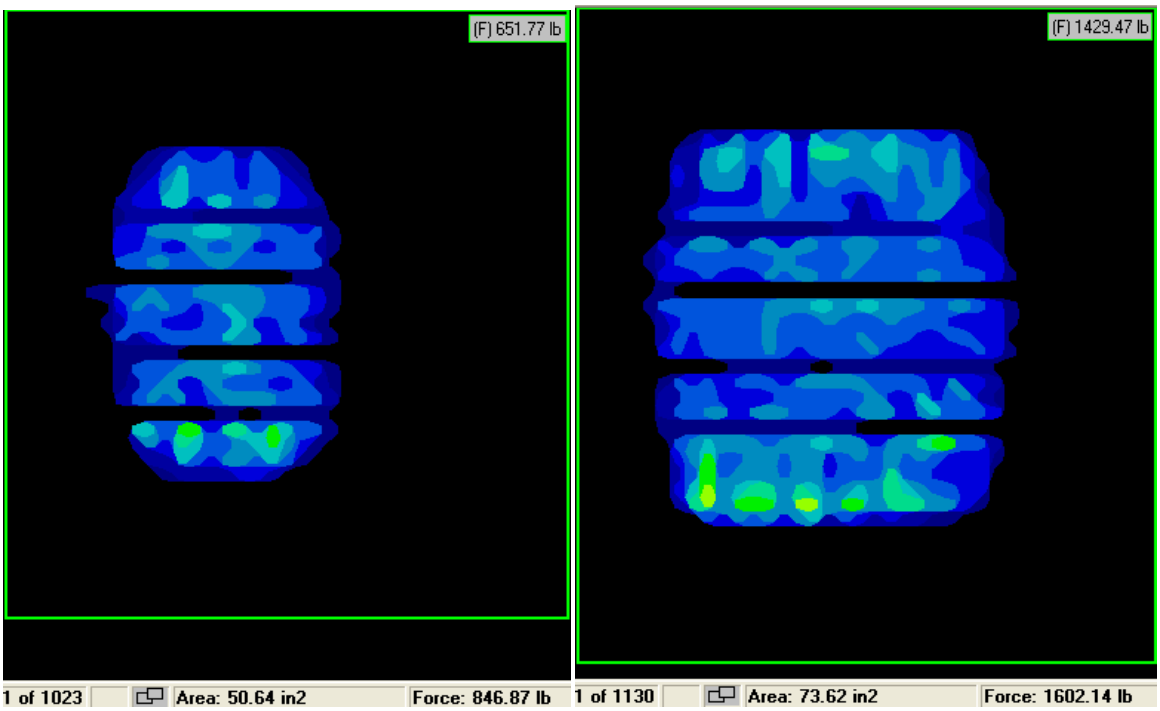

Figure 7-18. Screenshot of the winter tire tread contact patch; left image is for the weight of the carriage; right image is for weight close to 1488 lbf.

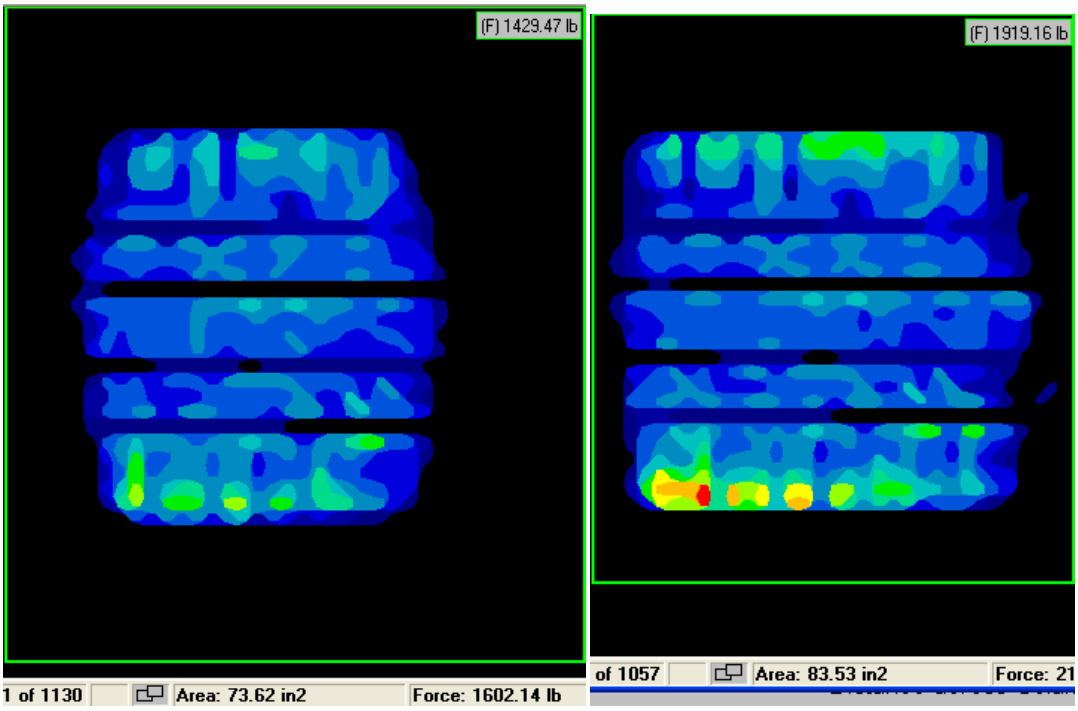

Figure 7-19. Screenshot of the winter tire tread contact patch; left image is for weight close to 1488 lbf; right image is for weight close to 1984 lbf.

On the tire with the winter tire tread pattern, the contact patch area increased with increasing load in the contact patch. With the weight of the vertical shaft portion of the carriage, the pressure pad detected 651.77 lbf (2899.07 N) in the contact patch. The contact patch area was 50.64 square inches (326.71 cm square) and was almost elliptical in shape. This contact patch area increased with increasing load to 73.62 square inches (474.97 cm square) at 1429.47 lbf (6358.28 N) and 83.53 square inches (538.9 cm square) at 1919.16 lbf (8536.42 N). At the lower level of normal loads tested, the shape of the contact patch became fairly rectangular, with the distance from the sidewalls being longer than the longitudinal length of the contact patch. At the higher level of normal loads tested, the shape of the contact patch became practically square-shaped. The width from sidewall to sidewall and the longitudinal length of the contact patch had an almost 1:1 ratio.

The 219% increase of mass in the contact patch (at 1429.47 lbf) resulted in a 145% increase of contact patch area. The 294% increase of mass in the contact patch (at 1919.16 lbf) resulted in a 165% increase of contact patch area. This shows that the increase in normal load reaches a point of diminishing returns, where the increase in contact patch load has a minor effect on the increase in contact patch area. The higher normal force level is at the maximum operating load of the tire, so the size of the contact patch is theoretically at its maximum area.

The bald, or smooth, tire had a contact patch area that increased with increasing load in the contact patch, as seen in Figure 7-20. With the weight of the vertical shaft portion of the carriage, the pressure pad detected 686.14 lbf (3051.95 N) in the contact patch. The shape of the contact patch was almost elliptical. As the normal load increased, the shape became rectangular at the lower normal load then square at the higher normal load level. The contact patch area was much smaller than the tire with the winter tire tread at 39.86 square inches (257.16 cm square) to

50.64 square inches (326.71 cm square) (79% of the winter tire tread contact patch). As weight was added to the contact patch, the normal force in the contact patch increased to 2028.28 lbf (9021.79 N). This increase coincided with an increase in the contact patch area to 84.51 square inches (545.22 cm square).

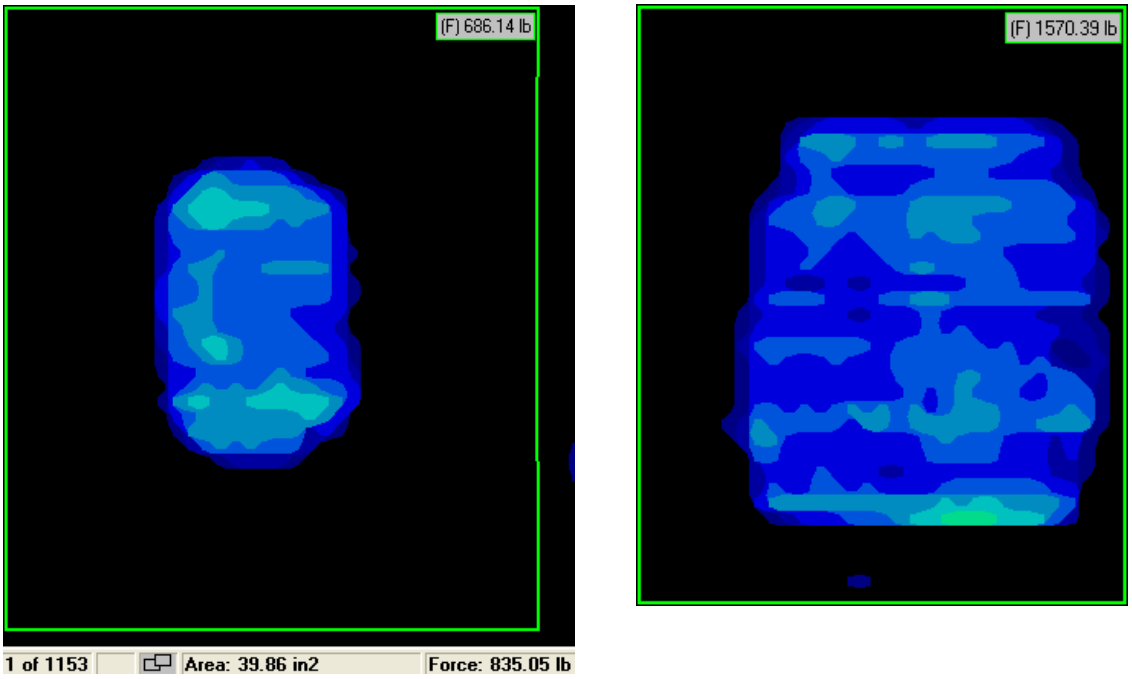

Figure 7-20. Screenshot of the bald (smooth) tire tread contact patch; left image is for the weight of the carriage; right image is for a weight close to 1488 lbf.

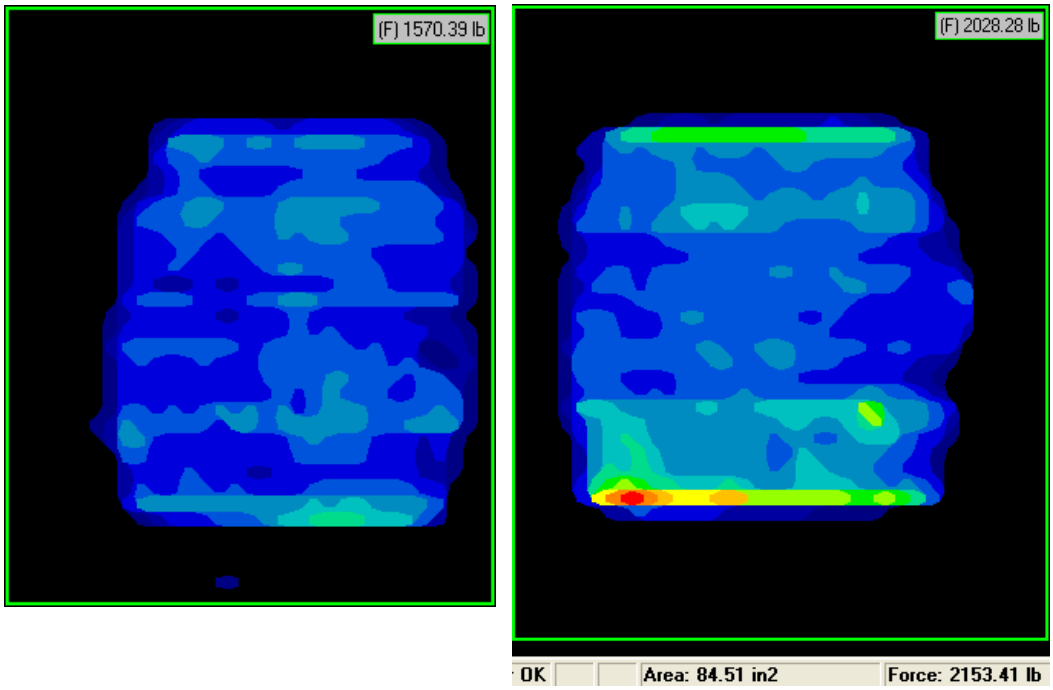

7-21. Screenshot of the bald (smooth) tire tread contact patch; left image is for a weight close to 1488 lbf; right image is for a weight close to 1984 lbf.

The discrepancy between the contact patches of the two tires at the weight of the carriage may have been from a small difference in pressure that was not noted at the time of the recordings. All readings should have been at 35 psi (241.32 kPA). At the higher load of 1984 lbf (8824.83 N), the bald (smooth) tire had an insignificant increase of 101% over the winter tire tread pattern in terms of contact patch area—84.51 square inches to 83.54 square inches (545.22 cm square to 538.9 cm square). The images above show the gaps in the tire tread of the winter tire tread pattern and that the distribution of the pressure in the contact patch is more even on the bald (smooth) tire. The shape of the tire with the generic winter tread was more rectangular than the bald (smooth) tire.

7.5 Results and Discussion of Results: Ice Surface Texture

The generic winter tire tread and the bald (smooth) tire both left patterns on the surface of the ice. The winter tread left an impression on the surface from the grooves and the lugs on the surface. The edges of the tire, seen to the right of Figure 7-22, also caused indents to the surface of the ice for both the tire with the winter tire tread and the bald (smooth) tire. It can be assumed that these indentations are created as the tire melts the ice, but without proper control of the temperatures of the tire or the air above the ice, it may not be valid to conclude that this effect would be seen consistently in winter conditions on ice.

Figure 7-22. Image of the middle of the test surface with the generic winter tire tread pattern that left marks on the surface of the ice. Taken well after a run.

8 Conclusions

This study was intended to identify the impact of different tire parameters on the traction capabilities of pneumatic tires on ice.

An extensive review of literature has been performed to learn about prior studies and experimental set-ups to address this topic. Following our communications with Goodyear, the following parameters were considered: type of tire tread, inflation pressure, normal load on the tire, and slip ratio at the tire-ice contact. A design of experiment has been developed in JMP8 to investigate the influence of these parameters and the correlations between the parameters on the tire traction and friction. Based on the feasibility of performing the tests according to the design suggested by JMP, two levels were selected for the tire tread (smooth and treaded), two levels for the inflation pressure (26 psi and 35 psi), two levels for the normal load (1984 lbf, representing 100% of the load, and 1488 lbf, representing 75% of the normal load), and three slip ratio levels (0, 10, and 20).

The Terramechanics Rig was utilized to carry out tests on ice. This was a novel and unique approach at testing for the drawbar pull and coefficient of friction on ice. Previous studies employed flat sections of the tire tread on rotating trays in closet-sized temperature controlled rooms, or full-scale tests have been performed outdoors because of the difficulty of conducting tests indoors. The terramechanics rig had to be modified to accommodate the study, and it also had to be calibrated to provide a consistent normal load on the tire. Thus, a large portion of the work in this study was dedicated to the preparation of the testing apparatus, including ice creation.

To interpret the test data collected, some strong assumptions were made. The most important one was considering that the resistance force in the tire contact patch is mainly due to the dry friction of the tire on ice. Although we aimed at running the tests to get dry friction, it has been almost impossible to obtain it in the existing testing facility during the summer in Virginia. Thus, the data collected was compared to previous test data and it was found that, in many aspects the trend was similar to previous studies, but in other respects it was not. For example, the behavior of the drawbar pull is consistent with results obtained in prior studies. The general trend of the coefficient of friction at the 35 psi inflation pressure for both loads, is also in-sync with the general trend of older studies presented in the review of literature. The magnitude and the offset of the coefficient of friction did not match previous studies, though, being about one order of magnitude smaller. We postulate that the main reason behind these differences is from the limitations of the testing environment, which did not reproduce the 100% dry friction for which the prior studies presented the results. The tests were conducted at night at an ice bulk temperature of -5 °C and an ambient air temperature of 22.2 °C. It was impossible to consistently get a lower air temperature with the equipment present in the lab. This may have led to the formation of a larger water layer than would be present in an environment that was actually below freezing. Thus, the experimental data collected indicates larger resistance at 20% slip for the lower inflation pressure, compared to 10% slip, but the difference is very small; other studies indicated a slight decrease or an almost steady-state value of the dry coefficient of friction pat 10% slip, which is what we noticed for the higher inflation pressure of 35 psi (nominal inflation pressure for the tires studied). Another possible source of miss-matching could be the effective rolling radius, which had to be pre-computed to provide the rig with the data needed to create a

given slip ratio. A simple sensitivity analysis indicated that a difference of merely a few millimeters greatly affects the sign and value of the calculated coefficient of friction.

Due to the operation of our rig, we forced it to maintain a constant longitudinal speed (the "vehicle speed"), as well as a specific tire slip, by modifying the torque imposed on the tire through the second motor. Due to the presence of the film of water on ice, the phenomena at the tire-ice interface was, in fact, a mixture of dry and wet friction. We postulate that, under pure dry friction conditions, the torque needed would have had larger values, leading to larger values of the coefficient of friction.

From the statistics analysis in JMP we found that the most influential factor is the slip ratio by itself, followed by the combination of slip ratio and inflation pressure, and the slip ratio and tire set-up (both the winter tire tread pattern and the bald tiretreaded or not).

8.1 Conclusions: Suggestions for Further Research

There are several ways to improve and expand upon the research that has been conducted. While the temperatures tested at were consistent, maintaining completely "dry" friction was not physically possible during the summer. Another study could be conducted during the winter, or utilizing some method to control the temperature inside the Terramechanics Enclosure. An example of this would be multiple air conditioning units to lower the temperature above the ice and/or inside the enclosure area.

It was found that the tire setup (bald or winter tread pattern) by itself was not a significant factor in influencing the drawbar pull and the coefficient of rolling friction. Conversely, the combination of the tire setup and the slip ratio did have a significant effect. However, it is clear

that the winter tread pattern has a higher drawbar pull and coefficient of rolling friction. Another series of tests could simply investigate this tire alone at various slip ratios and inflation pressures.

The slip ratio by itself was one of the most important influences on the observed drawbar pull and calculated rolling coefficient of friction. A more dense study at intervals of 1 or 2 between the slip ratios of 0 and 20 should be conducted to observe if the pattern from zero to ten to twenty is consistent.

It was noted that the combination of the slip ratio and the inflation pressure had a significant effect on the observed drawbar pull and calculated coefficient of friction. If it was desired, any additional test scenarios could be paired with more inflation pressures, such as 25% and 50% included with the 75% and 100% that were tested in this study, to see if there is a more noticeable effect from the changes in the inflation pressure.

With a limited amount of time available to collect data, the creation of a mathematical model was not possible in the current study. An extension of this study would be to collect more data to allow for the creation and verification of a model that could predict the coefficient of "wet" friction separate from and along with the average coefficient of friction.

9 References

[1] X. D. Peng, *et al.*, "A New Method for Determining Tire Traction on Ice," in *Proceedings of the Automotive Dynamics & Stability Conferece, May 15 - 17 2000*, Troy, MI, United States, 2000, pp. 1-7.

[2] X. D. Peng, *et al.*, "A Tire Traction Modeling for Use in Ice Mobile," in *Proceedings of the International Congress and Expositiion, Mar 1 - 4 1999*, Detroit, MI, United States, 1999, pp. 1-8.

[3] X.D. Peng, *et al.*, "A New Method for Determining Tire Traction on Ice," presented at the International Congress & Exposition, Detroit, MI, 2000.

[4] S.-K. Chen and W. Lin, "Study of the Test Method to Determine Rubber-Icy Road Friction," *Tribology (Chinese)*, vol. 25, p. 5, May 2005.

[5] S. Shoop, *et al.*, "Three Approaches to Winter Traction Testing Using Instrumented Vehicles," 1994.

[6] K. A. Forland and J.-C. P. Tatinclaux, "Kinetic Coefficient of Ice," U.S. Army Cold Regions Research and Engineering Laboratory, Hanover 85-6, 1985.

[7] K. Nice. (2000, March 10). *How Tires Work.* Available: http://auto.howstuffworks.com/tire.htm

[8] G. F. Hayhoe and C. G. Shapley, "Tire Force Generation on Ice," *SAE Transactions,* vol. 98, pp. 199-207, 1989.

[9] G. F. Hayhoe and C. G. Shapley, "Tire Force Generation on Ice," presented at the International Congress & Exposition, Detroit, MI, 1989.

[10] X.D. Peng and Y. B. Xie, "A Tire Traction Modeling for Use in Ice Mobile," presented at the International Congress & Exposition, Detroit, MI, 1999.

[11] J. Lacombe, "Tire Model for Simulations of Vehicle Motion on High and Low Friction Road Surfaces," in *2000 Winter Simulation Conference*, Orlando, Florida, 2006.

[12] William F. Milliken and D. L. Milliken, *Race Car Vehicle Dynamics* vol. xxviii, 890 p. :. Warrendale, PA :: Society of Automotive Engineers, 1995.

[13] D. A. Anthony, *The Horse, the Wheel, and Language: How Bronze-Age Riders from the Eurasian Steppes Shaped the Modern World.* Princeton: Princeton University Press, 2007.

[14] AccessScience. Hutchinson Dictionary of Scientific Biography [Online]. Available: http://www.accessscience.com/

[15] J. P. Raftery, "Pneumatic Tires and Tubes," O. o. I. o. t. U. S. I. T. Commission, Ed., ed. Washington: Office of Industries of the U.S. International Trade Commission, 1994, pp. 1-12.

[16] R. N. Jazar, *Vehicle Dynamics : Theory and Application* vol. xx, 1015 p. :. New York ; London :: Springer, 2008.

[17] J. C. Dixon, *Tires, Suspension, and Handling*. Warrendale: Society of Automotive Engineers, Inc., 1996.

[18] B. Townsend. (2002, October 14). *Static and Kinetic Friction*. Available: http://ffden-2.phys.uaf.edu/211_fall2002.web.dir/ben_townsend/staticandkineticfriction.htm

[19] Tire Rack. (2010). *P-Metric and Euro-Metric Tire Sizing*. Available: http://www.tirerack.com/tires/tiretech/techpage.jsp?techid=24

[20] The Goodyear Tire & Rubber Company. (2010, March 10). *Tire Size* [Website]. Available: http://www.gnttype.org/techarea/suspension/tired.html

[21] G. Wentz. (2000, May 26). *Tires and Wheels* [Website]. Available: http://www.gnttype.org/techarea/suspension/tired.html
[22] Tire Rack. (2010). *Tire Specs Explained*. Available: http://www.tirerack.com/tires/tiretech/tirespecskey.jsp
[23] Michelin. (2010, May 05). *Radial vs Bias*. Available: http://www.michelinag.com/agx/en-US/products/advantages/bias_radial/bias_radial.jsp
[24] GN/TTyPE Webmaster. (2009, February 10). *Tires and Wheels*. Available: http://www.gnttype.org/techarea/suspension/tired.html
[25] Tire Rack. (2010). *How to Read Speed Rating, Load Index & Service Descriptions*. Available: http://www.tirerack.com/tires/tiretech/techpage.jsp?techid=35
[26] Dunn Tire. (2010, July 1). *Tire Speed Ratings*. Available: http://www.dunntire.com/Learning_Center/Tire_Speed_Ratings
[27] Goodyear. (January 23). *Sidewall Abbreviations* Available: http://www.goodyeartires.com/kyt/readingATire/abbreviations.html
[28] T. Welch. (2006, October 12). *A Tale of Two Tires*. Available: http://www.businessweek.com/autos/content/may2006/bw20060504_512529.htm?chan=autos_classic+cars+index+page_insight
[29] A. W. Savage, "Vehicle Tire," United States of America Patent 1,203,910, 1915.
[30] G. A. Becker. (2000, February 2). *ITEC 2000, International Tire Exhibition and Conference, Announces Its First- Ever Trilogy Awards to Recognize 20th Century's Highest Technological Achievements*. Available: http://www.theautochannel.com/news/press/date/20000914/press025597.html
[31] J. C. Dixon, *Tires, Suspension, and Handling*, 2nd ed. ed. vol. xiii, 621 p. :. Warrendale, PA : London :: Society of Automotive Engineers ; Arnold, 1996.
[32] American Heritage® Dictionary of the English Language. (2009, April 21). *Bias*.
[33] Michelin North America Inc. (2010, January 19). *Radial vs Bias*. Available: http://www.michelinag.com/agx/en-US/products/advantages/bias_radial/bias_radial.jsp
[34] S. T. a. A. Service. (2009, July 19). *Anatomy of a Tire*. Available: http://www.sullivantire.com/trainingcenter/anatomyofatire.aspx
[35] Y. Nakajima, "Analytical Model of Longitudinal Tire Traction in Snow," *Journal of Terramechanics*, vol. 40, pp. 63-82, January 2003.
[36] T. C. Wheels. (2010, July 6). *Types of Tire Construction*. Available: http://www.lwnt.com/glossary-tires.shtml
[37] Rosava. (2010, March 15). *Tyre Design*. Available: http://www.rosava.ua/en/usefull/construction
[38] P. Swami. *OTR Radial Tyres*. Available: http://www.eastmanautotyres.com/otr-technology.html
[39] J. Y. Wong, "Development of High-Mobility Tracked Vehicles for Over Snow Operations," *Journal of Terramechanics*, vol. 46, pp. 141-155, August 2008.
[40] Motor Era. (2008, April 5). *Dictionary of Automotove Terms - "Ti"*. Available: http://www.motorera.com/dictionary/TI.HTM#Tire_Casing
[41] WSDOT. (2003, April 28). *Pavement Testing*. Available: http://www.wsdot.wa.gov/biz/mats/pavement/pave_surfacefriction.htm
[42] Mechanical Forensics Engineering Services LLC. (2007, August 15). *Skidding Friction: A Review of Recent Research*. Available: http://mfes.com/friction.html

[43] G. Ableman. (2004). *Coefficients of Friction for Ice*. Available: http://hypertextbook.com/facts/2004/GennaAbleman.shtml
[44] R. D. Peters. (2002, June 1). *Toward a Universal Model of Damping -- Modified Coulomb Friction (August 7 ed.)*. Available: http://arxiv.org/html/physics/0208025
[45] Rene. (2003, March 11). *Introduction to Tribology – Friction*. Available: http://depts.washington.edu/nanolab/ChemE554/Summaries%20ChemE%20554/Introduction%20Tribology.htm
[46] A. D. Roberts and J. C. Richardson, "Interface Study of Rubber - Ice Friction," *Wear*, vol. 67, pp. 55-69, 1981.
[47] K.-H. Guo, *et al.*, "Study of the Test Method to Determine Rubber-Icy Road Friction," *Mocaxue Xuebao/Tribology*, vol. 25, pp. 234-237, 2005.
[48] Merriam-Webster Incorporated. (2010, March 19). *Ice*. Available: http://www.merriam-webster.com/dictionary/ice
[49] M. C. Potter and C. W. Somerton, *Thermodynamics for Engineers*, Second Edition ed. New York: McGraw-Hill, 2006.
[50] F. P. Bowden and T. P. Hughes, "The Mechanism of Sliding on Ice and Snow," in *Proceedings of the Royal Society of London*, London, 1939, p. 20.
[51] K. A. Forland and J. C. P. Tatinclaux, "Kinetic Friction Coefficient of Ice," United States1985.
[52] K.-i. Shimizu and M. Nihei, "Emergency Braking Test of the Ice and Snow Tires on Iced Drum Tester," 1991.
[53] C. Sandu and J. Biggans, "Building an Infrastructure for Indoor Terramechanics Studies: The Development of a Terramechanics Rig at Virginia Tech.," in *16th International Conference of the International Society for Terrain-Vehicle Systems*, Turin, Italy, 2008.
[54] GlobalSpec. (2010, June 2). *Single Convolute Bellow Air Spring -- YI-1B5-510*. Available: http://www.globalspec.com/SpecSearch/PartSpecs?VID=96992&Comp=2330&PartId={cc44c929-adc4-430d-8a5a-dc38139fbaca}&RegEvent=login
[55] GlobalSpec. (2010, June 20). *Triple Convolute Bellows Air Spring -- YI-3B12-305*. Available: http://www.globalspec.com/SpecSearch/PartSpecs?VID=96992&Comp=2330&PartId={cc44c929-adc4-430d-8a5a-dc38139fbaca}&RegEvent=login
[56] Goodyear, "3B12-304," ed. Akron: The Goodyear Tire & Rubber Company, 2003.
[57] Kistler Holding AG, "Instruction Manual: Measuring Wheel System with Wheel Force Sensor RoaDyn P6xy System 2000," K. H. AG, Ed., ed. Winterthur: Kistler Holding AG, 2008.
[58] A. J. Wheeler and A. R. Ganji, *Introdution to Engineering Experimentation*, Second Edition ed. New Jersey: Pearson Prentice Hall, 2004.
[59] LMS International, "LMS SCADAS: Versatile, High-Performance Data Acquisition Systems," ed. Belgium: LMS International, 2009.
[60] Tekscan. (2009, December 12). *Sensor Map #3150*. Available: http://www.tekscan.com/medical/catalog/3150.html
[61] GlobalSpec. (2010, January 9). *MatScan® - 3150 -- 3150*. Available: http://www.globalspec.com/SpecSearch/PartSpecs?VID=2020&Comp=93&PartId={67154e7b-b4bf-4cbf-ad50-269e479489b0}&RegEvent=login

[62] D. J. S. Plotkin and H. J. Coleman, "Polyvinyl Chloride (PVC)," Nexant Inc., San Francisco2008.
[63] The Goodyear Tire & Rubber Company. (2008, September 7, 2009). Selection of Tires For Light Trucks, Trucks, Busses, Trailers and Multi-Purpose Passenger Vehicles and Definitions of Terms. 14. Available: www.goodyear.com/truck/pdf/edb_loads.pdf
[64] I. A. D. Nesnas and K. Breed. (2007, August 1). *Robot Coordinate Frames and Motion Direction*. Available: http://claraty.jpl.nasa.gov/man/software/development/conventions/coord_frames.php
[65] B. Willis. (2010, Aug 10). *The Traction and Friction*. Available: http://www.worsleyschool.net/science/files/tires/andfriction.html
[66] Kistler, "Messsysteme für die Fahrzeugentwicklung," Kistler, Ed., ed. Ostfildern: Kistler, 2007.

Appendix A: Glossary

Mil: Unit of length that is equal to 0.001 inches or 0.0254 mm (commonly used with plastic sheeting and plastic bags)

Nominal Load: Maximum load of the tire at a specified inflation pressure (35 psi for P-metric tires)

Saturation: Tekscan sensor term that indicates that the sensor has been maxed out. This means that any additional applied pressure will not be registered.

Appendix B: Collected Data

Table B- 1. Table of the test parameters generated by JMP with the data collected.

	Whole Plots	Tire Setup	Slip Ratio	Inflation Pressure	Normal Load (lbf)	Drawbar Pull (N)	Friction
run1	1	TREADED	10	26	1488	-435.38	0.132052617
run2	1	TREADED	0	26	1984	877.49	-0.200218337
run3	1	TREADED	20	35	1488	-513.9	0.153551412
run4	1	TREADED	0	35	1984	1075.9	-0.25273017
run5	1	TREADED	10	35	1488	-378.93	0.118254519
run6	1	TREADED	0	26	1488	882.48	-0.272387955
run7	2	TREADED	20	35	1984	-538.04	0.122916245
run8	2	TREADED	10	35	1488	-72.741	0.027692898
run9	2	TREADED	20	26	1984	-490.54	0.122015625
run10	2	TREADED	10	26	1984	-494.85	0.116563921
run11	2	TREADED	10	35	1984	-448.21	0.100452445
run12	2	TREADED	0	26	1984	1312.4	-0.307351509
run13	3	SMOOTH	20	26	1984	-168.74	0.047239877
run14	3	SMOOTH	0	26	1488	79.04	-0.008788012
run15	3	SMOOTH	10	35	1488	-129.48	0.040774186
run16	3	SMOOTH	10	35	1984	-162.17	0.039615095
run17	3	SMOOTH	20	35	1984	-187.83	0.04728295
run18	3	SMOOTH	20	35	1488	-111.09	0.035295372
run19	4	TREADED	0	26	1488	921.47	-0.284931653
run20	4	TREADED	0	35	1488	679.09	-0.21049599
run21	4	TREADED	10	35	1984	-332.62	0.076260514
run22	4	TREADED	20	35	1984	-523.09	0.122004647
run23	4	TREADED	10	26	1488	-385.78	0.114407593
run24	4	TREADED	20	26	1488	-435.87	0.132285262
run25	5	SMOOTH	20	26	1488	-116.56	0.041322613
run26	5	SMOOTH	10	26	1984	-151.72	0.038265593
run27	5	SMOOTH	20	35	1488	-95.678	0.028721739
run28	5	SMOOTH	0	26	1984	156.13	-0.036334016
run29	5	SMOOTH	0	35	1488	98.99	-0.031995248
run30	5	SMOOTH	10	35	1488	-482.44	0.13848398
run31	6	SMOOTH	0	35	1984	150.9	-0.036586256
run32	6	SMOOTH	10	26	1488	-130.5	0.040309688
run33	6	SMOOTH	0	35	1488	158.75	-0.047978275
run34	6	SMOOTH	10	35	1984	-139.28	0.031240214
run35	6	SMOOTH	10	26	1984	-129.57	0.033380068

run36	6	SMOOTH	20	26	1984	-162.82	0.037582783
run37	7	SMOOTH	10	35	1488	-137.02	0.042773828
run38	7	SMOOTH	20	26	1488	-110.5	0.033641227
run39	7	SMOOTH	0	26	1984	150	-0.03489305
run40	7	SMOOTH	10	26	1984	-223.57	0.0561822
run41	7	SMOOTH	20	35	1984	-102.08	0.02741865
run42	7	SMOOTH	0	35	1984	-341.12	0.078167344
run43	8	TREADED	10	35	1488	-404.38	0.118821483
run44	8	TREADED	10	26	1984	-502.74	0.116709858
run45	8	TREADED	0	35	1984	198.56	-0.044824234
run46	8	TREADED	20	26	1488	-382.9	0.123881542
run47	8	TREADED	20	35	1488	-454.69	0.137137742
run48	8	TREADED	0	26	1488	573	-0.176632344
run49	9	SMOOTH	0	35	1488	147.95	-0.043621935
run50	9	SMOOTH	0	26	1488	623.58	-0.192477982
run51	9	SMOOTH	20	26	1984	-184.37	0.049494095
run52	9	SMOOTH	20	35	1984	-184.52	0.046981669
run53	9	SMOOTH	10	26	1488	-95.965	0.033805989
run54	9	SMOOTH	0	26	1984	362.05	-0.078771675
run55	10	SMOOTH	0	26	1488	134.71	-0.0396354
run56	10	SMOOTH	20	35	1488	-152.27	0.047853148
run57	10	SMOOTH	10	35	1984	-164.68	0.039858669
run58	10	SMOOTH	0	35	1984	372.58	-0.087167738
run59	10	SMOOTH	10	26	1488	-140.86	0.046877007
run60	10	SMOOTH	20	26	1488	-136.49	0.049009296
run61	11	TREADED	0	35	1488	930.68	-0.290125478
run62	11	TREADED	20	26	1984	-478.86	0.115500164
run63	11	TREADED	20	35	1984	-490.3	0.111474052
run64	11	TREADED	0	26	1984	882.57	-0.203292151
run65	11	TREADED	10	35	1984	-536.81	0.125038287
run66	11	TREADED	20	35	1488	-414.51	0.125216146
run67	12	TREADED	10	26	1984	-558.53	0.130762839
run68	12	TREADED	10	26	1488	-403.38	0.122358213
run69	12	TREADED	0	35	1984	641.08	-0.148853476
run70	12	TREADED	20	26	1984	-542.55	0.128180023
run71	12	TREADED	0	35	1488	411.12	-0.129193681
run72	12	TREADED	20	26	1488	-436.69	0.132796876

Appendix C: Example of PiCPro Ladder Code used in tests

The code illustrated in Figures C-1, C-2, C-3, and C-4 is one program used to move the Terramechanics Rig at 7.4 cm/s and rotate the tire for a calculated slip of 20 slip at a load of 1488 lbf. In this example the code is moving the rig in the direction towards the office. READ_SV is code that initializes the motor in the specified axis. ACC_DEC specifies the rate of acceleration and deceleration in the motor for the specified axis. VEL_STRT is used to input a rate of velocity that the specified axis motor will achieve using the acceleration or deceleration values specified in ACC_DEC.

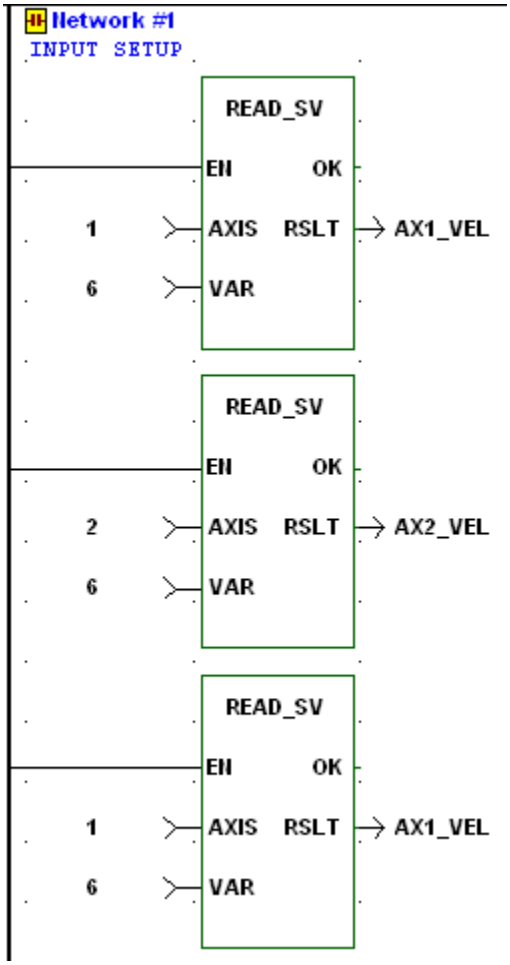

Figure C- 1. Example of the first portion of the code used to initialize the rig and the acceleration rates.

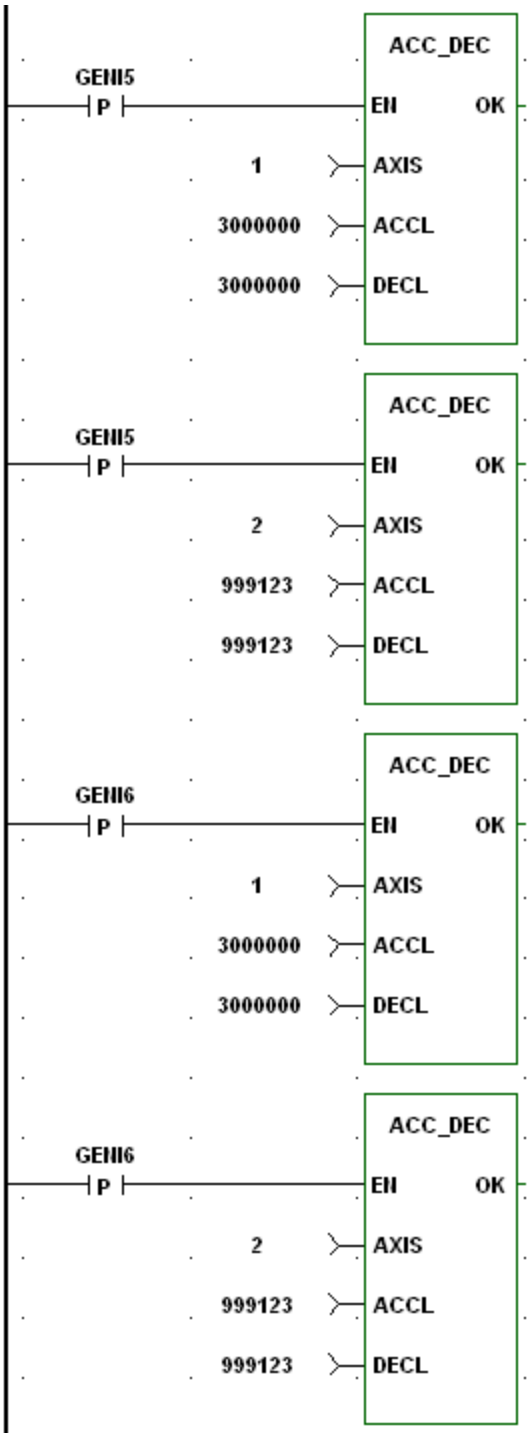

Figure C- 2. Example of the second portion of the code used to initialize the rig and the acceleration rates.

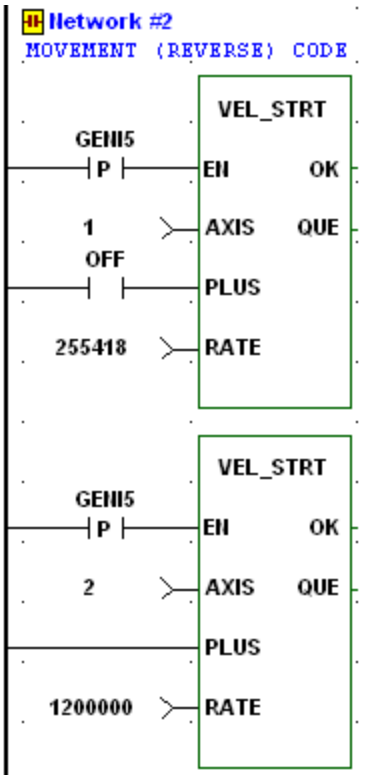

Figure C- 3. Example of the code used to start movement of the rig in the "reverse" direction towards the offices.

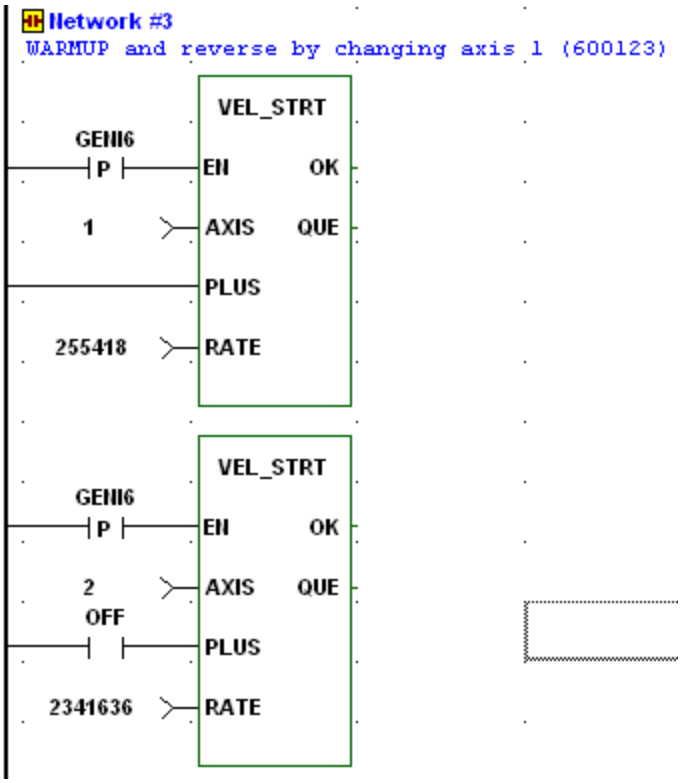

Figure C- 4. Example of the code used to start movement of the rig in the "forward" direction towards the computer station. To spin the wheel in place, axis one would be set to a rate of zero and axis two could be set to 12,000,000 LU/min or 120 degrees/sec.

The ladder code is uses objects such as VEL_STRT in green—which starts movement at the specified velocity—to control the movement of the Terramechanics Rig. These boxes are literally connected to a sort of power rail on the left side of the interface in PiCPro. GENI5 refers to the bottom right button on the Rig controller, and GENI6 refers to the bottom left button on the Rig controller.

Appendix D: Removing Condensation and Melting the Ice

Despite the insulation underneath the ice surface, it continually created condensation on the underside of the C-channels. This water collected in the bottom of the rig and had to be removed daily via vacuum. To ensure that this water would not spread everywhere around the lab, a six-foot 2-by-4 was trimmed down to block the door opening of the Terramechanics Rig enclosure. This ensured that up to 1 inch of water could be contained inside the Rig itself, as the rear drain supported up to an inch of water before it would overflow.

To remove the water that collects in the bottom of the rig:

1) Prep vacuum inside Terramechanics Rig enclosure
2) Put the hose as close to the ground of the rig as possible (the hose tends to bend upwards)
3) Start the vacuum inside the enclosure
4) Wait until the vacuum comes close to being full (the sound of the motor will change slightly as the vacuum reaches capacity)
5) Remove the lid and place it in a place where water can leak out of the lid and get collected
6) Use the utility pump to remove this water from the vacuum canister to a suitable location outside

Appendix E: Revised Kistler Hub Instruction Manual

Terramechanics Rig Startup Manual

1. **<u>Turn on the electronics for 20 minutes or more</u>**

1.1. The LMS SCADAS III data acquisition system (DAQ) should be turned on first. Its switch is located in the back of the unit, just above the power cord (left facing the channel inputs or right if facing the back panel), seen in Figure E-1.

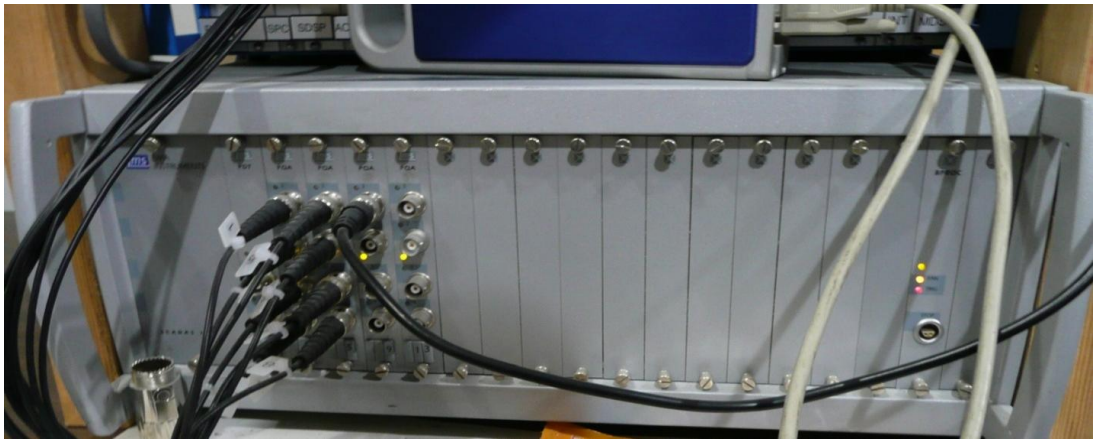

Figure E- 1. Front view of the LMS SCADAS III front-end for LMS Test.Lab.

1.2. The power supply for the Kistler System 2000 front-end should be turned on second. This unit has a red power switch that will glow red when the unit has power.

1.3. The laptop containing the Remote Emulator should be started.

1.3.1. If the computer was turned off (not in hibernation) then it should boot up and load the Remote automatically.

1.4. Load the Remote Emulator if this has not been completed; it should be loaded up on the laptop.

1.5. Turn on the Kistler front-end by hitting the green button on the right of the front panel, as shown in . The button should glow green.

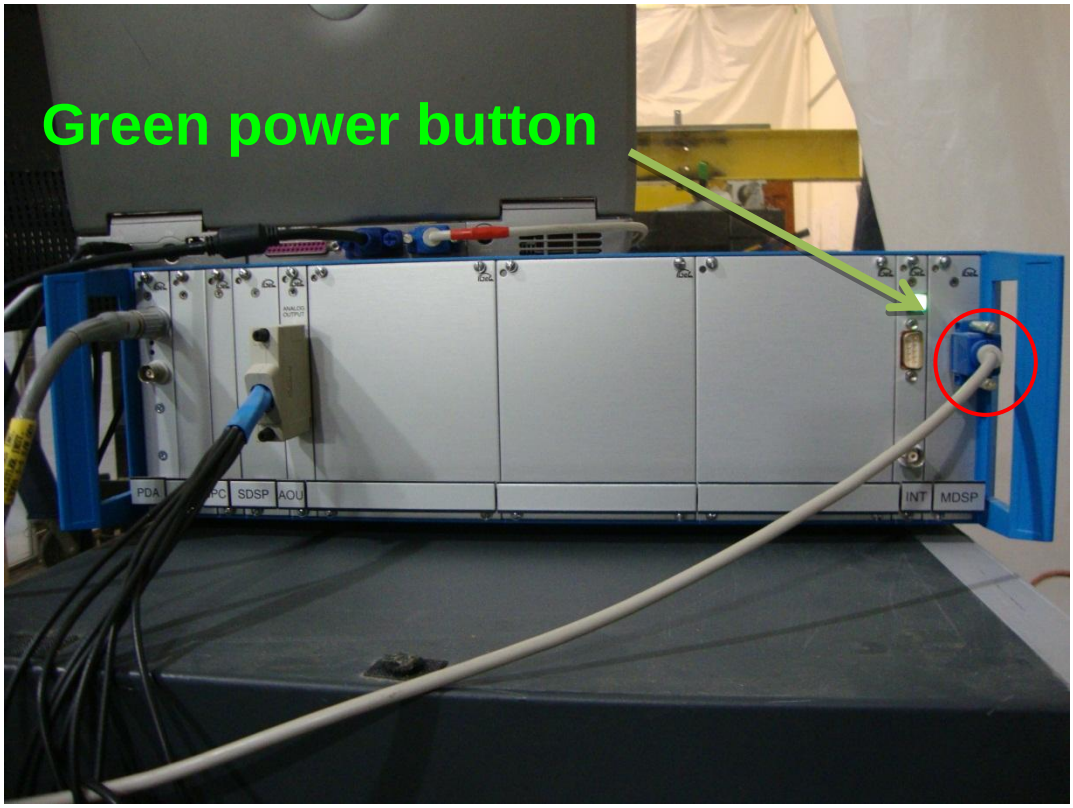

Figure E- 2. Front view of System 2000 interface of the Kistler Wheel Force Sensor with the power turned on, circled in red.

2. **Warm-up the components of the sensor**

   2.1. Load up a program in PiCPro that will spin the wheel in place.

   2.2. Start this program and allow it to run for 15-20 minutes.

   2.3. Check the temperature during the last few minutes of the run to determine if the temperature is staying consistent.

3. **Turn on the Terramechanics Rig computer.**

   3.1. The computer should be off before turning on the rest of the equipment, as the LMS data acquisition unit, sometimes, does not respond when the computer is already on.

4. **Turn on the Terramechanics Rig hardware.**

   4.1. Turn on breaker 15 of the 480 V panel (see Figure E-3, left)

   4.2. Turn on breaker 18 of the 120 V panel (see Figure E-3, right)

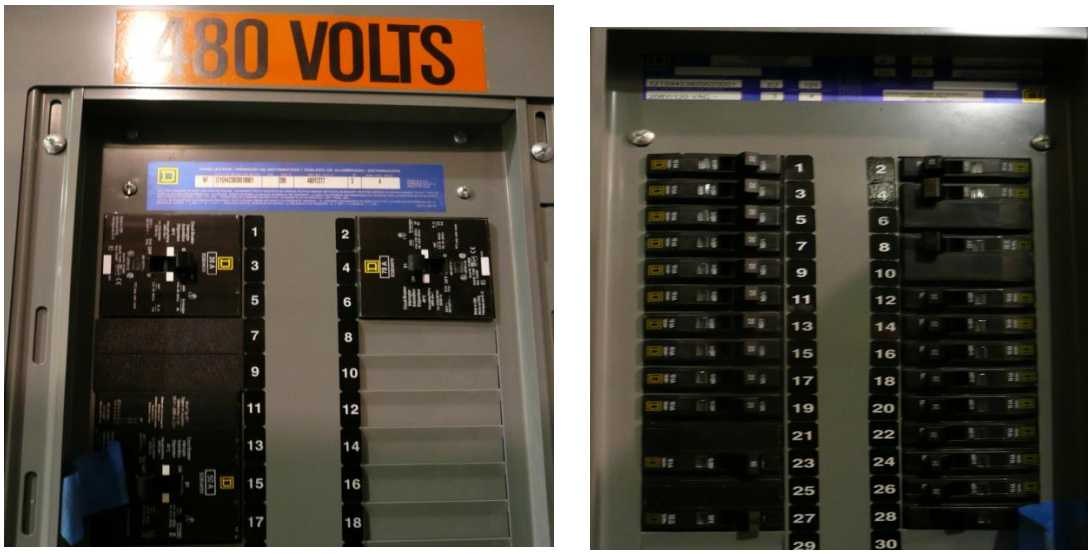

Figure E- 3. Panel LVP-1 supplies 120 Volts to power the motors. Breaker 18 must be flipped on to supply the voltage

5. Check the system settings

5.1. Load LMS Test.Lab on the desktop computer.

5.1.1. This can be found on the desktop or start menu.

5.1.2. Specifically use the "Signature Testing – Advanced" link to start the full data acquisition program, seen in Figure E-4.

Figure E- 4. The link to the LMS Test.Lab program.

The project loaded in LMS Test.Lab is shown in Figure E-5.

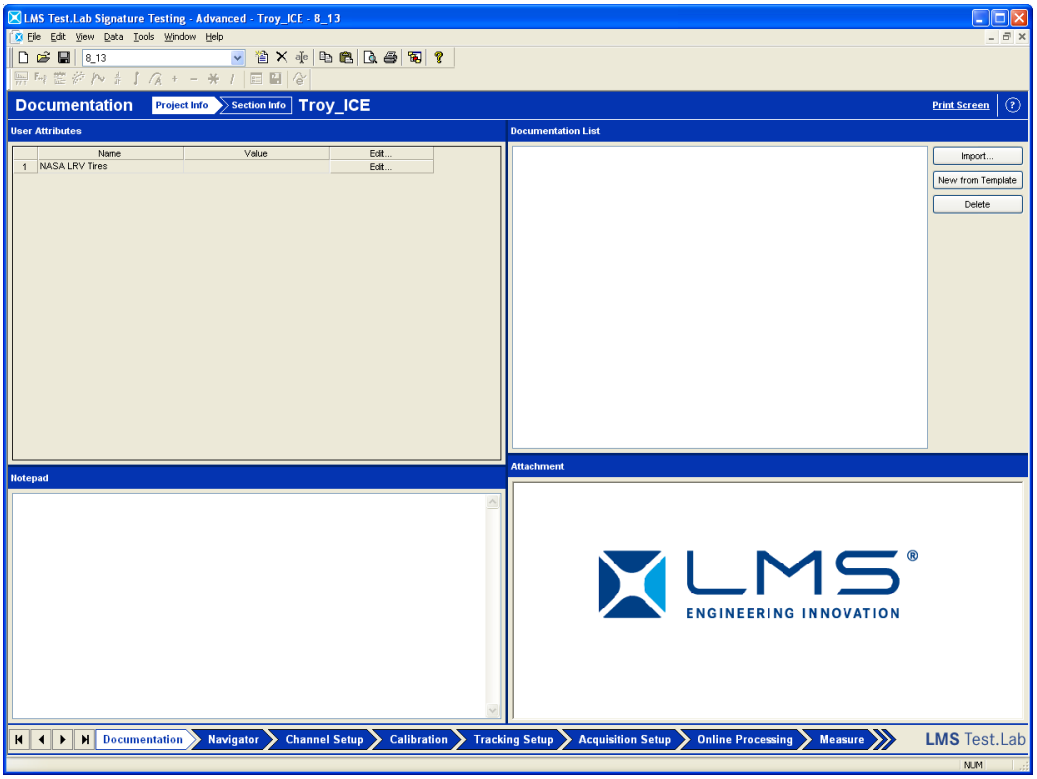

Figure E- 5. Project loaded in LMS Test.Lab. Bottom of the screen shows tabs for different functions.

5.2. With LMS Test.Lab loaded, go to the analog scale in the RoaDyn Remote Emulator through its setup.

5.2.1. "Output Setup"

5.2.2. "Analog Output Scale" can be seen in Figure E-6

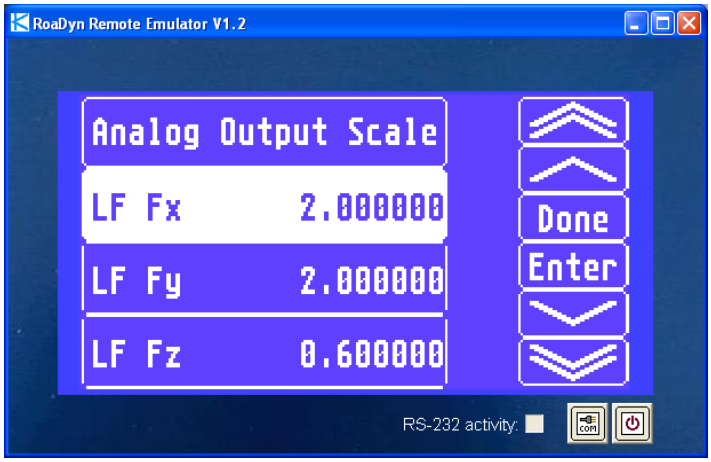

Figure E- 6. Screenshot of the "Analog Output Scale" screen.

5.3. Confirm that these values match with the values in LMS under the "Channel Setup" tab.

6. Before each run

6.1. Spin the wheel at 120 degrees per second or another prescribed wheel speed, Figure E-7.

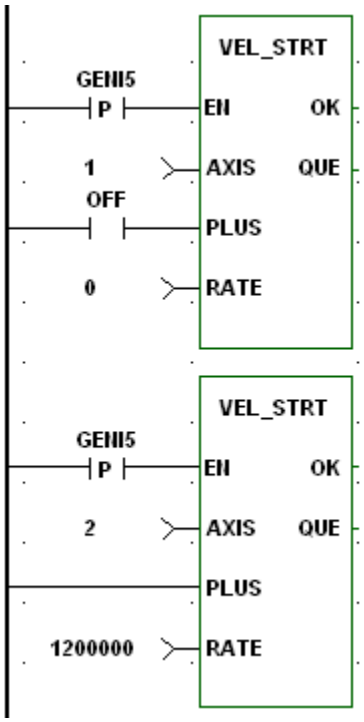

Figure E- 7. Example of the VEL_STRT portion of the code used to perform a warm up.

6.2. Perform a signal offset.

6.2.1. From the main screen on the RoaDyn Remote Emulator V1.2 select “Setup”

6.2.2. Select “Offset” and then “Signal Offset”

6.2.3. In the Signal Offset menu, select “Clear All”

6.2.4. This will bring you to the “Setup” screen again.

6.2.5. Select “Offset” and then “Signal Offset”

6.2.6. In the Signal Offset menu, select “Left Front” to do a signal offset on the Kistler hub attached to the Remote Emulator

6.2.7. In the “Setup” menu click exit to see the main screen, “Wheel Loads,” seen in Figure E-8.

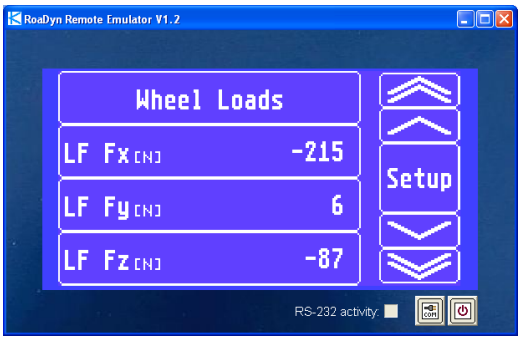

Figure E- 8. Screenshot of the "Wheel Loads" screen.

7. Powering Down the Kistler System.

7.1. Return the rig to the starting position you prefer or position it near the office

7.1.1. Positioning it at the very end of the container near the office will help to initialize the starting position if you need to run a position-specific program

7.2. Turn off the Kistler system.

7.2.1. Push the glowing green button on the System 2000 unit

7.2.1.1. Make sure this button is no longer active (glowing).

7.2.2. Wait 15-20 seconds and turn off the external power supply to the unit.

8. Save the Data.

8.1. Before doing anything else save the data in LMS Test.Lab through the file menu or the save icon on the toolbar menu.

8.2. Close the LMS Test.Lab program.

8.3. Close the PiCPro program and save any changes you have made if needed.

8.3.1. If you don't want to save any changes, select "no" during the prompt to discard these changes.

8.4. Turn off the computer, if you are completely finished using it.

9. Turn off the Power to the Motors and Controllers.

9.1. Turn off the keyed safety switch by rotating it counterclockwise until the light no longer glows.

9.2. Turn off the breaker switches that were turned on earlier, breaker 15 on HVP-1 and breaker 18 on LVP-1.

Appendix F: Kistler P650TT WFS versus S635 WFS comparison

Kent Lassen, Vehicle Applications Manager, and Aaron Schumacher, Technical Manager, from Kistler visited the Center for Vehicle Systems and Safety (CVeSS) in July to help troubleshoot the Advanced Vehicle Dynamics Lab's (AVDL's) Terramechanics Rig sensor and do a comparison of the Terramechanics Rig's Kistler sensor versus their own Wheel Force Sensor (WFS). Our first step was to observe the readings from the Terramechanics Rig's sensor on the ice test surface with its current settings. This was completed using the bald (smooth) tire and the current figuration that had the bolts torqued to 65 ft-lbs. Several different scenarios were explored and recorded with LMS Test.Lab.

Afterwards, the adapter plate on the hub was removed, a new angle offset was completed, and the adapter plate was replaced. A few sets of data were collected again to see if there was any change in the observations. The angle offset did improve the response to a small degree but the data still appeared to vary significantly. The Fz value oscillated around 1500 N plus 200 N for the sensor for an estimated load of 382 lbf, as seen in Figure F-1. The Fx values for the same test are presented in Figure F-2.

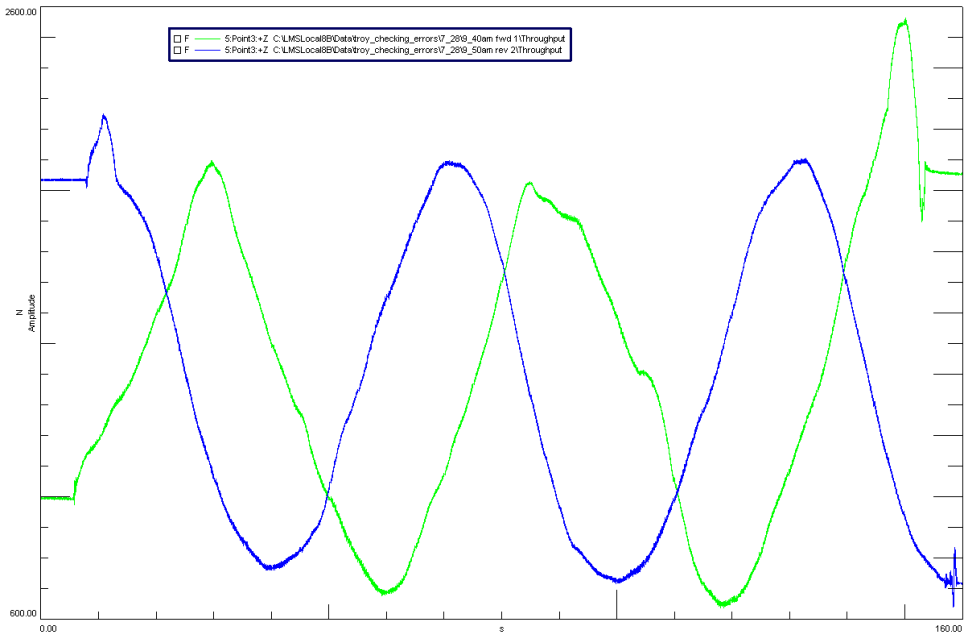

Figure F- 1. Z-value readings taken in the morning before the angle offset was performed again. The tire is moving in reverse. Load approximately 382 lbf.

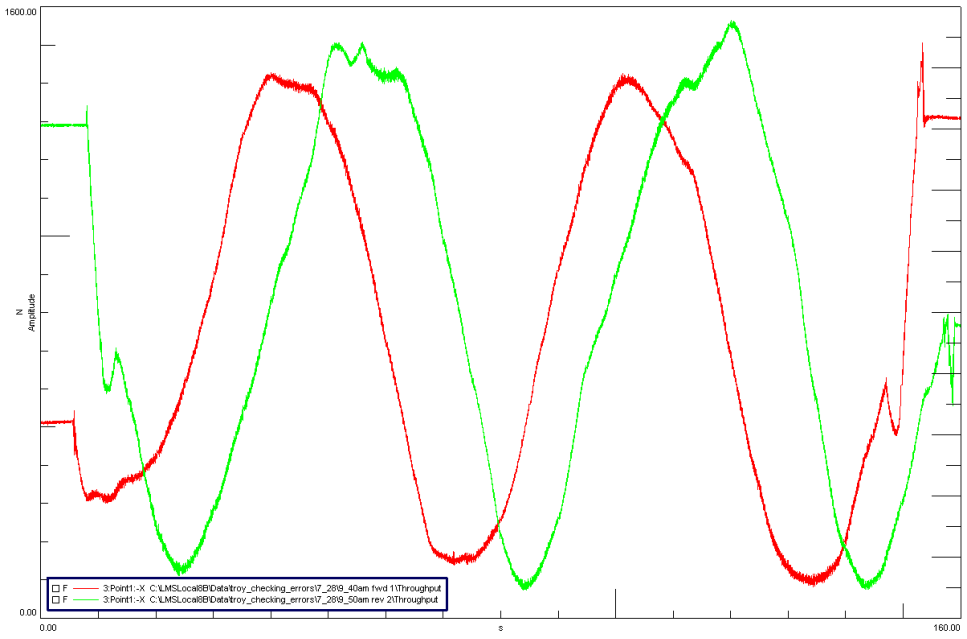

Figure F- 2. X-value readings taken in the morning before the angle offset was performed again. The tire is moving in reverse.

Afterwards, the adapter plate on the hub was removed, the angle offset was completed, and the adapter was put back on. A few sets of data were collected again to see if there was any change in the observations. The angle offset did improve the response to a small degree but the data still appeared to vary significantly. The observed load was 1300 N plus 200 N of the sensor for an estimated load of 337 lbf, as seen in Figure F-3. The Fx data is presented in Figure F-4.

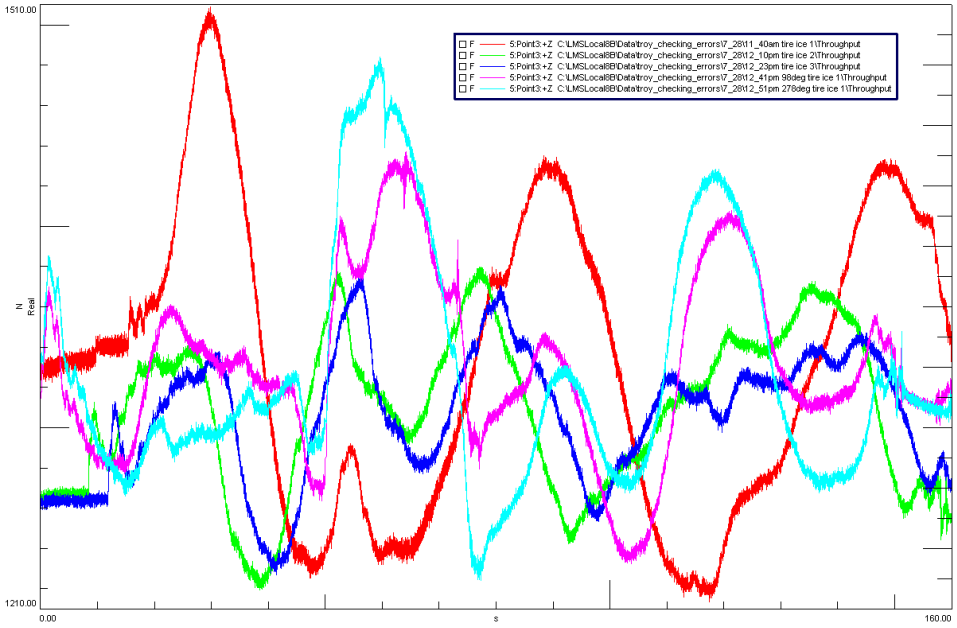

Figure F- 3. Z-value readings taken around noon after the angle offset was performed. The tire is moving in reverse. The hump in the data comes from a board placed on the ice surface. Load approximately 337 lbf.

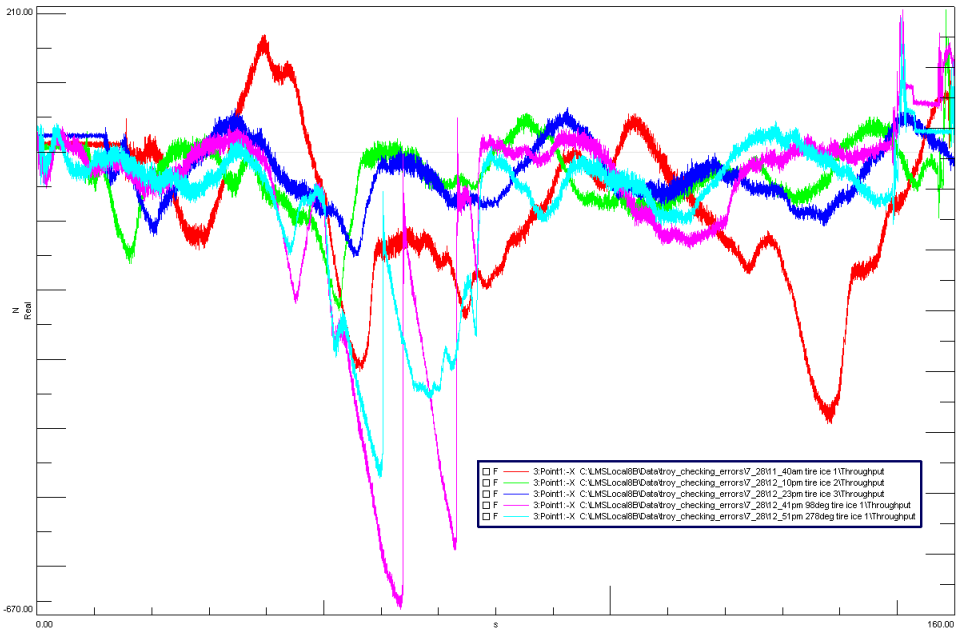

Figure F- 4. X-value readings taken around noon after the angle offset was performed. The tire is moving in reverse. The valley in the data comes from a board placed on the ice surface.

The Terramechanics Rig utilized a Kistler P650 TT WFS. This sensor hub was mounted to a Jeep hub so that any tire could be tested on the system as long as it had a viable 5-point rim. The sensor Kistler brought was a Kistler S635 WFS with a hub sensor that was already embedded into a rim-like assembly with an adapter rim to fit the 17-inch diameter wheels of Kistler's Jeep. Both sensors used a System 2000 front-end while the Terramechanics Rig's system was based on piezoelectric technology and the Kistler's own sensor was based on strain gauge technology, and used quartz sensors that could keep their calibration data (including the signal offset) for a far greater amount of time than the piezoelectric sensor mounted to the Rig [66].

It was decided that the Terramechanics Rig sensor should be compared to the sensor that Kent and Aaron brought. This sensor was already imbedded in a rim with a tire mounted to it, but it had a different size bolt pattern and required an adapter to attach to the Rig's adapter plate. This adapter was installed along with another stator for this sensor utilizing a stator adjusting device. Afterwards the wheel/tire assembly was mounted to the Terramechanics Rig sensor. Kistler provided their own front-end, remote, and cabling to attach the sensor to the AVDL's LMS SCADAS. The final piece to attach to this wheel/tire assembly was a hub electronics cover that contained the circuitry that interpreted the readings from the sensor; it was discovered that the first hub electronics cover did not work so another matching cover was utilized.

The second set of readings was taken during the night after both sensors were checked and calibrated. The angle offset of the Terramechanics' sensor was already completed earlier and verified, so the angle offset of the S635 sensor was performed. Before taking any readings the signal offset was performed on the S635 sensor and the P650 sensor while the Rig motor turned both sensors at 120 degrees per second. The channel setup had not been finalized but some readings were taken during this time. The Fz values found during these tests were around 2800 N plus 400 N for an estimated load of 719 lbf, as seen in Figure F-5.

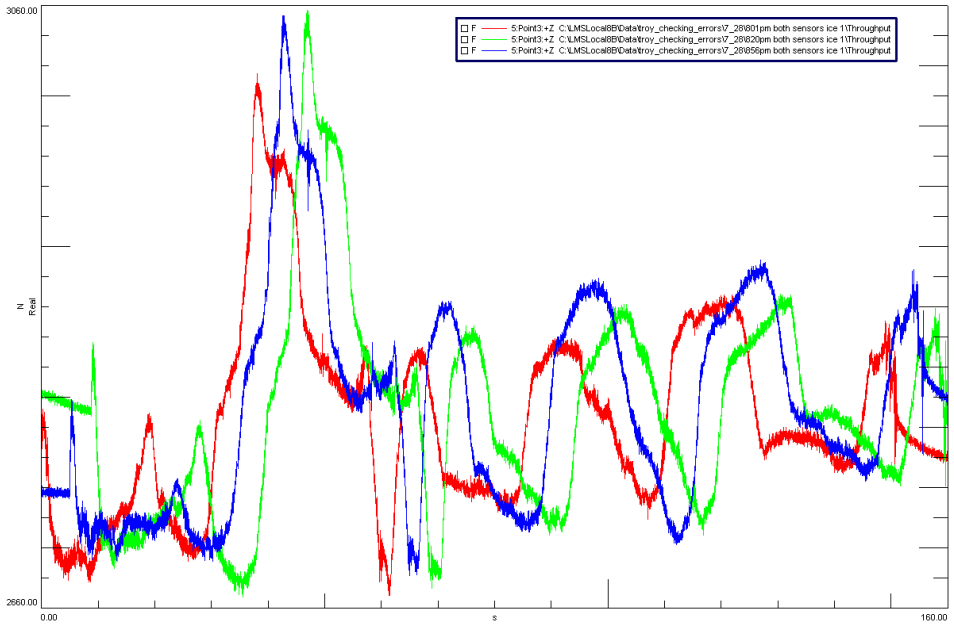

Figure F- 5. Z-value readings taken in the evening after angle offset and signal offsets performed. The tire is moving in reverse. Load approximately 719 lbf.

After all of the channels were setup properly, the readings for both sensors was taken again, as seen in Figure F-6. The Terramechanics Rig sensor recorded approximately 475+ newtons when the tire was suspended in the air because of the weight of the tire, rim, adapter, the WFS top plate, half of the load cells, and the added load of the S635 sensor. The S635 WFS recorded approximately 250+ newtons when the tire was suspended in the air because the sensor read the weight of the tire, rim, adapter, the WFS top plate, and half of the load cells. Based on these readings taken around 10 PM, both sensors averaged 3250 N for an estimated load of 731 lbf.

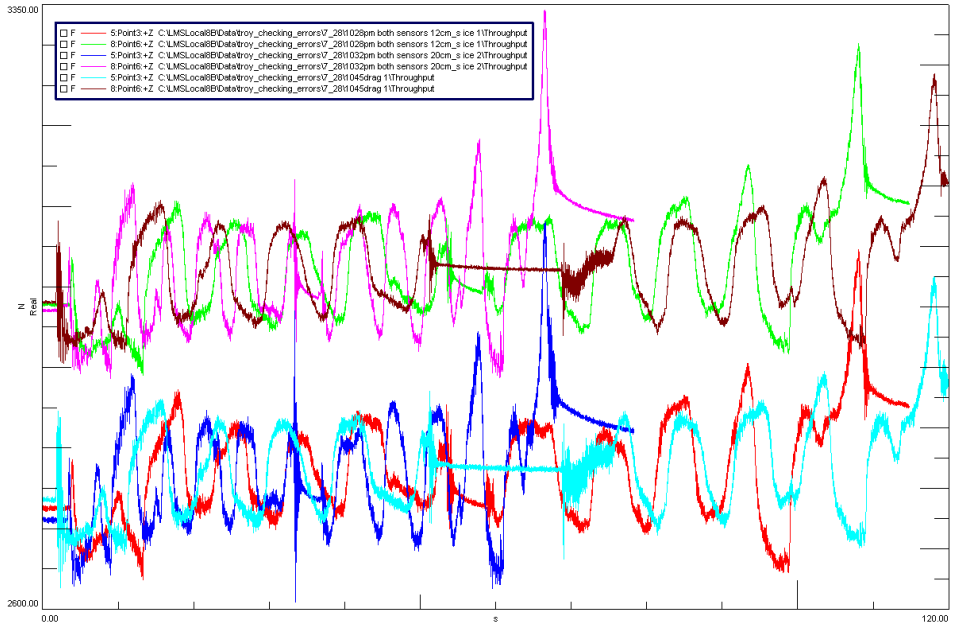

Figure F- 6. Z-value readings taken in the evening after the channel setup was corrected. The top value corresponds to the S635 sensor that was furthest from the Terramechanics Rig motor. The tire is moving in reverse. Load approximately 731 lbf.

After several different test scenarios, it was concluded that both sensors provided approximately the same readings. It was not observed until afterwards that there was an issue with the Terramechanics Rig sensor reading nearly half of the actual load. This problem was investigated thoroughly, ruling out the sensor and the front-end. It appears that the length of the bolts was an important factor, although the bolts did not appear to be touching the stop-plate imbedded in the adapter. Replacing the bolts with shorter bolts that should not be touching the stop-plate appears to have alleviated the problem of reading the incorrect loads.

Appendix G: Matlab Code to Filter the Data

```
% Troy Holley
% LMS_DataReaderTroy program

% Set the values for the beginning of the Z-axis based on the time position
T1=1000;
T2=8000;
% loop goes through the 72 runs
 for i=1:72
    zthelength=0;        %clear the length of the variable

    zstring_iteration=num2str(i)   %output to check the iteration <<WORKS>>
    xstring_iteration=num2str(i)   %output to check the iteration
    sstring_iteration=num2str(i)   %output to check the iteration
    tstring_iteration=num2str(i)   %output to check the iteration

    zloadthis=strcat('zdata',zstring_iteration,'.txt')    % file name changes per iteration
<<WORKS>>
    xloadthis=strcat('xdata',zstring_iteration,'.txt')    % file name changes per iteration
<<WORKS>>
    sloadthis=strcat('sdata',zstring_iteration,'.txt')    % file name changes per iteration
<<WORKS>>
    tloadthis=strcat('tdata',zstring_iteration,'.txt')    % file name changes per iteration
<<WORKS>>

    [ztextportion, znumbers] = hdrload(zloadthis);      %string variables used to load file names
    [xtextportion, xnumbers] = hdrload(xloadthis);
    [stextportion, snumbers] = hdrload(sloadthis);
    [ttextportion, tnumbers] = hdrload(tloadthis);
    ztime = znumbers((T1:T2),1);   %  copy first column of EXAMPLEONE into time
```

```
z_data = znumbers((T1:T2),2);   %  and second column into z

%xtime = xcurrentfile(:,1);   %  copy first column of EXAMPLEONE into time

x_data = xnumbers((T1:T2),2);   %  and second column into z

%stime = scurrentfile(:,1);   %  copy first column of EXAMPLEONE into time

s_data = snumbers((T1:T2),2);   %  and second column into s (THE SPEED)

t_data = tnumbers((T1:T2),2);


%zthelength = length(ztime)      %determine the amount of variables in the vector time
(matches z_data)

zthelength=length(z_data)


zaverage_counter=0;

zaverage_sum=0;

xaverage_counter=0;

xaverage_sum=0;

saverage_counter=0;

saverage_sum=0;

taverage_counter=0;

taverage_sum=0;


%% FILTER using the example from Michael Craft


Ny=80; %rad/sec- Nyquist freq(=Fs/2) or half the sampling frequency of the digital signal

wn=6;  %cutoff freq of the filter

ncf=wn/Ny;  %Normalized Cutoff Freq

n=4; %order of the filter

[num,den] = butter(n,ncf);      %Butterworth filter gives minimal ripples in the signal


%Zfilter = [];                  %Clear the data first
```

```
%Xfilter = [];              %Clear the data first
%Sfilter = [];              %Clear the data first
%Tfilter = [];              %Clear the data first

%Function to filter the array data
z_filterdata   = filtfilt(num,den,z_data);    %the filtered data
x_filterdata   = filtfilt(num,den,x_data);    %the filtered data
s_filterdata   = filtfilt(num,den,s_data);    %the filtered data
t_filterdata   = filtfilt(num,den,t_data);    %the filtered data

%%% WRONG ???
%z_filterdata   = filtfilt(num,den,z_data(T1:T2,1));    %the filtered data
%x_filterdata   = filtfilt(num,den,x_data(T1:T2,1));    %the filtered data
%s_filterdata   = filtfilt(num,den,s_data(T1:T2,1));    %the filtered data

for g = 1:zthelength
   if z_data(g) > 6115.2 && z_data(g) < 6364.8
         zaverage_counter = zaverage_counter+1;
         zaverage_sum = zaverage_sum+z_filterdata(g);

         xaverage_counter = xaverage_counter+1;
         xaverage_sum = xaverage_sum+x_filterdata(g);

         saverage_counter = saverage_counter+1;
         saverage_sum = saverage_sum+s_filterdata(g);

         taverage_counter = taverage_counter+1;
         taverage_sum = taverage_sum+t_filterdata(g);
   elseif z_data(g) > 8276.1 && z_data(g) < 8613.9
```

```
            zaverage_counter = zaverage_counter+1;
            zaverage_sum = zaverage_sum+z_filterdata(g);

            xaverage_counter = xaverage_counter+1;
            xaverage_sum = xaverage_sum+x_filterdata(g);

            saverage_counter = saverage_counter+1;
            saverage_sum = saverage_sum+s_filterdata(g);

            taverage_counter = taverage_counter+1;
            taverage_sum = taverage_sum+t_filterdata(g);
        end
    end
    PRINT = 'ZZZZZZZZZZZZZZZZZZZZ THE END ZZZZZZZZZZZZZZZZZZZZ'
  %PRINT TO SCREEN (TO CHECK THAT THE CODE IS WORKING!)
  zaverage_counter
  zaverage_average(i) = zaverage_sum/zaverage_counter
  xaverage_counter
  xaverage_average(i) = xaverage_sum/xaverage_counter
  saverage_counter
  saverage_average(i) = saverage_sum/saverage_counter
  taverage_counter
  taverage_average(i) = taverage_sum/taverage_counter

  Z_transpose = zaverage_average'
  X_transpose = xaverage_average'
  S_transpose = saverage_average'
  T_transpose = taverage_average'
end
```

Appendix H: Resistive Force Data

The graphs below show the resistive force (coefficient of rolling friction versus the normal force) in Figure H-1 and Figure H-2. The resistive force for the bald tire was higher at a slip ratio of 10 and 20. While the resistive force for the tire with tread was higher at a slip ratio of 0.

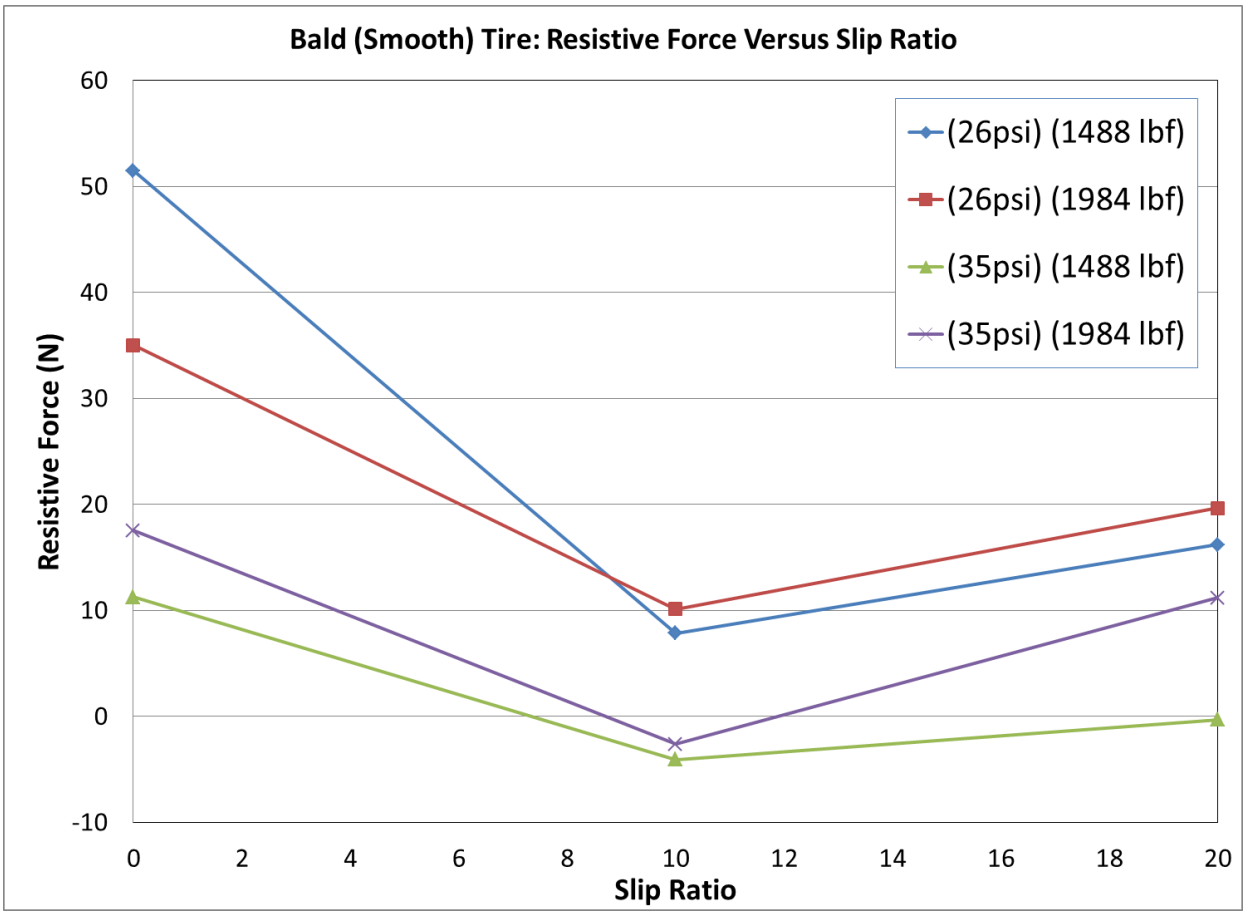

Figure H- 1. Resistive force data for the bald (smooth) tire.

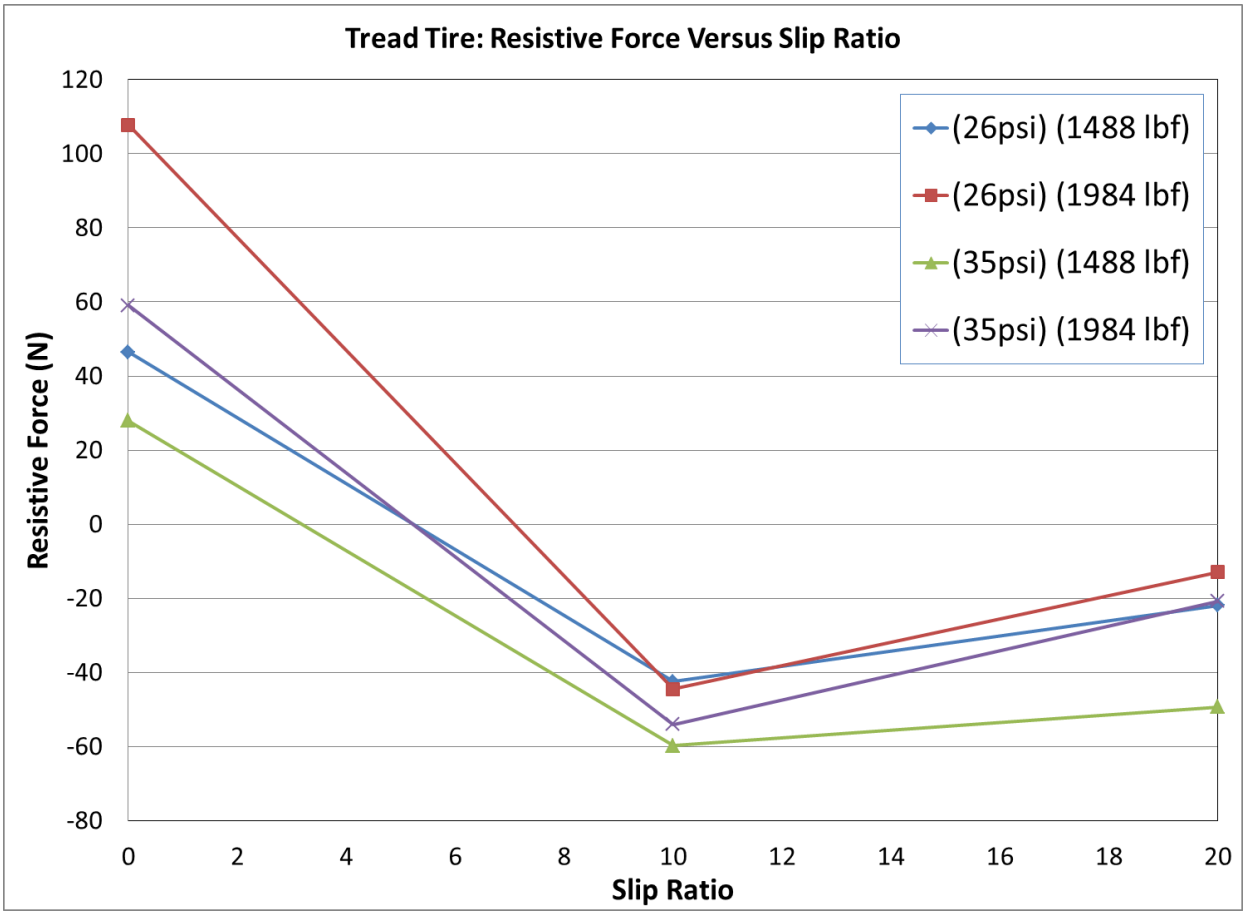

Figure H- 2. Resistive force data for the tire with the winter tread pattern.